Dissertation

submitted to the
Combined Faculties for the Natural Sciences and for Mathematics
of the Ruperto-Carola University of Heidelberg, Germany
for the degree of
Doctor of Natural Sciences

presented by

Xuepeng Chen
born in Guangde, China

Oral examination: February 07$^{\text{th}}$, 2008

High angular resolution observations of binary protostars

Referees: Prof. Dr. Thomas Henning
Prof. Dr. Ralf Klessen

Abstract: In this thesis I present a systematic effort to reveal the physical processes that lead to the formation of binary stars. We have observed, at high angular resolution, thirteen isolated low-mass protostellar cores, using the Owens Valley Radio Observatory millimeter array, the Australia Telescope Compact Array, and the IRAM Plateau de Bure Interferometer array. The observations were mainly carried out in the N_2H^+ (1–0) line and at 3 mm dust continuum. The results were complemented by infrared data from the *Spitzer Space Telescope* and the ESO *Very Large Telescope*. We find that binarity/multiplicity is frequent in the protostellar phase, though it is too early to derive a separation distribution. The circumstellar mass ratio distribution of binary protostars appears to be flat like that of more evolved long-period main-sequence binary stars, and more than 75% of protobinary systems have circumstellar mass ratios below 0.5. The specific angular momenta of protostellar cores are intermediate between those of prestellar cores and the orbital angular momenta of wide pre-main sequence binary systems. There appears to be no significant decrease of angular momentum between the onset of the protostellar collapse and the emergence of a binary star, which suggests that most of the angular momentum contained in the collapse region is transformed into orbital angular momentum of the resulting stellar binary system. We find that during core fragmentation the angular momentum is not evenly, in value and direction, divided between sub-cores. Furthermore, most cores with binary protostars have ratios of rotational to potential gravitational energy of $\beta_{\rm rot} > 1\%$. This is consistent with theoretical simulations and suggests that the initial amount of rotational energy in a molecular cloud core is playing an important role in the protostellar fragmentation process.

Zusammenfassung: In dieser Arbeit präsentiere ich eine systematische Untersuchung der physikalischen Prozesse die zur Bildung von Doppelsternsystemen führen. Wir haben insgesamt dreizehn massearme isolierte protostellare Kerne bei hoher Winkelauflösung mit dem Owens Valley Radio Observatory Millimeter-Interferometer, dem Australia Telescope Compact Array und dem IRAM Plateau de Bure Interferometer beobachtet. Die Beobachtungen wurden hauptsächlich bei der Wellenlänge der N_2H^+ (1–0) Linie und im 3 mm Kontinuum durchgeführt. Die Ergebnisse werden ergänzt durch Infrarotdaten vom *Spitzer Space Telescope* und vom ESO *Very Large Telescope*. Wir finden dass Duplizität und Multiplizität in der protostellaren Phase häufig vorkommt. Allerdings ist es noch zu früh, eine Abstandsverteilung abzuleiten. Die Verteilung der zirkumstellaren Massenverhältnisse in Doppel-Protosternen scheint flach zu sein, wie die Massenverhältnisverteilung von weiterentwickelten Hauptreihendoppelsternen. Mehr als 75% der Doppel-Protosternsysteme haben Massenverhältnisse unter 0.5. Die Werte des spezifischen Drehimpulses von protostellaren Kernen liegen zwischen denen von prästellaren Kernen und den Bahndrehimpulsen von Vorhauptreihendoppelsternen. Zwischen dem Beginn des protostellaren Kollaps' und der Bildung eines Doppelsternsystems scheint es keine signifikante Verringerung des Gesamtdrehimpulses zu geben. Daraus kannn man schliessen dass der groesste Teil des in der Kollapsregion enthaltenen Drehimpulses in Bahndrehimpuls des entstehenden Doppelsternsystems umgewandelt wird. Wir finden auch dass beim Fragmentationsprozess der Gesamtdrehimpuls oft nicht gleichmässig zwischen den Fragmenten aufgeteilt wird, sowohl bezüglich Wert als auch Richtung. Weiterhin finden wir dass das Verhältniss zwischen Rotationsenergie und potentieller Gravitationsenergie ($\beta_{\rm rot}$) in den meisten Kernen mit Doppel-Protosternen grösser als 1% ist. Dieses Ergebnis ist konsistent mit theoretischen Simulationen und deutet darauf hin, dass der ursprüngliche Anteil der Rotationsenergie am Gesamtenergiegehalt eines Molekülwolkenkerns eine wichtige Rolle im protostellaren Fragmentationsprozess spielt.

Contents

Chapter 1

Introduction

Over the past two decades, the formation of low-mass ($M \leq 2\,M_{\odot}$) stars has been well understood (see e.g., Reipurth et al. 2007 for recent reviews). It is widely accepted that low-mass stars form by gravitational contraction in molecular cloud cores. Initially, these molecular cloud cores are supported against gravity by thermal, magnetic, and turbulent pressures. At a certain point, the condensations inside these cores become gravitationally unstable and quickly collapse to form a protostar which is surrounded by an envelope and a disk. From the infalling envelope, matter is continuously accreted onto the disk and then the protostar, which results in an increasing mass of the star-disk system (see Shu et al. 1987). However, in detail, several important aspects in this picture still remain poorly known, such as the initial conditions of the collapse process, the formation of binary and higher-order multiple systems, and the evolution of angular momentum. In this chapter, I briefly describe these aspects, as well as the goals of this thesis motivated by these problems.

1.1 The initial conditions of star formation

The outcome of the collapse of a molecular cloud core depends on the initial conditions and how the collapse is initiated. On the theoretical side, two different scenarios have been widely studied to illustrate two limiting possibilities for initiating collapse. One scenario is the well-known inside-out collapse model of Shu (1977), which is based on the assumption that molecular cloud cores are initially magnetically supported and condense gradually by ambipolar diffusion. This quasi-static contraction process causes the core to become increasingly centrally condensed and increasingly supported by thermal pressure, eventually becoming a singular isothermal sphere (SIS) with no magnetic support and with a density distribution of $\rho(r) \propto r^{-2}$ (Shu et al. 1987). However, this long called 'standard model' has been challenged by more and more observations (see e.g., André et al. 2002) and theoretical calculations (see e.g., Whitworth et al. 1996), and gradually replaced by a new scenario, in which large-scale, supersonic turbulence controls the collapse and hence star formation (see e.g., Klessen et al. 2000). In this modified scenario, cores form as turbulence-generated density fluctuations and are dynamical, not quasi-static, objects with lifetimes not exceeding a few Myr (see a review by Ballesteros-Paredes et al. 2007). Simulations of such turbulent cores have produced

many of the observed properties of cores (e.g., Jappsen & Klessen 2004) and a mass spectrum similar to the observed core mass spectrum (e.g., Klessen et al. 2005). More details of theories and physics of the protostellar collapse can be found in the recent reviews by Larson (2003), Mac Low & Klessen (2004), and McKee & Ostriker (2007).

On the observational side, there are two complementary approaches to understand the initial conditions of the protostellar collapse: (1) studying the structure and kinematics of prestellar cores observed prior to protostar formation, and (2) studying the structure of the youngest protostars observed soon after point mass formation. The most recent observational results concerning the initial conditions of protostellar collapse can be found in the reviews by André et al. (2002), Di Francesco et al. (2007), and Ward-Thompson et al. (2007).

1.1.1 Prestellar cores

The prestellar stage of star formation may be defined as the phase in which a gravitationally bound core has formed in a molecular cloud, and evolves toward higher degrees of central condensation, but no central hydrostatic protostellar object exists yet within the core (André et al. 2000). Figure 1.1a shows a dust continuum map of one such core. As this map shows and as already mentioned by Ward-Thompson et al. (1999), most prestellar cores are far from being spherically symmetric and instead have rather filamentary structure.

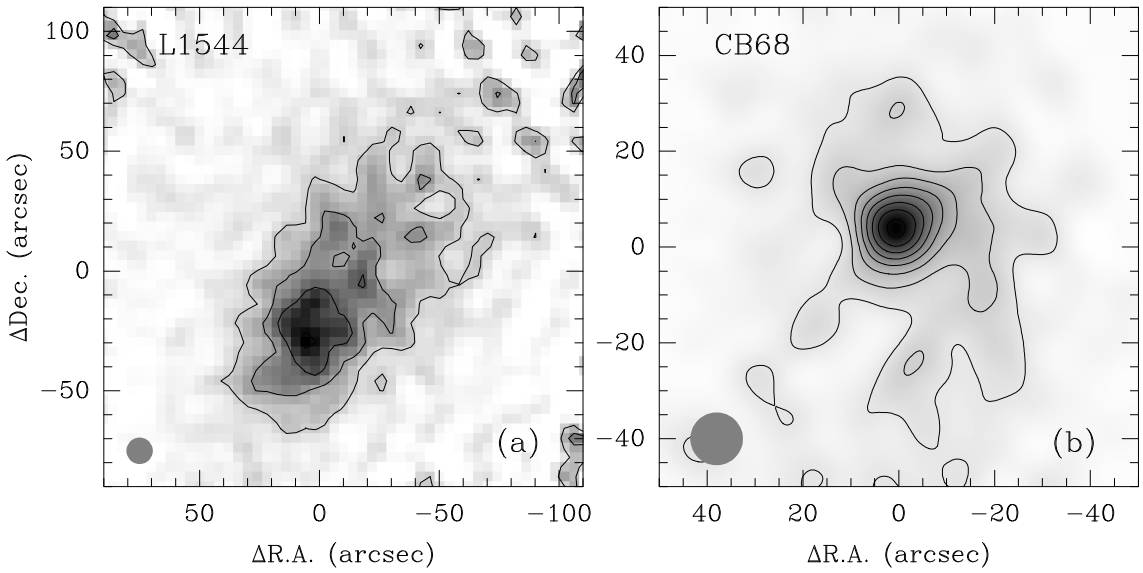

Figure 1.1: IRAM-30 m 1.3 mm dust continuum images of **a)** a prestellar core (L 1544; from Tafalla et al. 1998) and **b)** a Class 0 protostellar core (CB 68; from Launhardt et al. 2008, in prep.).

Based on (sub-) millimeter dust continuum emission observations and mapping the same cold core dust in absorption against the background infrared emission, models of isolated prestellar cores have been derived by several research groups (see the review

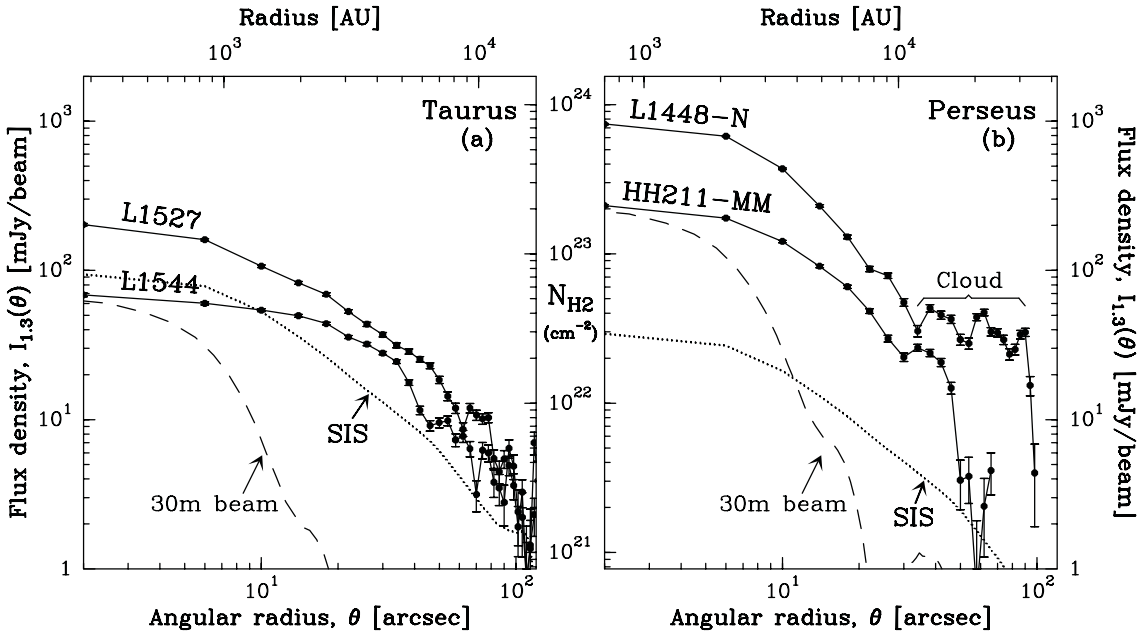

Figure 1.2: Radial density profiles of (a) L1544 (prestellar) and L1527 (Class 0) in Taurus (isolated star-forming cloud) and (b) HH211-MM and L1448-N (Class 0) in Perseus (clustered star-forming cloud). The dotted lines marked SIS (Singular Isothermal Sphere) show the initial conditions for spontaneous collapse (see Shu et al. 1987) convolved with the beam (dashed line). Note that prestellar core has a flatter profile than the protostellar cores and that the column densities in Perseus are an order of magnitude higher than both the model and the Taurus cores (adopted from Ward-Thompson et al. 2007).

by André et al. 2002). Despite different observing and modeling approaches, all groups draw some common conclusions: isolated prestellar cores appear to have an inner flat-density [$\rho(r) \propto r^{-1}$] profile of radius few hundred to few thousand AU (see Fig. 1.2a) and central densities of one to a few $10^6\,\mathrm{cm}^{-3}$, an outer radial density profile that approaches $\rho(r) \propto r^{-2}$, a well-defined outer cut-off radius at $\sim 10^4$ AU, and total mass between 2 and $5\,M_\odot$. Typical masses inside 5000 AU are of order $0.5 - 1.0\,M_\odot$, i.e., $\sim 20\%$ of the total core mass. Typical dust temperatures are $6 - 10$ K in the inner core while $10 - 15$ K towards the outer edge, which is due to external heating by the interstellar radiation field (e.g., Evans et al. 2001). Evans et al. (2001) also find that the large-scale morphology of many prestellar cores can be well-modeled by the so-called Bonner-Ebert spheres with different degrees of central concentration (see the review by Di Francesco et al. 2007). However, it should be noted that the filamentary structure, as well as the turbulent nature of the outer envelope (see Park et al. 2004), make the assumption of an ideal Bonner-Ebert gas sphere somewhat doubtful.

Turning to kinematics, the prestellar cores are characterized by narrow line widths of order 0.2 to $0.5\,\mathrm{km\,s}^{-1}$ in which the thermal contribution dominates, despite these cores are in cluster-forming region, like Ophiuchus (e.g., Belloche et al. 2001) or isolated star-forming region, like Taurus (e.g., Benson & Myers 1989). This means that the inner parts of the gravitationally bound cores are "velocity coherent" (Goodman et al.

1998) and essentially free of turbulence. Apart from low levels of turbulence, prestellar cores are characterized by slow rotation, with velocity gradients ranging from 0.3 to 5 $\mathrm{km\,s^{-1}\,pc^{-1}}$ (see Di Francesco et al. 2007). The dependence of velocity gradient on the radius of a core is $v \sim R^{-0.4}$, with a large scatter (Goodman et al. 1993). Furthermore, subsonic and extended infall motions ($0.05-0.09\ \mathrm{km\,s^{-1}}$) are also common in prestellar cores (e.g., Lee et al. 2001).

1.1.2 Class 0 protostars

Specifically, Class 0 protostars (or protostellar cores) can be defined by the following observational properties: (1) indirect evidence for a central young stellar object, as indicated by, e.g., the detection of a compact centimeter radio continuum source, a collimated outflow, or an internal heating source; (2) centrally peaked but extended sub-millimeter continuum emission tracing the presence of circumstellar dusty envelope (not just a disk); (3) high ratio of sub-millimeter to bolometric luminosity suggesting the envelope mass exceeds the central stellar mass: $L_{\mathrm{submm}}/L_{\mathrm{bol}} > 0.5\%$, where L_{submm} is measured longward of $350\,\mu$m (André et al. 2000).

Isolated Class 0 protostellar cores have been observed in the (sub-) millimeter dust continuum emission and modeled by a lot of groups, e.g., Motte & André (2001) and Shirley et al. (2002). Compared with prestellar cores, Class 0 protostellar cores have a higher central mass concentration ($M_{5000\mathrm{AU}}/M_{\mathrm{tot}} \approx 0.4$) and appear to be more spherical symmetric (see an example in Fig. 1.1b). Their envelopes have a power-law radial density gradient of $\rho(\mathrm{r}) \propto r^{-2}$ and a well-defined outer radius at $\sim 1-2 \times 10^4\,\mathrm{AU}$ (see Fig. 1.2). Densities inside $R < 3000-4000\,\mathrm{AU}$ are about two orders of magnitude higher than in prestellar cores. Total masses are comparable to those of prestellar cores, i.e., $2-5\,M_{\odot}$. At the center, higher dust temperature ($\sim 15-20\,\mathrm{K}$) and embedded accretion disks add additional dust emission, leading to strongly centrally peaked sub-millimeter and millimeter continuum images. Envelope dust temperatures are comparable to those in prestellar cores, which means that the embedded protostars do not yet considerably contribute much heating to the envelope. It should be noted that protostellar cores in dense and clustered star-forming regions have different structures than isolated cores due to different environments like e.g., better shielding from the external radiation field, differences in external pressure and turbulent environment, and effects of competitive accretion. Indeed, Johnstone et al. (2000) and Motte & André (2001) find smaller outer cutoff radii ($R_{\mathrm{out}} \leq 5000\,\mathrm{AU}$), smaller degrees of central condensation, and higher column densities for cores in the ρ Ophiuchus main cloud and Perseus (see Fig. 1.2b).

So far there are very few detailed studies of velocity structures towards protostellar cores (see the review by Ward-Thompson et al. 2007). Typical examples are isolated Class 0 object IRAM 04191 in Taurus (Belloche et al. 2002), and IRAS 4 in the NGC 1333 protocluster (Di Francesco et al. 2001). IRAM 04191 is associated with a flattened circumstellar envelope, seen in the dust continuum and in dense gas tracers (Belloche et al. 2002). The velocity field of IRAM 04191 shows a clear gradient across this envelope of $\sim 7\,\mathrm{km\,s^{-1}\,pc^{-1}}$ increasing from west to east along the long axis, roughly perpendicular to the outflow axis, strongly suggesting rotation. Furthermore,

this rotation does not occur in a solid-body, but differential: the inner ~ 3500 AU region seems to be rotating much faster than the outer parts of the core. Direct evidence for infall motions is also observed for IRAM 04191 in optically thick lines, indicative of a relatively flat infall velocity profile ($v_{\rm inf} \sim 0.1\,{\rm km\,s^{-1}}$) for 3000−11000 AU and larger infall velocities scaling as $v_{\rm inf} \propto r^{-0.5}$ for r $\leq$ 3000 AU (Belloche et al. 2002). For NGC 1333 IRAS4, the example in the cluster-forming region, evidence of fast rotation (velocity gradient as high as $\sim 40\ {\rm km\,s^{-1}\,pc^{-1}}$) and of large infall velocities ($0.5 - 0.7$ ${\rm km\,s^{-1}}$), was found by Di Francesco et al. (2001).

1.2 Theories and models of binary star formation

After the initial stages of collapse process, another major gap in our understanding of star formation concerns the origin of binary stars. Detailed studies in recent years have shown that binary and higher-order multiple systems represent the preferred outcome of the star formation process, but at present we do not know how this occurs.

Different formation scenarios for binary stars have been proposed, of which the classical ideas of capture and fission are no longer considered major processes (see review by Tohline 2002). Numerous theoretical simulations support the hypothesis that the fragmentation of molecular cloud cores is the main mechanism for the formation of binary/multiple stellar systems (see reviews by Bodenheimer et al. 2000, Tohline 2002, and Goodwin et al. 2007).

Regarding to the collapse phase and scale, fragmentation models could be divided into initial cloud fragmentation (prior to protostellar collapse) and protostellar fragmentation (during or after protostellar collapse). For the single collapsing protostellar core, rotational fragmentation and turbulent fragmentation were two main mechanisms suggested in terms of the source of angular momentum. In the dense cluster-forming environment, disk fragmentation was proposed as a mechanism for low-mass companions. Furthermore, 'secondary' or 'delayed' fragmentation was proposed for very close (separation ≤ 10 AU) binary systems.

1.2.1 Initial fragmentation

In a study of the separation distribution of optical binaries, Larson (1995) found a clear break in the distribution at 0.04 pc (~ 8000 AU), which was considered to correlate with the Jeans size. Larson suggested that systems on this and larger scales formed by fragmentation of prestellar cores and separate collapse.

The basic idea of this initial fragmentation is that the collapse is initiated in a large-scale molecular cloud core which contains multiple Jeans masses in a weakly condensed configuration, e.g., a prolate or filamentary gaussian distribution with several Jeans masses along the long axis and one Jeans mass across the short axis; with some initial perturbations, provided by either slow rotation (Bonnell et al. 1991) or turbulence (Bonnell et al. 2007), the large cloud core fragments at Jeans scale into several dense cores, in which the separate protostellar collapse then starts and proceeds more quickly than across the whole structure.

1.2.2 Rotational fragmentation

It has been recognized for a long time that fragmentation may occur in a spherical cloud with solid-body rotation and an isothermal equation of state. A number of simulations have shown that rotation cloud cores do fragment if $\beta_{\rm therm}\beta_{\rm rot} \leq 0.12 - 0.15$, where $\beta_{\rm therm} = E_{\rm therm}/E_{\rm grav}$ is the initial thermal virial ratio ($E_{\rm therm}$ is the thermal kinetic and $E_{\rm grav}$ is the gravitational potential energy) and $\beta_{\rm rot} = E_{\rm rot}/E_{\rm grav}$ is the initial rotational virial ratio ($E_{\rm rot}$ is the rotational kinetic energy) (Tohline 2002).

Boss & Bodenheimer (1979) and Burkert & Bodenheimer (1993) added density perturbation into a standard rotating cloud and found that with a perturbation the cloud fragments into a binary system. This simulation can be made more physical by including an adiabatic or barotropic equation of state (see the review by Goodwin et al. 2007). Bate & Burkert (1997) showed that the Boss & Bodenheimer model produces a line of fragments with a barotropic state, but not if it remains isothermal. In addition, Boss et al. (2000) simulated a cloud with a certain perturbation using a barotropic state and also with radiation transport. They found that the second case produces a binary while the first does not, despite the similarity of the pressure-temperature relations. These simulations suggest that rotational fragmentation is highly sensitive to thermal inertia and radiation transport effects.

On the other hand, a series of simulations have shown that the level of rotation energy (i.e., $\beta_{\rm rot}$) plays an important role in the fragmentation process (see reviews by Bodenheimer et al. 2000 and Tholine 2002). Boss (1999) has shown that rotating cloud cores fragment when $\beta_{\rm rot} > 0.01$ initially (considering magnetic fields support fragmentation), while Machida et al. (2005) suggest that the rotational fragmentation occurs only when $\beta_{\rm rot} \geq 0.04$ (considering magnetic fields suppress fragmentation).

1.2.3 Turbulent fragmentation

Recent theoretical simulations have shown that turbulence in the cores is also important for fragmentation because it may provide the angular momentum required for the formation of binary and multiple systems. The level of turbulence is usually quantified as a turbulent virial ratio $\beta_{\rm turb} = E_{\rm turb}/E_{\rm grav}$ ($E_{\rm turb}$ is the kinetic energy in turbulent motion). Simulations of the effects of turbulence in cores could be divided into two different regimes: high-velocity and low-velocity (see the review by Goodwin et al. 2007). Highly turbulent simulations focus on $\beta_{\rm turb} = 1$ in $50\,M_\odot$ and $5\,M_\odot$ cores, while lowly turbulent simulations range between $\beta_{\rm turb} = 0 - 0.25$ in $5.4\,M_\odot$ cores.

Even very low levels of turbulence ($\beta_{\rm turb} \sim 0.025$) are enough to allow cores to fragment (Goodwin et al. 2004). As the level of turbulence is increased, the average number of stars that form in a core increases (Goodwin et al. 2004). In highly-turbulent cores, the supersonic turbulent velocity field creates a number of condensations in shocked, converging regions which become Jeans unstable and collapse (see e.g., Bate et al., 2003). However, it is unclear if this mode of fragmentation is realistic in low-mass cores as the observed levels of non-thermal motions rule out significant highly supersonic turbulence in these cores.

1.2.4 Disk fragmentation

Disk fragmentation is a mechanism by which low-mass companions and brown dwarfs may be formed. The basic idea is that, in the dense environments, e.g., star-forming clusters, close encounters between stars can disturb the circumstellar disks, leading to the fragmentation of stable disks.

A series of simulations suggest that most star-disk interactions will lead to gravitational instabilities, which form new low-mass companions (Boffin et al. 1998; Watkins 1998). Bate et al. (2003) also find that star-disk encounters play an important role in forming binaries and truncating disks. Furthermore, star-disk encounters are thought to play an important role in redistributing angular momentum in protoplanetary disks even if they do not trigger further fragmentation (see Larson 2002).

Thies et al. (2005) suggest that star-disk encounters may lead to the formation of brown dwarfs (or even planetary) mass companions. However, they are probably not a significant contributor to the primordial stellar binary population. This is due to the requirement that the encounters occur early in the star formation process – during the Class 0 phase when the disk mass is still very large compared to the stellar mass – a phase which lasts for only 10^5 yr, leaving only a small time for encounters to occur.

1.2.5 Secondary fragmentation

As suggested by Tohline (2002), there is a second isothermal phase in the evolution of gas towards stellar densities. This occurs at a temperature of 2000 K and a density of 10^{-3} g cm^{-3} when molecular hydrogen dissociates into atomic hydrogen. This phase occurs in the hydrostatic protostar when its radius is about 1 AU. If fragmentation can occur at this stage, it may explain very close binary systems.

Both Boss (1989) and Bonnell & Bate (1994) simulated the collapse of a rotating hydrostatic first object to high densities and found that fragmentation can occur in antisymmetric instabilities or a ring formed by a centrifugal bounce. Nevertheless, Bate (1998) found that spiral instabilities remove angular momentum and suppress further fragmentation. Recent simulations by Saigo & Tomisaka (2006) suggest that the angular momentum of the first core is a crucial factor in determining if fragmentation will occur during the second collapse. Therefore, it is unclear yet if a secondary fragmentation phase occurs.

1.3 Observations of binary systems

1.3.1 Main sequence binary systems

Main sequence (MS) binary/multiple systems in the field are so far the best-studied due to the availability of local samples whose completeness is easier to estimate. The *fraction* of MS stars in binary/multiple systems is found to be high and increasing with primary mass. A series of surveys found that $\sim 60\%$ of G-stars (Duquennoy & Mayor 1991; hereafter DM91), $\sim 45\%$ of K-stars (Mayor et al. 1992), and $\sim 42\%$ of M-dwarfs are in binary systems (Fisher & Marcy 1992). DM91 found that binary stars

have *separations* from a few $R_\odot$ to 104 AU. The distribution of separations appears to be wide and flat, with a broad peak at about 30 AU (see Fig. 1.3a). A similar distribution is found for M-dwarfs by Fischer & Marcy (1992) and generally seems to hold for all stars. Considering the distribution of *mass ratios*, DM91 found that most binaries do not have equal masses, but that the distribution is slowly increasing for smaller mass ratios. In contrast, with the overall mass ratio distribution, the closest systems appear to have a nearly flat distribution with a possible rise towards equal mass systems (Mazeh et al. 1992; see Fig. 1.3b). In terms of the *eccentricity*, only the closest of binary stars have circular orbits due to tidal circularization. Longer period binaries all have non-zero eccentricities, while the maximum eccentricity at a given period increases with the period.

1.3.2 Pre-main sequence binary systems

The properties of pre-main sequence (PMS) multiple systems are much harder to determine than those in the field. The most important difference between the PMS and MS binaries is that young PMS stars have a significantly higher multiplicity fraction than the MS stars (Mathieu 1994). The overall fraction of binary stars among the PMS population is at least as large as has been documented for MS stars, i.e., certainly greater than 50%. More specifically, the binary frequency in the separation range from 100 to 1000 AU is a factor of ~ 2 higher than in the field (see Goodwin et al. 2007). Extrapolating this increase across the whole separation range implies that

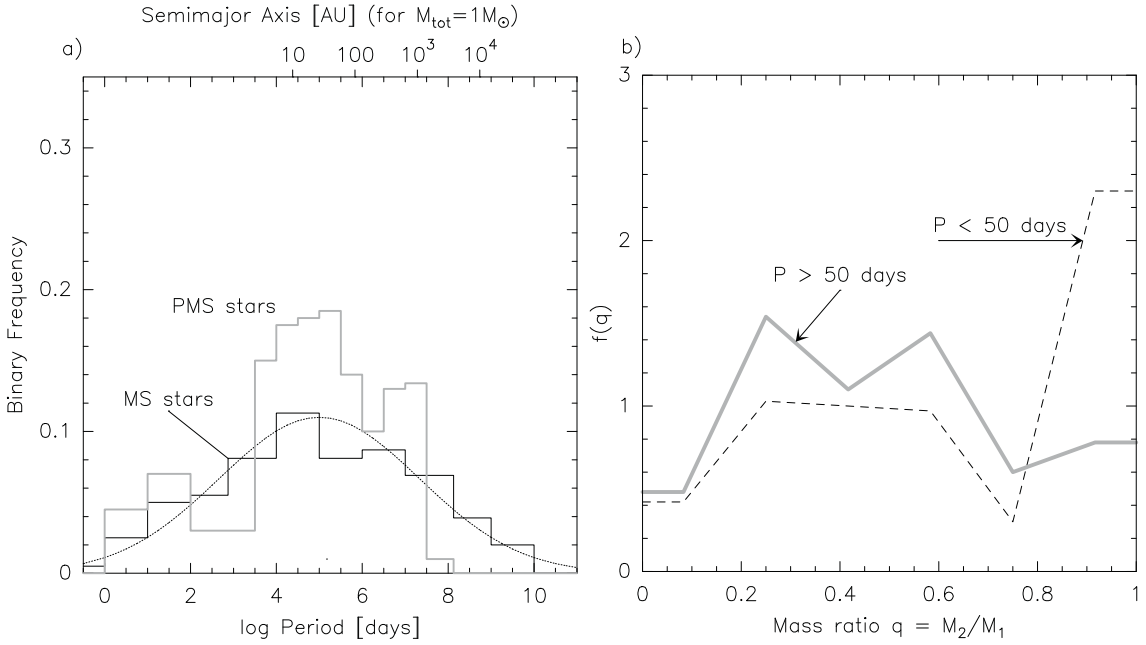

Figure 1.3: (a) Period/separation distribution of MS and PMS binary systems (Duquennoy & Mayor 1991; Mathieu 1994; Simon et al. 1995). (b) Distribution of mass ratios in MS binary systems (Halbwachs et al. 2003). The image is adopted from Launhardt (2004).

fraction for PMS stars could be as high as 100%. Indeed, it appears that in Taurus the binary frequency is $\sim 100\%$ for stars of $> 0.3\,M_{\odot}$ (Leinert et al. 1993; Köhler & Leinert 1998). The separation distribution of PMS stars also appears different to that in the field with an over-abundance of binaries with separations of a few hundred AU (Mathieu 1994; Patience et al. 2002; see Fig. 1.3a). The mass-ratio distribution of PMS stars is similar to field population. However, a detailed comparison is not yet possible because low-mass companions to PMS primaries are very difficult to observe because the available results depend mostly on direct imaging or speckle interferometry, while for MS systems radial-velocity surveys have been done over decades. The eccentricity distribution of PMS stars is also similar to the field, with a thermalized distribution except at low separation where tidal circularization has occurred rapidly (e.g., White & Ghez 2001).

1.3.3 Protostellar binary systems

Compared with MS and PMS stars, protostars are deeply embedded in molecular cloud cores and surrounded by opaque, infalling envelopes and accretion disks. All radiation emanating from the protostar is re-processed by the surrounding dust. Therefore, only emission from circumstellar material can usually be directly observed. The range of dust temperatures and gas densities involved in low-mass protostellar cores make observations of thermal dust continuum emission from far-infrared to millimeter wavelengthes as well as millimeter molecular line transitions most favorable.

The largest current-day single-dish millimeter telescopes (e.g., IRAM-30 m) provide angular resolution of $\sim 10''$ at 1 mm wavelength, corresponding to 2000 AU at a distance of 200 pc. This is far beyond the the peak of binary separation distribution (see Fig. 1.3). Due to long limitation by the low resolution of (sub-) millimeter telescopes, the observational information of protobinary systems is extremely missing. Only recently some progress was made in this field thanks to the advance of current large millimeter interferometric array (e.g., Looney et al. 2000 and Launhardt 2004), but the number observed is still small (because hard to get observing time) and no statistical conclusions can be drawn yet.

1.4 The angular momentum problem

An important open question in the theory of star formation is the evolution of the angular momentum of the stars. It has been realized for many decades that the amount of specific angular momentum in a typical star-forming cloud core is several orders of magnitude too large to be contained in a single star (even when this star is rotating at breakup speed). This is the classical 'angular momentum problem' which was first well expressed by Spitzer (1978). Table 1.1 lists the typical values of specific angular momentum. It is obvious that the amounts of angular momentum have to be reduced at least by a factor of $10^4 - 10^5$ from the core to the star formed therein.

It is believed that during the different stellar evolutionary phases, several different mechanisms could remove angular momentum from the molecular cloud, the protostellar core, the circumstellar disk, and later even from the visible T Tauri stars (see

Table 1.1: Typical values of specific angular momentum taken from Bodenheimer (1995) and Lamm (2003).

Object	J/M [$\mathrm{m^2\ s^{-1}}$]
Molecular cloud ($\sim 1\,\mathrm{pc}$)	10^{19}
Molecular cloud core ($\sim 0.1\,\mathrm{pc}$)	10^{17}–10^{18}
Binary system (period $10^4\,\mathrm{yr}$)	4×10^{16}–10^{17}
Binary system (period $10\,\mathrm{yr}$)	4×10^{15}–10^{16}
Binary system (period $3\,\mathrm{day}$)	4×10^{14}–10^{15}
$100\,\mathrm{AU}$ disk ($1\,M_\odot$ central star)	5×10^{16}
Planet (Jupiter orbit)	10^{16}
PMS star (T Tauri star)	5×10^{13}
ZAMS (median young clusters)	3×10^{12}
Present sun	10^{11}

Bodenheimer 1995 and Lamm 2003). During the early low-density phase of cloud evolution, magnetic fields are still strongly coupled to the gas (Mouschovias 1991); at this phase, magnetic braking is proposed as a mechanism for the angular momentum removal (Basu & Mouschovias 1994). However, magnetic fields are predicted to decouple from the gas by ambipolar diffusion long before stellar densities are reached, and angular momentum is then expected to be approximately conserved during the later stages of collapse (Mouschovias & Ciolek 1999). Since the typical observed angular momentum of prestellar cores is still three orders of magnitude larger than the maximum amount that can be contained in a single star (see Table 1.1), an important part of the angular momentum problem remains unsolved.

In principle, there are at least three ways to dispose of this excess angular momentum. (1) It could be transported to outlying diffuse material by viscous transport processes in a protostellar accretion disk, thus allowing most of the mass to be accreted by a central star (see a review by Balbus 2003). However, as discussed by Larson (2002), transport processes in disks do not clearly offer a solution to the angular momentum problem because no adequate transport mechanism has yet been identified, and because even if such a mechanism could be identified, a residual disk would have to expand to a very large radius to absorb all of the angular momentum, and this would make the accretion time longer than the inferred ages of young stars. (2) Much of the initial angular momentum could go into the orbital motions of the stars in a binary or multiple system (Bodenheimer 1995). Since the angular momentum of a typical prestellar core is comparable to that of a wide binary (see Table 1.1), it is likely that at least the wide binaries can be formed directly by the fragmentation of rotating cloud cores. And (3) the angular momentum contained in the star-disk system could be carried out by bipolar outflows/jets, although the actual launch mechanisms remain controversial (Shang et al. 2007; Ray et al. 2007). Unfortunately, so far there is not much observational evidence of outflow rotation. Only recently Bacciotti et al. (2003) and Coffey et al. (2004) have detected possible rotation signature in a few optical jets from T Tauri stars.

1.5 About this thesis

Based on numerous observations and theoretical simulations, the statistical properties of binary stars have been gradually comprehended over the past two decades (see above). Both the observations and simulations support that the fragmentation of protostellar cores is the main mechanism for the formation of binary systems, leading to systems with a wide variety of properties. These properties are largely determined by the accretion process which, in turn, strongly depends on the initial conditions of the cloud cores, e.g., the initial distributions of mass and angular momentum (see Bate & Bonnell 1997). Some of the theoretical predictions, e.g., that close binary systems are likely to have mass ratios near unity (see Bate 2000), are already indirectly supported by statistical studies of evolved binary systems (see Halbwachs et al. 2003).

However, *our current knowledge of the formation of binary stars mostly relies on observations of MS and PMS stars and the constrains they put on the models.* The observational link between initial conditions in a molecular cloud core and the final star systems formed therein is still missing. Furthermore, as multiple systems certainly undergo dynamical evolution, important information about the formation phase is lost in the final systems. Direct observations of (pre-) protostellar cores are needed therefore to answer a number of questions, e.g., **how common is binarity/multiplicity in the protostellar phase? What makes a prestellar core fragment in the collapse phase? How is mass distributed in the process of fragmentation? How is angular momentum distributed? Are there differences between cores forming binaries and those forming single stars?** Unfortunately, direct observations of protostellar stages, when the main collapse has started but no optical or infrared emission emerges from the protostar through the opaque infalling envelope, were long hampered by the low angular resolution of millimeter telescopes and the results were mostly interpreted in terms of single star formation. Only the recent advance of large millimeter interferometers has enabled us to directly observe the formation phase of binary stars, but the number of known systems is still very small and no systematic observational studies of the initial fragmentation process do exist yet.

To search for binary protostars and to derive their kinematic properties, we have started a systematic programm to observe, at high angular resolution, a number of isolated low-mass (pre-) protostellar cloud cores. The initial survey was conducted at the Owens Valley Radio Observatory (OVRO) millimeter array, and then continued with the Australia Telescope Compact Array (ATCA) and the IRAM Plateau de Bure Interferometer (PdBI) array. Complementary infrared data from the *Spitzer Space Telescope* (*Spitzer*) and the ESO *Very Large Telescope* (VLT) are also used. In this thesis I present the main results of this programm. The outline of the thesis is as follows:

• In Chapter 2 I introduce our N_2H^+ (1–0) line observations conducted at OVRO for nine protostars, of which three were identified as binary protostars.

• In Chapter 3 I present ATCA and *Spitzer* observations towards the two southern binary protostars CG 30 and BHR 71.

• The first results from the IRAM-PdBI towards binary protostars L1448 IRS3 and SVS 13 are presented in Chapter 4.

• For comparison with the millimeter results, I present VLT/NACO near-infrared observations of young stellar objects in Chapter 5.

• Taking all results together, I discuss new observational constraints from this thesis work to the binary star formation models in Chapter 6.

• I summarize the main results of this thesis in Chapter 7 and outline future plans in the framework of this study.

Chapter 2

OVRO N_2H^+ observations of Class 0 protostars

This chapter is based on one paper published by Astrophysics Journal by Chen, Launhardt, & Henning (2007) and two papers to be submitted to the Astrophysics Journal Letter by Launhardt, Chen & Sargent, et al. (2008).

Abstract

We present the results of an interferometric study of the N_2H^+ (1–0) emission from nine nearby, isolated, low-mass protostellar cores, using the OVRO millimeter array. The main goal of this study is the kinematic characterization of the cores in terms of rotation, turbulence, and fragmentation. Eight of the nine objects have compact N_2H^+ cores with FWHM radii of $1200 - 3500$ AU, spatially coinciding with the thermal dust continuum emission. The only more evolved (Class I) object in the sample (CB 188) shows only faint and extended N_2H^+ emission. The mean N_2H^+ line width was found to be $0.37\,\mathrm{km\ s^{-1}}$. Estimated virial masses range from 0.3 to $1.2\,M_\odot$. We find that thermal and turbulent energy support are about equally important in these cores, while rotational support is negligible. The measured velocity gradients across the cores range from 6 to $24\,\mathrm{km\,s^{-1}\,pc^{-1}}$. Assuming these gradients are produced by bulk rotation, we find that the specific angular momenta of the observed Class 0 protostellar cores are intermediate between those of dense (prestellar) molecular cloud cores and the orbital angular momenta of wide PMS binary systems. There appears to be no evolution (decrease) of angular momentum from the smallest prestellar cores via protostellar cores to wide PMS binary systems. In the context that most protostellar cores are assumed to fragment and form binary stars, this means that most of the angular momentum contained in the collapse region is transformed into orbital angular momentum of the resulting stellar binary systems.

2.1 Introduction

This chapter presents N_2H^+ (1–0) survey for nine protostellar cores observed by OVRO millimeter-wave array. For this survey we selected a number of well-isolated and nearby low-mass protostellar cores. Priority was given to sources which were already well-characterized either by our own previous observational data or in the literature. Most sources are Class 0 objects, which represent the youngest protostars at an age of a few $\times\ 10^4$ yr. These objects provide an opportunity to probe the earliest and most active stage of the star formation process, where most of the initial information is still preserved. The target list and basic properties of the sources are summarized in Table 2.1.

For studying the gas kinematics and derive rotation curves, we choose to observe the N_2H^+ (1–0) hyperfine structure line complex at 93.1378 GHz. N_2H^+ is known to be a selective tracer of cold, dense, and quiescent gas and is particularly suitable for studying the structure and kinematics of cold star-forming cores (Turner & Thaddeus 1977; Womack, Ziurys, & Wychoff 1992; Bachiller 1996; Caselli et al. 2002). It is the most reliable tracer of the gas kinematics in pre- and protostellar cores for three reasons: (1) compared to other molecules, it depletes much later and more slowly onto grains (Bergin & Langer 1997), (2) it is formed where CO is depleted and thus traces only the dense cores and not the wider envelope and is thus perfectly suited for interferometric observations, and (3) with its seven hyperfine components within 17 $\mathrm{km\,s^{-1}}$ (including optically thin and moderately optically thick components; Caselli et al. 1995) it provides much more precise and reliable kinematic information than a single line, even with a moderate signal-noise ratio.

2.2 Observations and data reduction

Observations were carried out by R. Launhardt with the OVRO array of six 10.4 m telescopes during 7 observing seasons between 1999 and 2002. Five different array configurations (C, L, E, H, and U) were used, with baselines ranging from 18 to 480 m. All antennas were equipped with cooled SIS receivers which provided average system temperatures of $\sim 300 - 400$ K at the observing frequency. A digital correlator was centered at 93.1378 GHz. Spectral resolution and bandwidth were $\sim$ 0.2 $\mathrm{km\,s^{-1}}$ and 25 $\mathrm{km\,s^{-1}}$, respectively. Amplitude and phase were calibrated through frequent observations of quasars nearby to each source, typically every 20 minutes, resulting in an absolute position uncertainty of $\leq 0\farcs2$. The flux density scale was calibrated by observing Neptune and Uranus. The estimated uncertainty is $< 20\%$. Observing parameters are summarized in Table 2.2. The thermal dust continuum emission was measured simultaneously with the N_2H^+ and other line observations using a separate continuum correlator.

The raw data were edited and calibrated using the MMA software package (Scoville et al. 1993), and synthesized images were produced using MIRIAD (Sault et al. 1995) and its CLEAN algorithm, with "robust" weighting of the visibilities (Briggs et al. 1999). The cleaned and restored maps have effective synthesized beam sizes of $4-8''$

Table 2.1: Basic properties of target sources

Source Name	Associated IRAS source[a]	D [pc]	$L_{\rm bol}$ [$L_\odot$]	$T_{\rm bol}$ [K]	$M_{\rm env}$ [$M_\odot$]	Outflow	Infall	Class	Refs
IRAS 03282	03282+3035	300	1.2	23	2.9	y, bipol, coll.	y	0	1,2,3
IRAS 04166	04166+2706	140	0.4	91	1.0	y, bipol, coll.	y	0	1,3,4
RNO 43 MM	05295+1247	400	6.0		0.4	y, bipol, coll.		0	5,6
CB 68	16544−1604	160	1.6	74	3.5	y, bipol, coll.		0	7,8
L723 VLA2	19156+1906	300	3.3	47	7.3	y, quadrupol.		0	3,9
CB 188	19179+1129	300	2.6		0.7	y, bipol		I	8,10
CB 224	20355+6343	400	16		6.6	y, bipol	y	0/I	11,12,13
CB 230	21169+6804	400	8.2		5.1	y, bipol, coll.	y	0/I	10,11,12
CB 244	23238+7401	180	1.1	56	3.3	y, bipol	y	0	8,10,14

[a]The IRAS source is not always associated with the mm source.

References. — (1) Mardones et al. 1997; (2) Bachiller et al. 1994; (3) Shirley et al. 2000; (4) Tafalla et al. 2004; (5) Zinnecker et al. 1992; (6) Arce & Sargent 2004; (7) Vallée et al. 2000; (8) Launhardt & Henning 1997; (9) Lee et al. 2002; (10) Yun & Clemens 1994; (11) Wolf et al. 2003; (12) Launhardt et al. 1998; (13) Chen et al. in prep.; (14) Wang et al. 1995

Table 2.2: Target list and summary of observations

Source Name	Other Name	R.A. & Dec. (1950)[a] [h : m : s, ° : ′ : ″]	Array configuration	UV coverage [kλ]	HPBW[b] [arcsecs]	rms[c] [mJy/beam]	rms[d] [mJy/beam]
IRAS 03282	...	03:28:15.2, +30:35:14	CLE	3–36	5.5×4.3	76	0.29
IRAS 04166	B 213	04:16:37.8, +27:06:29	CLU	3–145	4.8×4.2	45	0.26
RNO 43 MM	L 1582B	05:29:30.6, +12:47:35	CLEH	3–68	5.3×4.7	52	0.36
CB 68	L 146	16:54:27.2, −16:04:44	CLH	3–62	8.4×5.0	71	0.41
L723 VLA2	...	19:15:41.8, +19:06:45	CLE	3–36	5.5×4.5	81	0.33
CB 188	...	19:17:54.1, +11:30:02	CLEU	3–127	4.4×4.1	55	0.27
CB 224	L 1100	20:35:30.6, +63:42:47	CL	3–36	5.4×5.1	97	0.37
CB 230	L 1177	21:16:53.7, +68:04:55	CL	3–36	7.1×6.4	63	0.30
CB 244	L 1262	23:23:48.5, +74:01:08	CL	3–36	6.3×5.2	86	0.39

[a]Reference position for figures and tables in the paper.
[b]Synthesized FWHM beam size with robust weighting.
[c]1 σ noises in the N_2H^+ (1-0) maps.
[d]1 σ noises in the 3 mm dust continuum maps.

and 1σ rms levels of ~ 70 mJy/beam (see Table 2.2). Further analysis and figures were done with the GILDAS[1] software package. With CLASS (part of GILDAS), we have developed a semi-automatic fitting routine which allows the derivation of reliable and very accurate velocity fields from the 7-hyperfine component line complex. Assuming that bulk rotation is the dominating motion, the velocity fields are then used to derive the rotation axis and the specific angular momentum of the cores.

2.3 Results

2.3.1 Morphology of N_2H^+ cores

Figure 2.1 shows the 3 mm continuum images for the nine sources. The combined dust continuum results will be published in a separate paper by Launhardt, Sargent, Zinnecker & Chen (2008, in prep.; hereafter LSZC08). N_2H^+ emission is detected from all nine targeted objects. Figure 2.2 shows the distribution of the velocity-integrated intensity of N_2H^+ towards the nine cores. The emission was integrated over all seven components, using frequency masks that completely cover velocity gradients within the sources. All objects are spatially associated with mm dust continuum sources, indicative of embedded protostars and their accretion disks. The positions of the mm continuum sources are indicated by crosses in Figure 2.2. We find that in seven of the nine objects the mm continuum source lies within the half maximum level of the N_2H^+ emission. The two exceptions are CB 188 (the only Class I object in our sample) and CB 244. This good general agreement indicates that N_2H^+ cannot be significantly depleted like, e.g., CO and CS (see Bergin et al. 2001; Caselli et al. 1999).

We also measured mean FWHM radii of the integrated N_2H^+ emission. The mean FWHM core radii R were measured as $A^{1/2}/\pi$, where A is the core area at the half maximum level, corrected for the beam size. Except for CB 188, all sources exhibit quite compact N_2H^+ emission regions with mean FWHM radii of 1200−3500 AU (see Table 2.4). The average radius in our sample is $\langle R \rangle = 2000 \pm 800$ AU, which is much lower than the average value found by Caselli et al. (2002; hereafter CBMT02) for their sample of starless cores (~ 10000 AU) observed with single-dish observations (beam size $\sim 54''$), but similar to the radius of Class 0 sources IRAM 04191+1522 (~ 2400 AU) and NGC 1333 IRAS 4B (~ 1800 AU) observed with PdBI by Belloche et al. (2002) and Di Francesco et al. (2001), respectively.

However, when viewed in detail, all sources in our sample show a complex, often multi-peaked structure. For example, IRAS 03282, IRAS 04166, and CB 230 each have two separated peaks in the region enclosed by the half maximum intensity level, with the mm continuum source located between the two peaks. In RNO 43, CB 68, CB 224, and CB 244 the main peak of N_2H^+ emission offsets by $5-10''$ from the mm continuum sources. Only in L723 VLA2 there is no positional discrepancy between the N_2H^+ and mm continuum emission. The individual sources are discussed in detail in Section 2.4.1.

[1] http://www.iram.fr/IRAMFR/GILDAS

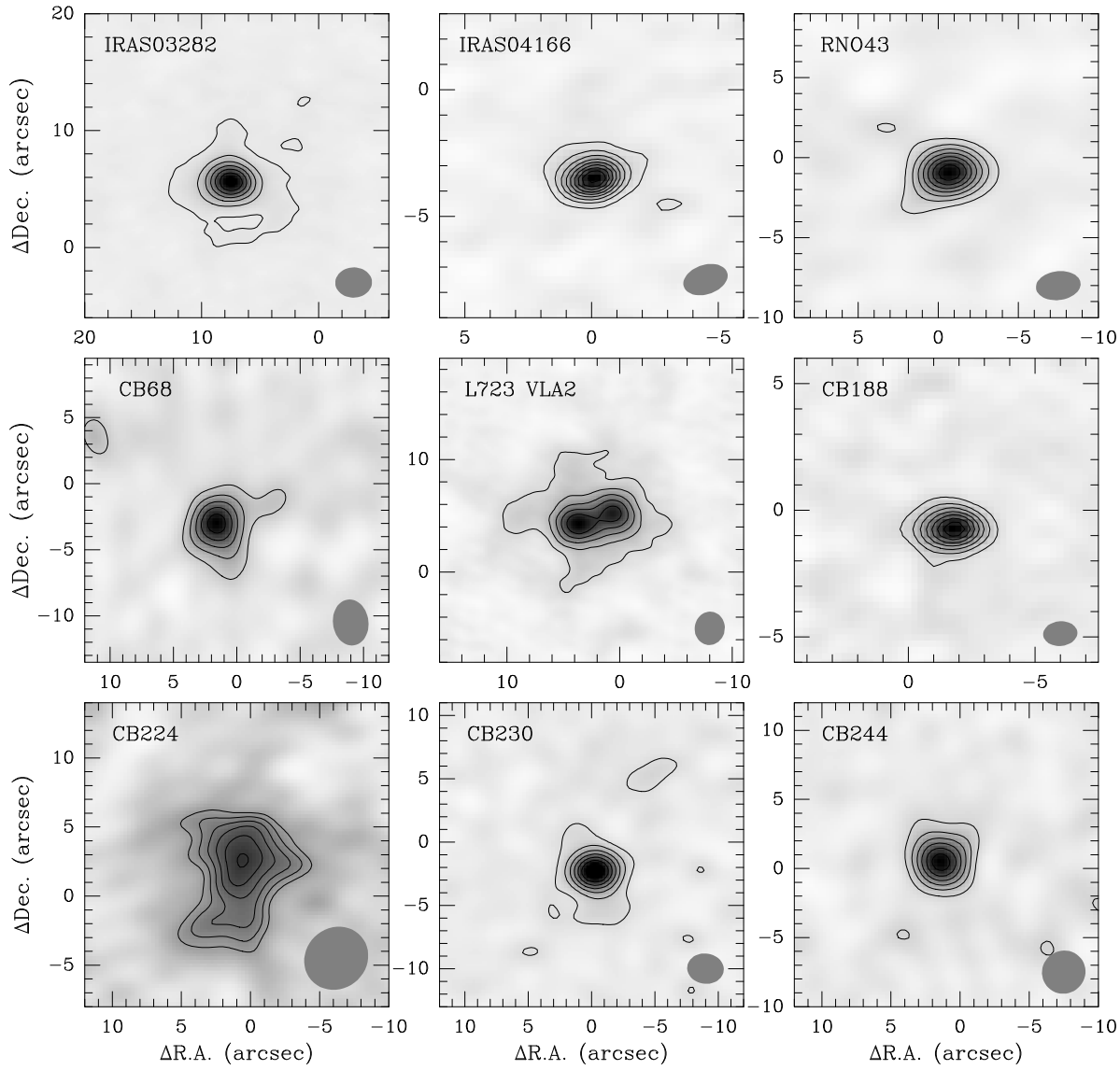

Figure 2.1: OVRO 3 mm dust continuum images of all nine target sources. Contours start at $\sim 3\,\sigma$ (see Table 2.2) with steps of $\sim 2\,\sigma$. OVRO synthesized beam sizes are shown as grey ovals in each map.

2.3.2 Masses and column densities

Figure 2.3 shows the N_2H^+ spectra at the position of maximum intensity in each map. The N_2H^+ (1−0) line complex consists of seven hyperfine structure components, which have been detected in all sources. However, in several sources like, e.g., L723 VLA2 (see below), the line width is larger than the separation between hyperfine components, so that some lines are blended. The hyperfine fitting program in CLASS (Forveille et al. 1989), with the frequencies adopted from Caselli et al. (1995) and weights adopted from

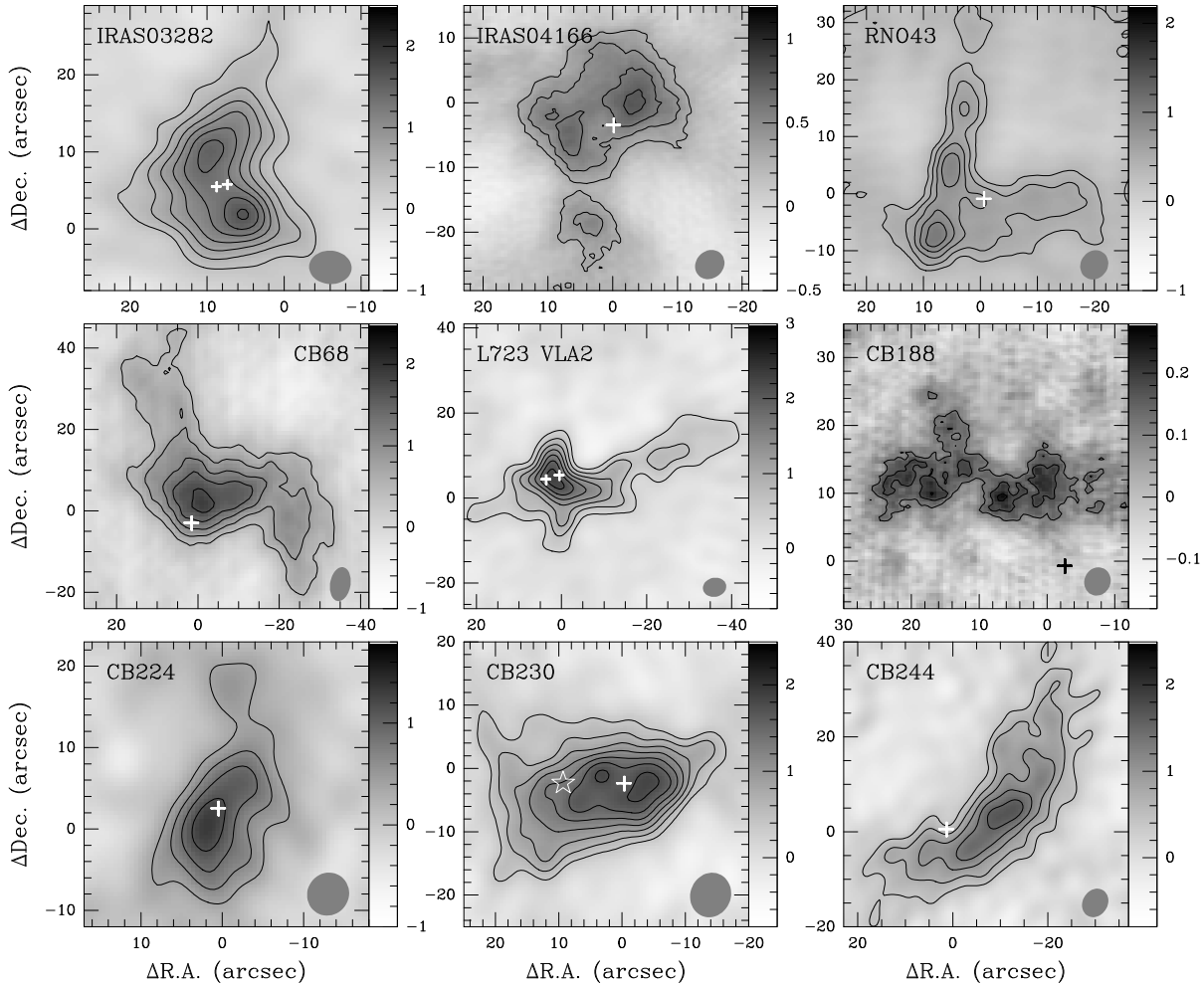

Figure 2.2: Maps of the N_2H^+ (1−0) intensity integrated over the seven hyperfine components for the nine protostars. The unit of the scale is [Jy beam^{-1} km s^{-1}]. Contours start at $\sim 3\,\sigma$ with steps of $\sim 2\,\sigma$ (see Table 2.2). OVRO synthesized beam sizes are shown as grey ovals in each map. Crosses in the maps represent the peaks of 3 mm dust continuum emission (except IRAS 03282, in which the crosses indicate the peaks of 1.3 mm dust emission; see Fig. 2.7). The asterisk in CB 230 marks the positions of the secondary protostar observed at 7 μm with ISOCAM (not detected at 3 mm, see Launhardt 2001 and Fig. 2.10).

Womack et al. (1992), has been used to determine LSR velocities ($v_{\rm LSR}$), intrinsic line width ($\triangle v$; corrected for instrumental effects), total optical depths ($\tau_{\rm tot}$), and excitation temperatures ($T_{\rm ex}$). These parameters are listed in Table 2.3. Here $\tau_{\rm tot}$ is the sum of the peak optical depths of the seven hyperfine components (see Benson & Myers 1989). The optical depth of the main N_2H^+ ($J\,F_1\,F = 1\,2\,3 \longrightarrow 0\,1\,2$) component, which is equal to $0.259\tau_{\rm tot}$, is found to be small (≤ 0.5) at the intensity peak for all sources. Hence the N_2H^+ emission can be considered optically thin everywhere. The excitation temperature, $T_{\rm ex}$, was calculated to be $4.1 - 5.7$ K at the peak positions, using a main-

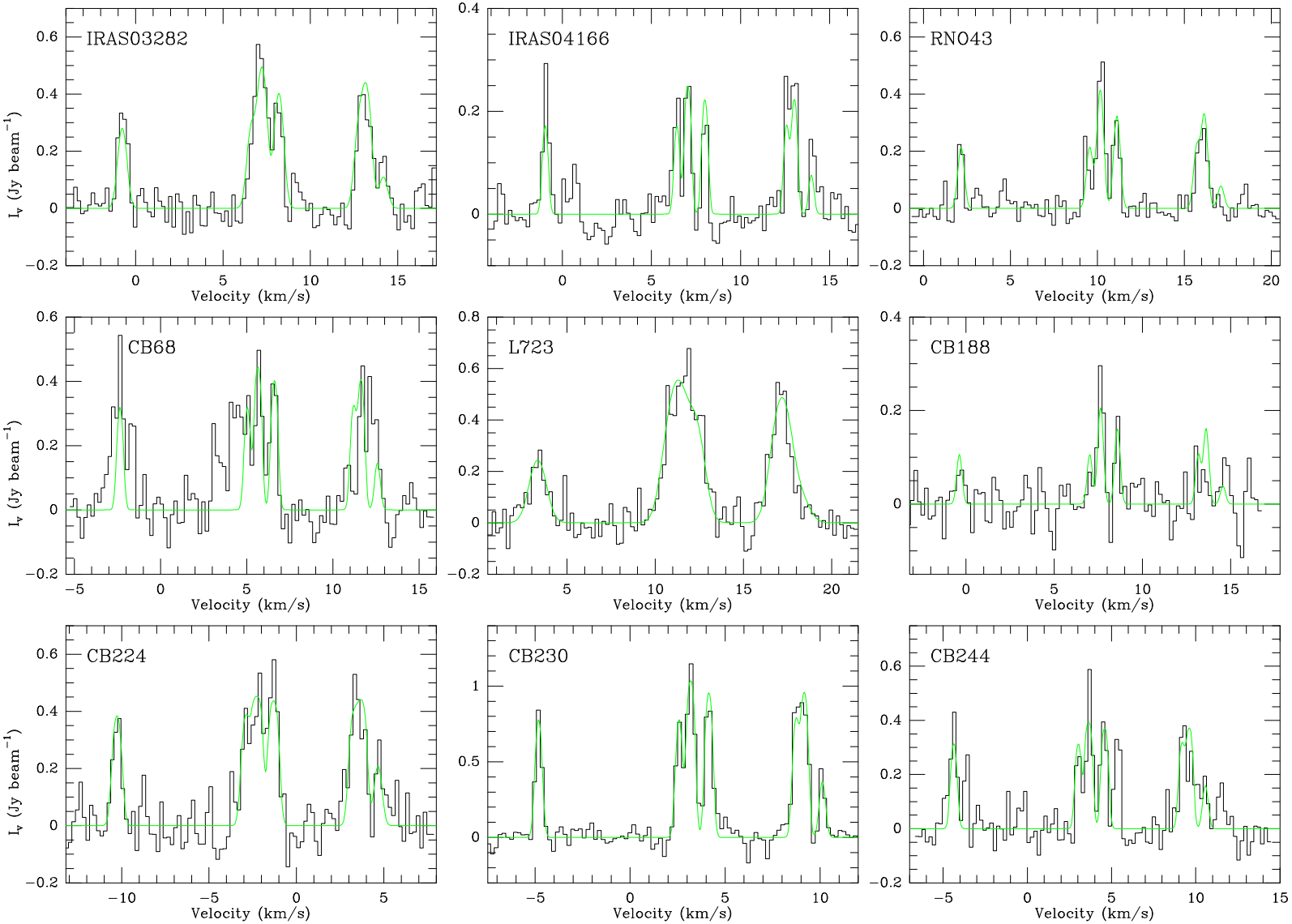

Figure 2.3: N_2H^+ spectra at the peak position of the nine observed protostars. Green curves show the hyperfine structure line fitting. Fitting results are given in Table 2.3.

Table 2.3: Parameters from N_2H^+ (1-0) spectral fitting

Source Name	$V_{\rm LSR}{}^a$ [km s^{-1}]	$T_{\rm ex}{}^a$ [K]	$\tau_{\rm tot}{}^a$	$\triangle v^a$ [km s^{-1}]	$\triangle v_{\rm mean}{}^b$ [km s^{-1}]	$\triangle v_{\rm NT}{}^c$ [km s^{-1}]
IRAS 03282	6.89±0.01	4.98±0.05	1.38±0.08	0.51±0.03	0.29±0.01	0.26±0.02
IRAS 04166	6.64±0.02	4.08±0.13	1.76±0.18	0.34±0.01	0.32±0.01	0.29±0.02
RNO 43	9.77±0.01	5.15±0.25	0.77±0.01	0.41±0.02	0.39±0.01	0.37±0.02
CB 68	5.26±0.04	4.25±0.04	1.38±0.09	0.37±0.04	0.33±0.01	0.30±0.02
L723 VLA2	11.00±0.02	5.74±0.21	0.78±0.03	1.07±0.04	0.51±0.01	0.49±0.02
CB 188	7.23±0.02	4.58±0.08	0.73±0.04	0.38±0.03	0.31±0.01	0.28±0.02
CB 224	−2.65±0.01	4.61±0.04	1.75±0.08	0.50±0.03	0.47±0.01	0.45±0.02
CB 230	2.78±0.01	5.49±0.13	1.54±0.04	0.36±0.01	0.29±0.01	0.26±0.02
CB 244	3.24±0.01	4.93±0.11	1.09±0.16	0.38±0.02	0.45±0.02	0.43±0.03

[a]Value at the intensity peak. The error represents 1 σ error in the hyperfine fitting.
[b]Mean line width for each object (see § 2.3.4).
[c]Non-thermal line width for each object at the given gas temperature (10 K; see § 2.3.4).

beam efficiency $\eta_{\rm B} = 0.7$ (Padin et al. 1991). The average $\langle T_{\rm ex} \rangle \sim 4.9$ K in our sample is similar to what has been found with single-dish observations for dense cores by CBMT02 (~ 5.0 K).

Assuming that the observed N_2H^+ line widths are not dominated by systematic gas motions, the virial mass of the cores has been calculated as:

$$M_{\rm vir} = \frac{5}{8ln2} \frac{R \triangle v_{\rm m}^2}{\alpha_{\rm vir} G}, \tag{2.1}$$

where G is the gravitational constant, R is the FWHM core radius, and $\triangle v_{\rm m}$ is the line width of the emission from an "average" particle with mass $m_{\rm ave} = 2.33$ amu (assuming gas with 90% H_2 and 10% He). The coefficient $\alpha_{\rm vir} = (3-p)/(5-2p)$, where p is the power-law index of the density profile, is corrected for deviations from constant density (see Williams et al. 1994). In our calculations, we assume $p = 1.5$ and $\alpha_{\rm vir} = 0.75$ (see André et al. 2000). $\triangle v_{\rm m}$ can be derived from the observed spectra by

$$\triangle v_{\rm m}^2 = \triangle v_{\rm mean}^2 + 8ln2 \frac{kT_{\rm ex}}{m_{\rm H}} (\frac{1}{m_{\rm av}} - \frac{1}{m_{\rm obs}}), \tag{2.2}$$

where $\triangle v_{\rm mean}$ is the observed mean line width (obtained through Gaussian fitting to the distribution of line widths versus solid angle area; see Table 2.3 and section 2.3.4) and $m_{\rm obs}$ is the mass of the emitting molecule (here we use $m_{N_2H^+} = 29$ amu). The corresponding hydrogen density of the $n_{\rm H_2}$ has been calculated assuming a uniform density spherical core with radius R (given in Table 2.4). The derived virial masses $M_{\rm vir}$ in our sample range from 0.3 to 1.2 $M_\odot$, with a mean value of 0.6 $M_\odot$. The corresponding hydrogen densities $n_{\rm H_2}$ range from 7.4 to 81 $\times 10^5$ cm^{-3}. Both $M_{\rm vir}$ and $n_{\rm H_2}$ values for each source are listed in Table 2.4.

The N_2H^+ column density has been calculated independently from the line intensity using the equation given by Benson et al. (1998):

$$N(N_2H^+) = 3.3 \times 10^{11} \frac{\tau \triangle v T_{\rm ex}}{1 - e^{-4.47/T_{\rm ex}}} \, ({\rm cm}^{-2}), \tag{2.3}$$

Table 2.4: Size, density, and mass

Source	R [AU]	$M_{\rm vir}$ [$M_\odot$]	$\langle n_{\rm H_2}\rangle^a$ [$\times 10^5\,{\rm cm^{-3}}$]	$N(N_2H^+)$ [$\times 10^{12}\,{\rm cm^{-2}}$]	$M_{\rm N_2H^+}$ [$\times 10^{-10}\,M_\odot$]	$X(N_2H^+)$ [$\times 10^{-10}$]
IRAS 03282	1703	0.42	22.6	1.81	1.57	5.11
IRAS 04166	1232	0.30	43.6	0.96	0.31	1.41
RNO 43 MM	3530	1.21	7.4	0.82	2.32	2.60
CB 68	1440	0.37	33.7	0.93	0.51	1.83
L723 VLA2	1272	0.65	84.4	2.84	1.89	3.96
CB 188	1763	0.44	21.6	0.57	0.46	1.42
CB 224	1329	0.57	64.7	1.95	2.07	4.97
CB 230	2762	0.71	9.0	1.52	3.86	7.41
CB 244	1774	0.72	34.9	0.96	0.69	1.30

[a]Mean density, computed from R and $M_{\rm vir}$ (see § 2.3.2)

where τ is the total optical depth, $\triangle v$ is the intrinsic line width in km s^{-1}, and $T_{\rm ex}$ is the excitation temperature in K. The gas-phase N_2H^+ mass of the core can then be calculated from $M_{\rm N_2H^+} \approx N(N_2H^+)_{\rm peak} \times {\rm m}_{\rm N_2H^+} \times {\rm d}^2 \times \Omega_{\rm FWHM}$, where d is the distance from the Sun and $\Omega_{\rm FWHM}$ is the area enclosed by the contour level at 50% of the peak value for each core.

From the ratio of N_2H^+ mass to virial mass, we derived the average fractional abundance of N_2H^+ in each core: $X(N_2H^+) = M_{\rm N_2H^+}/M_{\rm H_2}$, where $M_{\rm H_2} = M_{\rm vir}/1.36$, the factor 1.36 accounting for He and heavier elements. The values are listed in Table 2.4. The average value $\langle X(N_2H^+)\rangle \sim 3.3 \times 10^{-10}$ in our sample is close to that found by CBMT02 for their sample of dense cores ($\sim 3 \times 10^{-10}$).

2.3.3 Velocity fields

Based on the hyperfine fitting program in CLASS, we have developed a semi-automated quality control and spectra fitting routine that computes the mean radial velocity, line width, and line intensity at each point of the map where N_2H^+ is detected ($> 2\sigma$ noise). Figure 2.4 shows the mean velocity fields for the eight Class 0 objects in our sample, obtained from this line fitting routine. The N_2H^+ emission from CB 188, the only evolved (Class I) object in our sample, is too faint and fuzzy to give a reliable velocity field.

In Class 0 protostars, the effects of infall, outflow, rotation, and turbulence are generally superimposed. Of these, turbulence and infall normally broaden the lines but do not produce systematic velocity gradients. On the other hand, systematic velocity gradients are usually dominated by either rotation or outflow. In Fig. 2.4, we therefore also show the outflow information for each source. We want to mention that many other studies usually do not take this kind of caution. Figure 2.4 shows that five objects (IRAS 04166, RNO 43, L723 VLA2, CB 230, and CB 224) have well-ordered velocity fields with symmetrical gradients, while 3 objects (IRAS 03282, CB 68, and CB 244) have more complex velocity fields. Two objects (RNO 43 and CB 230) with well-ordered velocity fields have gradients roughly perpendicular to the axis of outflow,

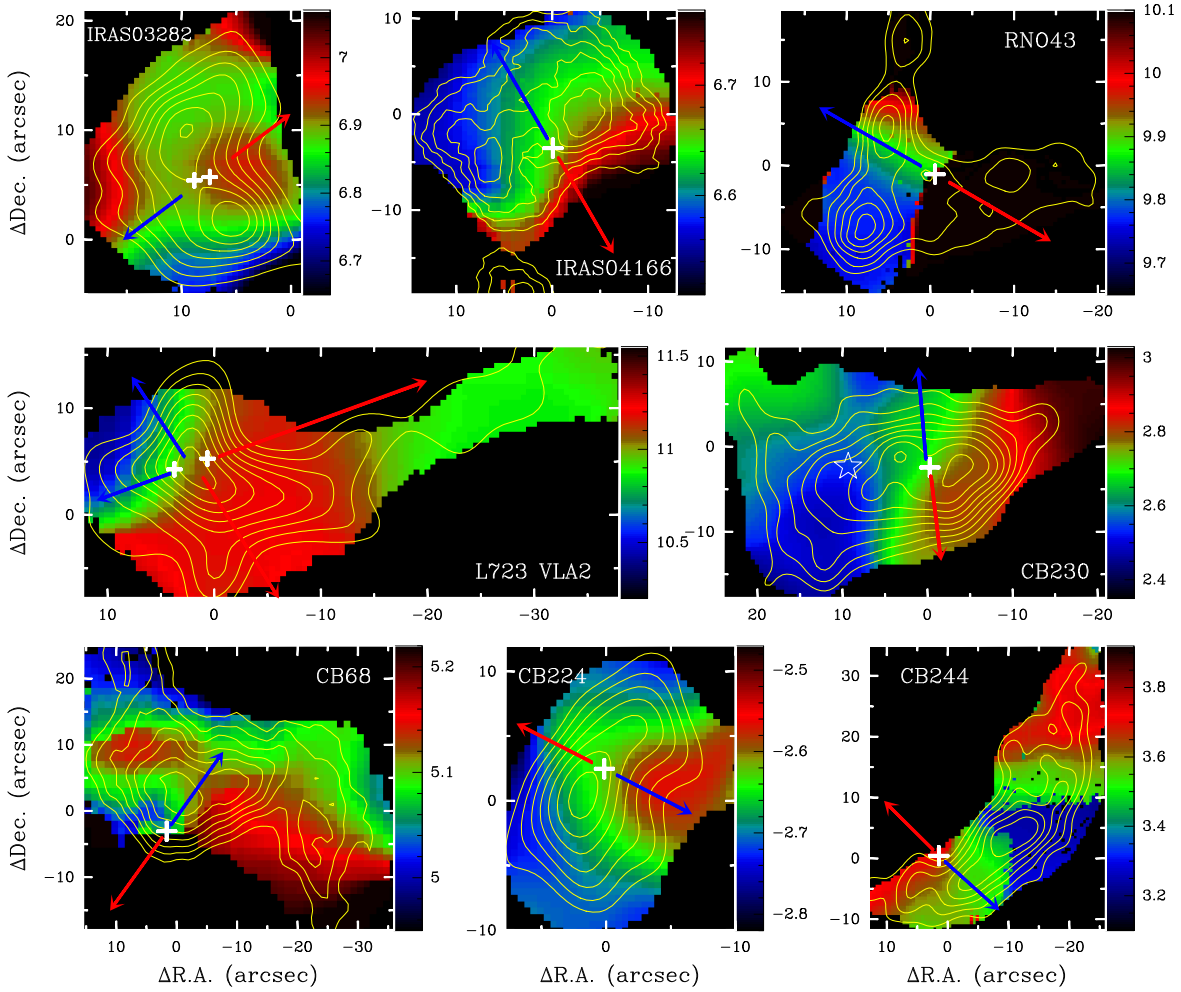

Figure 2.4: N_2H^+ velocity field maps of 8 Class 0 protostars. The unit of the scale is km s^{-1}. The contours in each map are from Fig. 2.2, but range from 30% to 99% of the peak intensity by the step of 10%. The crosses in each are same as them in Fig. 2.2. The red and blue arrows show the directions of the red- and blue-shifted outflow for each source (see text).

while two objects (IRAS 04166 and L732 VLA2) have gradients basically parallel and one object (CB 224) anti-parallel to the outflow direction.

Assuming that the mean direction of the bulk angular momentum is preserved in the collapse from the core to the disk, we would expect outflows to emerge perpendicular to the rotation velocity gradients. Thus, if the velocity field is dominated by rotation, we would see the velocity gradient to be perpendicular to the outflow axis, like seen in RNO 43 and CB 230. If gradients are parallel to the outflow axis and with the same orientation, it is likely that we see outflow motions rather than rotation, like in IRAS 04166 and L723 VLA2. In these cases, a possible underlying rotation velocity gradient must be smaller than the observed effective gradient. Following these arguments, we treat those gradients parallel to the outflow as upper limits to the rotation gradient. The details of the velocity field for each source are described in section 2.4.1.

Table 2.5: Velocity gradient and specific angular momentum

Source	mean velocity [km s^{-1}]	g [km s^{-1} pc^{-1}]	Θ_g [degree]	g_r [km s^{-1}]	J/M [$\times 10^{-3}$ km s^{-1} pc]
IRAS 03282	6.91	<6.6	70.8±1.2	0.11	<0.12
IRAS 04166	6.64	<12.5	-134.2±1.7	0.15	<0.12
RNO 43 MM	9.72	5.8±0.1	-23.1±1.0	0.21	0.45
CB 68	5.15	<10.3±0.2	161.2±0.8	0.15	<0.13
L723 VLA2	11.03	<24.2	-139.2±0.2	0.30	<0.24
CB 224	-2.67	<11.2	-82.7±1.0	0.15	<0.12
CB 230	2.69	8.8±0.1	-54.0±0.4	0.24	0.42
CB 244	3.51	<22.9	51.2±0.2	0.41	<0.45

A least-squares fitting of velocity gradients has been performed for the objects in our sample using the routine described in Goodman et al. (1993; hereafter GBFM93). The fitting results are summarized in Table 2.5. Listed are in column (2) the mean velocity of the cores, in columns (3) and (4) the magnitude of the velocity gradient g and its direction Θ_g (the direction of increasing velocity, measured east of north), and in column (5) the total velocity shift across the core gr (i.e., the product between g and core size R).

2.3.4 Line widths

Figure 2.5 shows the distribution of line widths versus solid angle area in the maps for the nine protostars in our sample. The mean line width for each source is then derived through Gaussian fitting to the distribution and is listed in Table 2.3. We find that the mean line width in our sample is $0.29 - 0.51$ km s^{-1}, with an average of ~ 0.37 km s^{-1}.

The FWHM thermal line width for a gas in LTE at kinetic temperature $T_{\rm K}$ is given by

$$\triangle v_{\rm th}^2 = 8ln2\frac{kT_{\rm K}}{m_{\rm obs}}, \tag{2.4}$$

where k is the Boltzmann constant and $m_{\rm obs}$ is the mass of the observed molecule. Assuming a kinetic gas temperature of 10 K (see Benson & Myers 1989), the thermal contribution to the N_2H^+ line width is ~ 0.13 km s^{-1}. The typical non-thermal contribution to the line width ($\triangle v_{\rm NT} = \sqrt{\triangle v_{\rm mean}^2 - \triangle v_{\rm th}^2}$) is then ~ 0.35 km s^{-1} , which is about 2.5 times larger than the thermal line width (see discussion in § 2.4.2).

Figure 2.6 shows the spatial distribution of the N_2H^+ line width for those six Class 0 sources which are not highly elongated (axial ratios ≤ 2). In most cases the line widths are roughly constant within the interiors of the cores and broader line widths occur only at the edges. This is consistent with both the NH_3 observations by Barranco & Goodman (1998) and the physical picture described by Goodman et al. (1998) that the star-forming dense cores are "velocity coherent" regions of nearly constant line width. The exception, CB 230, is discussed in § 2.4.

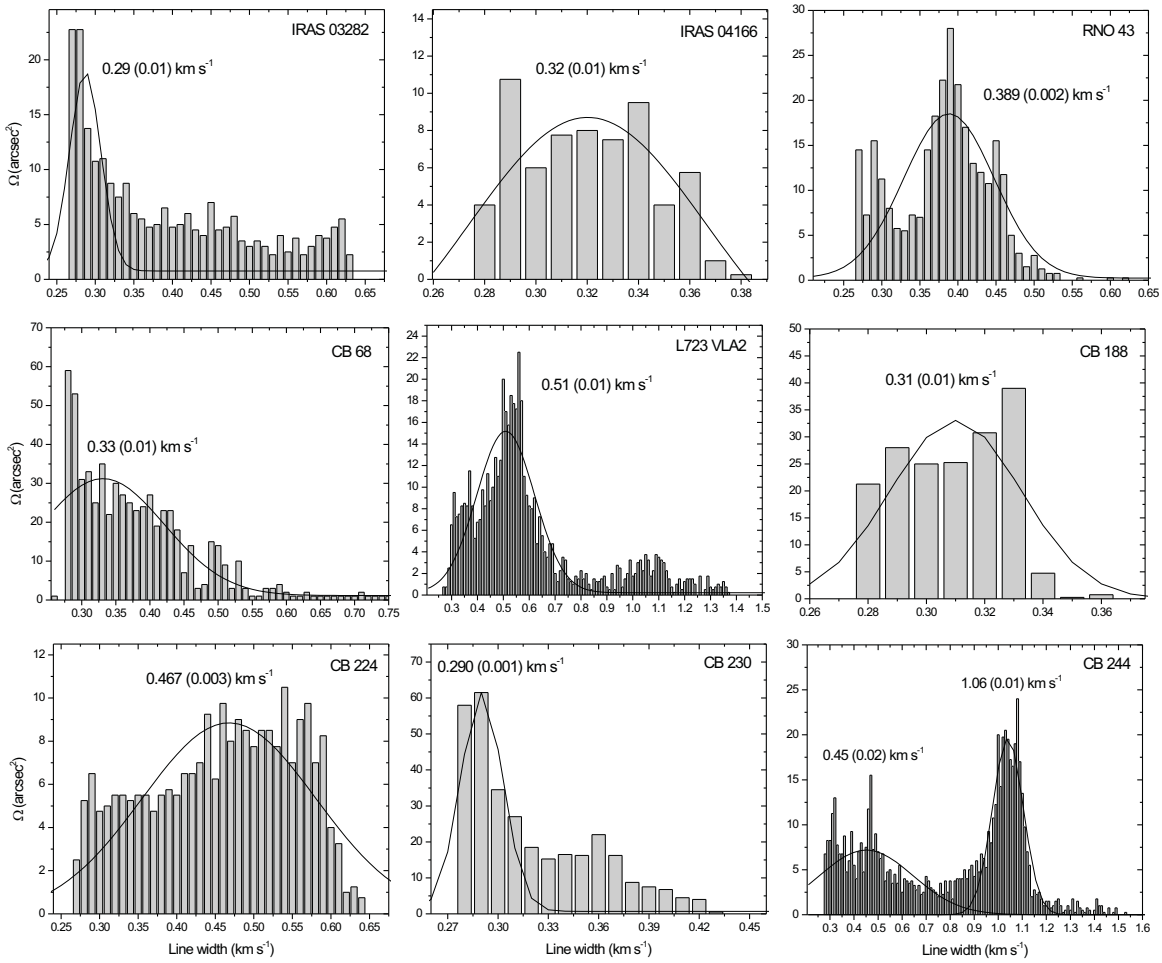

Figure 2.5: Diagrams of the correlation between line width and solid angle area for the nine protostars in our sample. Black solid curves and values in each map show the results of Gaussian fitting.

2.4 Discussion

2.4.1 Description of individual sources

2.4.1.1 IRAS 03282+3035

IRAS 03282 is one of the youngest known Class 0 protostars (André et al. 2000). It is located in the western part of the Perseus molecular cloud complex at a distance of $\sim$ 300 pc (Motte & André 2001). Its bolometric luminosity and total envelope mass are estimated to be $L_{\rm bol} \sim 1.2\,L_{\odot}$ and $M_{\rm env} \sim 2.9\,M_{\odot}$, respectively (Shirley et al. 2000). IRAS 03282 drives a highly collimated bipolar molecular outflow at P.A. $\sim -37^{\circ}$ with kinematic age $\sim 10^4$ yr (Bachiller et al. 1994).

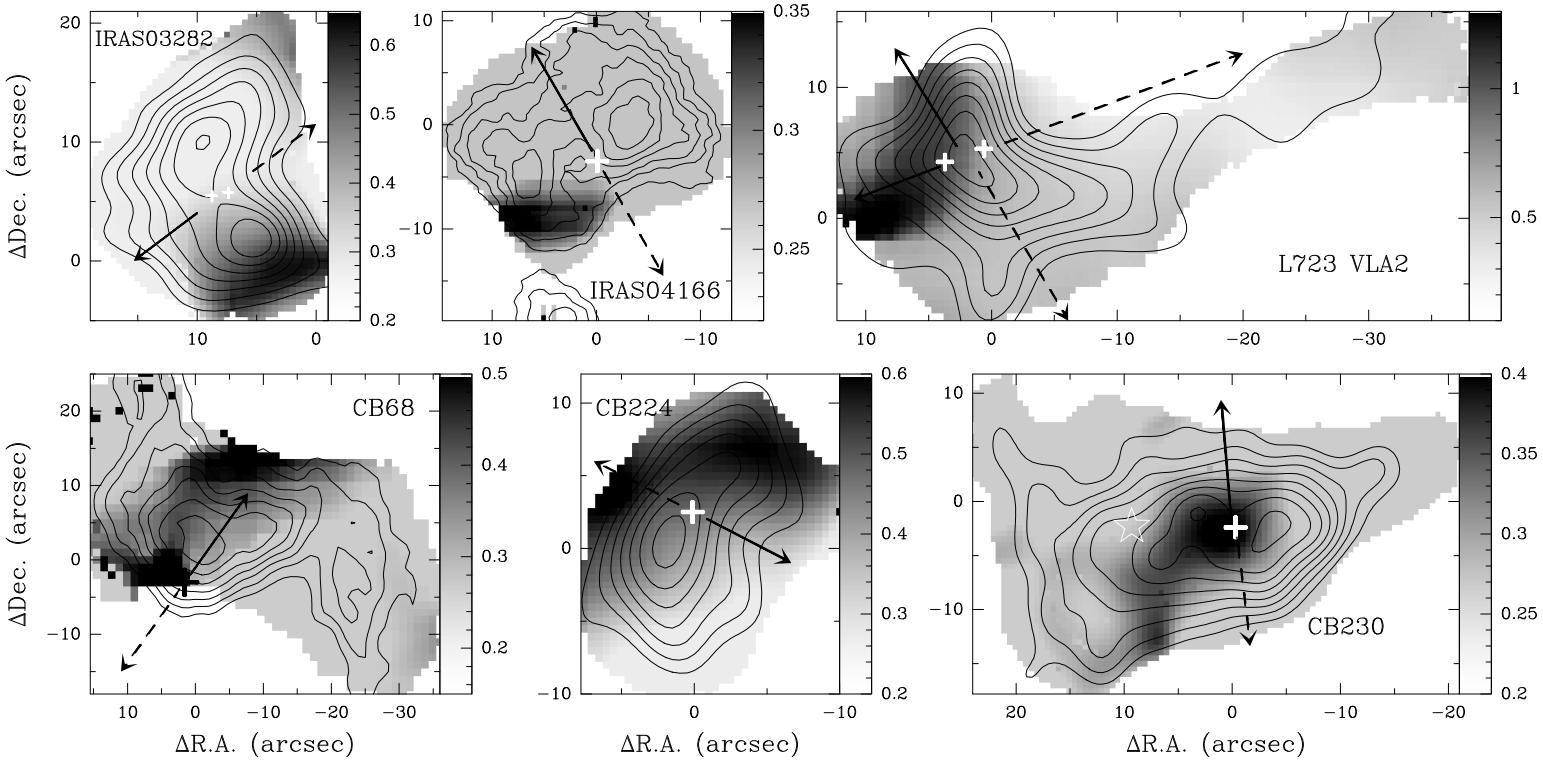

Figure 2.6: Line widths distribution of 6 Class 0 protostars in our sample. The unit of the scale is km s^{-1}. The crosses in each map are same as them in Fig. 2.2 and the contours in each map are same as them in Fig. 2.4. Solid and dashed lines in each map show the direction of blue- and red-shifted outflow, respectively.

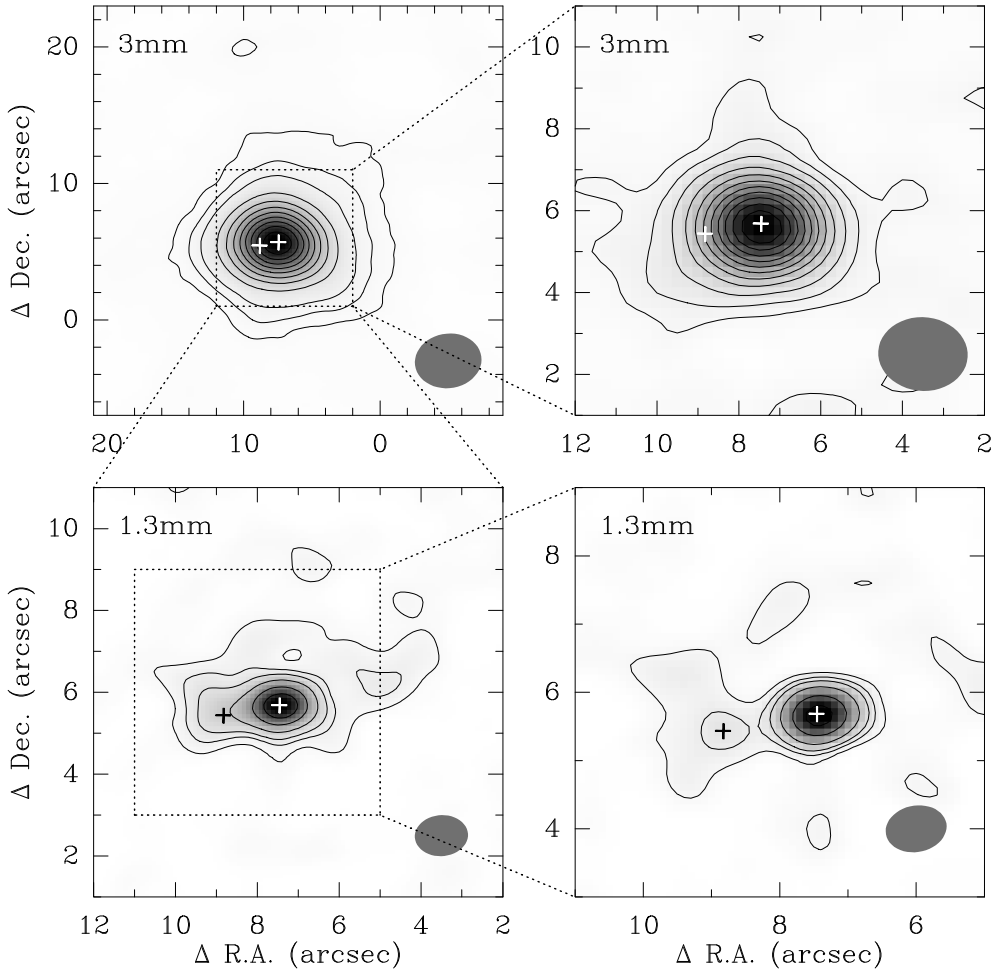

Figure 2.7: OVRO dust continuum images at 1.3 mm and 3 mm of IRAS 03282. Contour levels in all images start at $3\,\sigma$ rms. OVRO synthesized beam sizes are shown as grey ovals. The center positions of MM1 (7.″5, 5.″7) and MM2 (8.″9, 5.″4) are marked by crosses. Top left: naturally *uv* weighted 3 mm continuum image (robustness parameter +1); $\sigma = 0.3$ mJy/beam. Top right: uniformly *uv* weighted 3 mm continuum image (robustness parameter −0.5); $\sigma =$ 0.45 mJy/beam. Bottom left: naturally *uv* weighted 1.3 mm continuum image (robustness parameter +1); $\sigma = 2.4$ mJy/beam. Bottom right: uniformly *uv* weighted 3 mm continuum image (robustness parameter 0); $\sigma = 2.5$ mJy/beam.

The N_2H^+ intensity map of IRAS 03282 shows a molecular cloud core that is hourglass shaped and elongated along P.A. $\sim$ 30 degree, i.e., nearly perpendicular to the axis of the large-scale CO outflow (see Fig. 2.4). We interpret the hourglass shape as effect of the outflow, which re-releases CO from grain surface back into the gas phase. CO, in turn, destroys the N_2H^+ molecule (Aikawa et al. 2001). Our OVRO 1.3 mm dust continuum images reveal two mm sources, MM1 and MM2, located between the two N_2H^+ emission peaks (see Fig. 2.7). The mass ratio and the angular separation of this binary protostar are 0.23 and 1.″5 ($\sim$ 450 AU at a distance of 300 pc), respectively (LSZC08). The velocity field of IRAS 03282 does not show a symmetrical gradient

and the red-shifted N_2H^+ emission lobe to the northwest of the mm sources matches exactly the red-shifted ^{13}CO lobe, implying that the N_2H^+ emission in this region is affected by the outflow. Correspondingly, we treat the observed total velocity gradient as upper limit to rotation (see § 2.3.3). Figure 2.6 shows the line width distribution of IRAS 03282. The average line width across the source is $\sim 0.4 \pm 0.1\,\mathrm{km\,s^{-1}}$ and reaches $0.7\,\mathrm{km\,s^{-1}}$ towards the southern edge of the core.

2.4.1.2 IRAS 04166+2706

IRAS 04166 is a Class 0 protostar associated with the small dark cloud B 213 in the Taurus molecular cloud complex at a distance $\sim$ 140 pc (Mardones et al. 1997). Its bolometric luminosity and total envelope mass are $L_{\rm bol} \sim 0.4\,L_\odot$ and $M_{\rm env} \sim 1.0\,M_\odot$, respectively (Shirley et al. 2000). IRAS 04166 drives a highly collimated, extremely high velocity (up to 50 km $\mathrm{s^{-1}}$) bipolar molecular outflow at P.A. $\sim 30°$ (Tafalla et al. 2004).

The N_2H^+ intensity map of IRAS 04166 shows the same hourglass shape and orientation relative to the outflow as IRAS 03282. We interpret it in the same way. The N_2H^+ velocity field of IRAS 04166 shows a symmetric gradient, which however matches the red- and blue-shifted CO outflow lobes (see Fig. 2.4). As for IRAS 03282, we treat the observed total velocity gradient as upper limit to rotation.

2.4.1.3 RNO 43 MM

The millimeter continuum source RNO 43 MM is associated with the dark cloud L 1582B and the very cold IRAS point source 05295+1247 (detected only at 60 and 100 μm). The cloud is physically connected to the λ Ori molecular ring located at a distance of $\sim$ 400 pc (Zinnecker et al. 1992). RNO 43 MM is the origin of a 3.4 pc long Herbig-Haro flow (HH 243, HH 244, and HH 245; Reipurth et al. 1997) and drives a collimated bipolar molecular outflow at P.A. $\sim 60°$ (Arce & Sargent 2004). From its spectral energy distribution (SED) and the ratio of sub-mm to bolometric luminosity, RNO 43MM has been classified a Class 0 source (Bachiller 1996). Its bolometric luminosity and total envelope mass are estimated to be $L_{\rm bol} \sim 6.0\,L_\odot$ and $M_{\rm env} \sim 0.4\,M_\odot$, respectively (Zinnecker et al. 1992).

Our N_2H^+ intensity map of RNO 43MM shows a V-shaped core with two lobes, extending $\sim 20''$ to the north and west, respectively (see Fig. 2.2). The western lobe exhibits much higher (redder) mean velocities than the rest of the core, and is outside the plot scale of Fig. 2.4 (11 up to $20\,\mathrm{km\,s^{-1}}$). This jump in velocity probably means that the western lobe belongs to another molecular cloud layer in this direction. In the inner core region (included at 50% contour level), the velocity field exhibits a symmetric structure with a gradient of $\sim 5.8\,\mathrm{km\,s^{-1}\,pc^{-1}}$ at P.A. $\sim -13°$, approximately perpendicular to the axis of outflow, suggesting rotation (see Fig. 2.4). The total velocity shift across the inner core is $\sim 0.4\,\mathrm{km\,s^{-1}}$.

2.4.1.4 CB 68

CB 68 (LDN 146) is a small Bok globule located in the outskirts of the ρ Oph dark cloud complex at a distance of 160 pc (Clemens & Barvainis 1988; Launhardt & Henning 1997). The dense core of the globule exhibits strong, extended, centrally peaked sub-mm/mm dust continuum emission (Launhardt & Henning 1997; Launhardt et al. 1998; Vallée, Bastien, & Greaves 2000) and is associated with the cold IRAS point source 16544−1604. The central source, which was classified as a Class 0 protostar, drives a weak, but strongly collimated bipolar molecular outflow at P.A. $\sim 142°$ (Wu et al. 1996; Mardones et al. 1997; Vallée et al. 2000).

Our N_2H^+ intensity map shows a compact source of about $9''$ FWHM radius, which peaks very close to the mm continuum position. In addition, it exhibits two armlike extensions to northeast and southwest. The velocity field of CB 68 is relatively complicated and shows no systematic gradient which could be interpreted as rotation. There is also no clear correlation with the outflow. As for IRAS 03282, we derive only an upper limit for the rotation velocity gradient.

2.4.1.5 L723 VLA2

L723 is a small, isolated dark cloud located at a distance of 300 ± 150 pc (Goldsmith et al. 1984). The IRAS point source 19156+1906, at the center of the cloud core, is associated with strong far-infrared (Davidson 1987), sub-mm (Shirley et al. 2000), and mm continuum emission (Cabrit & André 1991; Reipurth et al. 1993) and was classified as a Class 0 protostar with a bolometric luminosity $L_{\rm bol} \sim 3.0\,L_\odot$ (Shirley et al. 2000). Anglada et al. (1991) detected two radio continuum sources (VLA 1 and VLA 2) with $15''$ separation, both located within the error ellipse of the IRAS position. However, only VLA 2 was found to be associated with dense gas in the cloud core (Girart et al. 1997). Centered at the IRAS position is a large quadrupolar molecular outflow with two well-separated pairs of red and blue lobes: a larger pair at P.A. $\sim 110°$ and a smaller pair at P.A. $\sim 30°$ (see Lee et al. 2002 and references therein). While several scenarios have been proposed to explain the quadrupolar morphology of the large-scale CO outflow, the discovery of a thermal radio jet at the position of VLA 2 (Anglada et al. 1996) and of a large-scale $H_2S(1)$ bipolar flow (Palacios & Eiroa 1999), both aligned with the larger pair of CO outflow lobes at P.A. $\sim 110°$, as well as new high-resolution CO observations (Lee et al. 2002), clearly favor the presence of two independent outflows.

Our OVRO 3 mm dust continuum image reveals two separate compact sources with a projected separation of $\sim 3\farcs16$ (~ 950 AU at a distance of 300 pc) in L723 VLA2 (see Fig. 2.8). The results derived from *uv* plane modeling suggest that the two compact sources represent two accretion disks embedded in a common envelope. The circumstellar masses of the disks and the common envelope are calculated to be $0.05\,M_\odot$, $0.04\,M_\odot$, and $1.2\,M_\odot$, respectively. OVRO ^{12}CO (1–0) image suggests two biconical limb-brightened arcs at the center of the outflow (see Fig. 2.9). Our results strongly supports the scenario that the quadrupolar outflow is driven by an equal-mass binary protostar. More details of this source will be discussed in a separate paper (Launhardt, Chen, & Sargent, et al. 2008a, to be submitted).

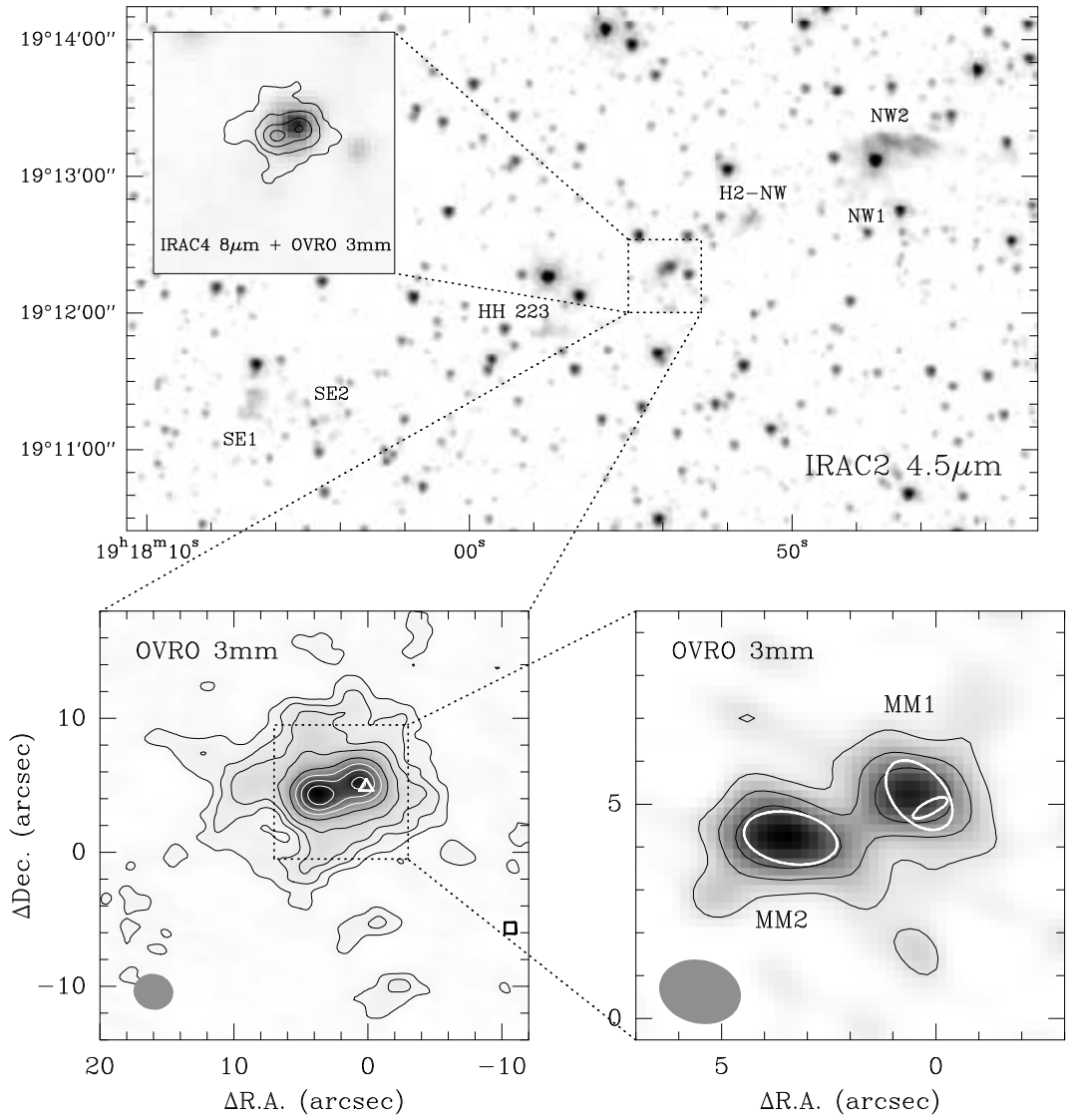

Figure 2.8: Top: *Spitzer* IRAC2 (4.5 μm) and IRAC4 (8.0 μm) images of L723 (taken from *Spitzer* archive), overlaid with naturally weighted OVRO 3 mm continuum contours. The positions and names of H_2 objects are referred to Lopez et al. (2006). Bottom left: OVRO naturally *uv* weighted 3 mm continuum image. Contour levels are at 2, 4, 6, 9 ... $\times 1\sigma$ rms where $\sigma = 0.17$ mJy/beam. OVRO synthesized beam size is shown as grey oval ($3\farcs0 \times 2\farcs7$). Positions of VLA 1 and VLA 2 are marked by a black square and white triangle, respectively. Bottom right: higher-resolution image (robust *uv* weighting, beam size $1\farcs9 \times 1\farcs5$) of the two embedded accretion disks after the envelope has been subtracted (see text). Contours are at the same levels as in the left panel with $\sigma = 0.3$ mJy/beam. Large white ellipses show the orientation and size of beam-deconvolved gaussian fits to the two sources. The small white ellipse shows the size and orientation of the thermal radio jet L 723 VLA 2 (Anglada et al. 1996).

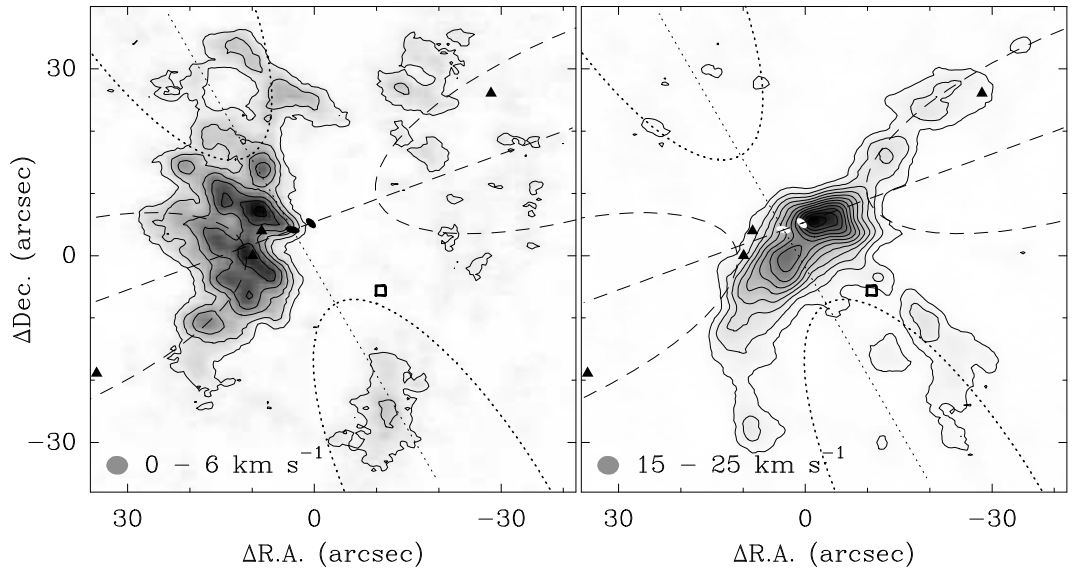

Figure 2.9: Map of integrated ^{12}CO (1–0) emission in blue-shifted (left) and red-shifted (right) outflow line wings of L 723. Contour levels are at 5, 10, 15 ... $40 \times 1\sigma$ rms where $\sigma = 80$ mJy/beam. Beam sizes are shown as grey ovals. Two small black (left) and white (right) ovals show the size and orientation of two embedded accretion disks. Black square and triangles show the positions of radio object VLA 1 and H_2 objects (Palacios & Eiroa 1999), respectively.

The N_2H^+ intensity map of L723 VLA2 shows a compact source of about 8″ FWHM diameter, which peaks between the two mm continuum sources. In addition, it shows a long extension to the northwest along the direction of larger outflow. The mean velocity difference between the two continuum positions is $\sim 0.4\,\mathrm{km\,s^{-1}}$. However, the overall velocity field of L723 VLA2 shows that the red-shifted N_2H^+ emission matches exactly the red-shifted emission of two outflows and the velocity gradient is basically in the same direction as the outflow, suggesting that the outflow has a strong effect on the N_2H^+ emission. As for IRAS 03282, we therefore treat the observed total velocity gradient as upper limit to rotation. The line widths distribution of L723 VLA2 is shown in Fig. 2.6. The line widths are about 0.5 $\mathrm{km\,s^{-1}}$ in the northwest extension, $0.6 - 1.0$ $\mathrm{km\,s^{-1}}$ across the core, and reach $1.5\,\mathrm{km\,s^{-1}}$ towards the eastern edge of the core. We suggest that the relatively large line widths in this source are the result of strong outflow-envelope interaction.

2.4.1.6 CB 188

CB 188 is a small dark globule at a distance of ~ 300 pc, which harbors a Class I young stellar object (Launhardt & Henning 1997). A small ($\leq 2'$) CO outflow with overlapping red and blue lobes was detected by Yun & Clemens (1994), suggesting the object is seen close to pole-on. In our N_2H^+ intensity map, CB 188 shows a complex clumpy structure (see Fig. 2.2). It also has the weakest N_2H^+ emission in our survey (also see the spectra in Fig. 2.3). This could imply that N_2H^+ is destroyed during

the evolution from Class 0 to Class I, e.g., due to release of CO from grain surfaces in outflows (see Aikawa et al. 2001). We do not further discuss this source in this chapter.

2.4.1.7 CB 224

CB 224 is a Bok globule located at a distance of ~ 400 pc (Launhardt & Henning 1997). Two mm sources were detected in our OVRO survey at an angular separation of $20''$ (LSZC08). The northeast mm source (not shown here) is associated with a cold IRAS source 20355+6343 ($3.9\,L_\odot$; Launhardt & Henning 1997), but has no N_2H^+ emission detected. The southwest source shown in our images, which is classified a Class 0 object (LSZC08), drives a collimated ^{13}CO bipolar outflow at P.A. $\sim -120°$ (Chen et al., in prep.).

The N_2H^+ intensity map of CB 224 shows the same hourglass morphology perpendicular to the outflow as IRAS 03282 and IRAS 04166 (but slightly more asystematic in intensity). There is a clear and systematic velocity gradient across the core, but the lines of constant velocity are curved in a "C" shape (see Fig. 2.4). The velocity field cannot be solely interpreted by rotation. The CO outflow seems to have no effect on the N_2H^+ velocity field because it is oriented in the opposite direction. We speculate that the velocity field is due to a combination of rotation and core contraction. The HCO^+ observations in De Vries et al. (2002) indeed indicated signs of infall motions in CB 224.

2.4.1.8 CB 230

CB 230 (L 1177) is a small, bright-rimmed Bok globule at a distance of 400 ± 100 pc (Wolf et al. 2003a). The globule contains a protostellar core of total mass $\sim 5\,M_\odot$ and exhibits signatures of mass infall (Launhardt et al. 1997, 1998, 2001). Magnetic field strength and projected direction in the dense core are $B = 218 \pm 50$ μG and P.A. $= -67°$, respectively (Wolf et al. 2003a). The dense core is associated with a large-scale collimated CO outflow at P.A. $= 7°$ of dynamical age $\sim 2 \times 10^4$ yr (Yun & Clemens 1994). The Mid-IR image of CB 230 suggests the presence of two deeply embedded young stellar objects separated by $\sim 10''$ (Launhardt 2004; see Fig. 2.10). Only the western source was detected at 1.3 mm and 3 mm dust continuum, suggesting that the mass of a possible accretion disk around eastern source is below the detection limit. Two bright near-infrared reflection nebulae are associated with the embedded objects, but the stars are not directly detected at wavelengths shorter than $5\,\mu$m. CB 230 is probably a transition object between Class 0 and I.

Our N_2H^+ intensity map shows that the molecular cloud core is elongated East-West. The velocity field map shows a clear velocity gradient across the core of $\sim 8.8\,\mathrm{km\,s^{-1}\,pc^{-1}}$ increasing from east to west along the long axis, i.e., roughly perpendicular to the outflow axis. This strongly supports the view that the two MIR sources form a protobinary system which is embedded in the N_2H^+ core. This core in turn rotates about an axis perpendicular to the connecting line between the two protostars and parallel to the main outflow. Fig. 2.6 shows that the line width distribution exhibits a strong peak at the position of the 3 mm continuum source. Together with the velocity field shown in Fig. 2.4, this can be understood as the result of Keplerian

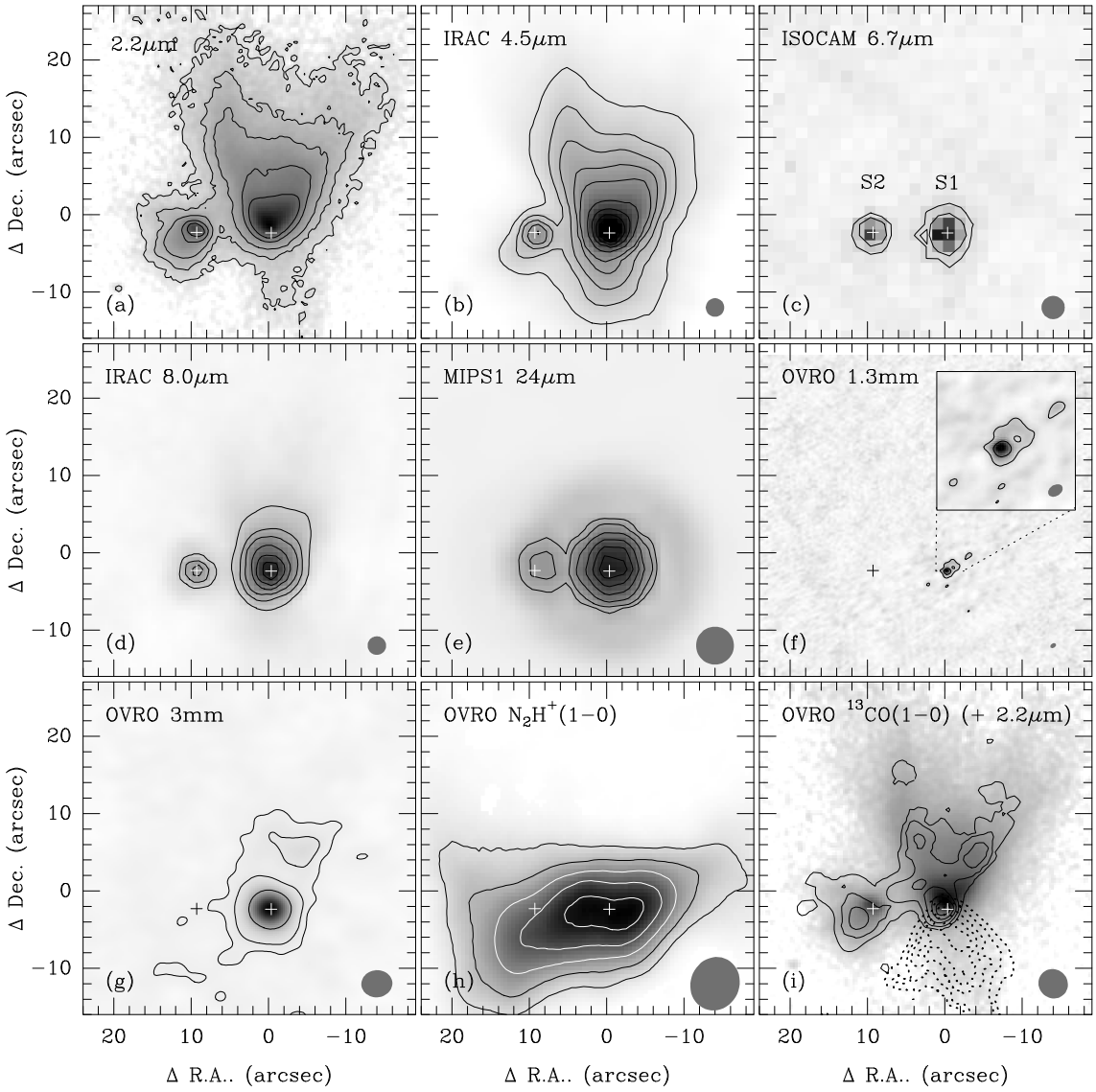

Figure 2.10: CB 230 - Summary of observational results. From top to bottom, left to right: **a)** 2.2 μm continuum surface brightness distribution of the NIR reflection nebula. The "+" signs in this and all other panels mark the locations of the embedded protostars. **b)** *Spitzer* IRAC 2 image (taken from *Spitzer* archive), showing the shock-excited 4.5 μm infrared emission. The grey ellipse in this and the following panels illustrates the FWHM beam size of the observations. **c)** ISOCAM image of the 6.7 μm emission. The thermal mid-infrared emission from hot circumstellar dust is the only tracer that directly reveals both embedded sources S1 (E) and S2 (W). **d) and e)** *Spitzer* images of the 8.0 μm and 24 μm emission, tracing hot dust in the immediate environment of the sources. **f)** At 1.3 mm (dust continuum emission) and angular resolution of $0\farcs6$, point-like emission with a small envelope is detected only towards S1. **g)** 3 mm dust emission at $4''$ resolution. **h)** Integrated intensity of the N_2H^+ (1–0) line emission. **i)** ^{13}CO (1–0) line wing emission, overlayed on the grey-scale NIR image (panel a). Solid contours: blue-shifted emission ($0.7 - 2.5\,\mathrm{km\,s^{-1}}$) dashed contours: red-shifted emission ($3.1 - 5.2\,\mathrm{km\,s^{-1}}$).

rotation. Morphology and kinematics of this source will be discussed more detailed in a separate paper (Launhardt, Chen, & Sargent, et al. 2008b, to be submitted).

2.4.1.9 CB 244

CB 244 (L 1262) is a Bok globule located at a distance of ~ 180 pc (Launhardt & Henning 1997). It is associated with a faint NIR reflection nebula and a cold IRAS point source, and was classified as Class 0 protostar. Its bolometric luminosity and total envelope mass are estimated to be $L_{\rm bol} \sim 1.1\,L_\odot$ and $M_{\rm env} \sim 3.3\,M_\odot$, respectively (Launhardt & Henning 1997). CB 244 drives a bipolar molecular outflow at P.A. $\sim -130°$ (Yun & Clemens 1994; Chen et al., in prep.).

The N_2H^+ intensity map of CB 244 shows an elongated structure in the direction from Northwest to Southeast, approximately perpendicular to the direction of outflow (see Fig. 2.4). The velocity field of CB 244 exhibits a complicated structure and maybe dominated by effects other than rotation. As for other sources, we assume that the total observed velocity gradient puts an upper limit to the rotation. The distribution of line widths for this source shows two distinct peaks (see Fig. 2.5). The smaller line widths originate from the southeastern part of the core where the protostar is embedded, while the larger widths are found in the northwestern extension only (see Fig. 2.2). Therefore, we adopted the smaller peak value as representative for CB 244.

2.4.2 Turbulent motions

At a kinetic gas temperature of 10 K, the typical non-thermal line width in our sample (0.35 km s^{-1}) is about 2.5 times lager than the thermal line width (0.13 km s^{-1}) (see §2.3.4). The origin of the non-thermal line width in such cores is subject of an ongoing debate in the literature. Generally, turbulence is suggested to be the main contribution (see e.g., Barranco & Goodman 1998 and Goodman et al. 1998), but infall, outflow, and rotation may also contribute to the non-thermal line width.

With the exception of L723 VLA2, there appears to be no spatial correlation between regions of increased line width and outflow features (see Fig. 2.6). CB 230 may represent a special case where Keplerian rotation of a large circumstellar disk causes the large non-thermal line width in the central region (see Fig. 2.6). To avoid a bias from localized line-broadening due to outflows and/or Keplerian rotation, we estimated the observed mean line width through Gaussian fitting to the distribution of line widths versus area in the maps (see Fig. 2.5). The non-thermal contribution to these mean line widths are listed in Table 2.3. We assume that these mean non-thermal line widths are dominated by turbulence. The thermal FWHM line width of an "average" particle of mass 2.33 $m_{\rm H}$, which represents the local sound speed, would be ~ 0.44 km s^{-1} at 10 K. The mean observed non-thermal line width is ~ 1.3 times smaller than this value, which means that turbulence in these cores is subsonic.

Figure 2.11 shows the distribution of non-thermal line width $\triangle v_{\rm NT}$ with core size R for the objects in our sample, together with the dense cores from GBFM93 and CBMT02. It shows that high-level (supersonic) turbulence normally occurs in large-scale cores only. In the cores traced by NH_3 ($R > 20000$ AU ~ 0.1 pc), the non-thermal line widths decrease with core size with a power-low index ~ 0.2, while in those traced

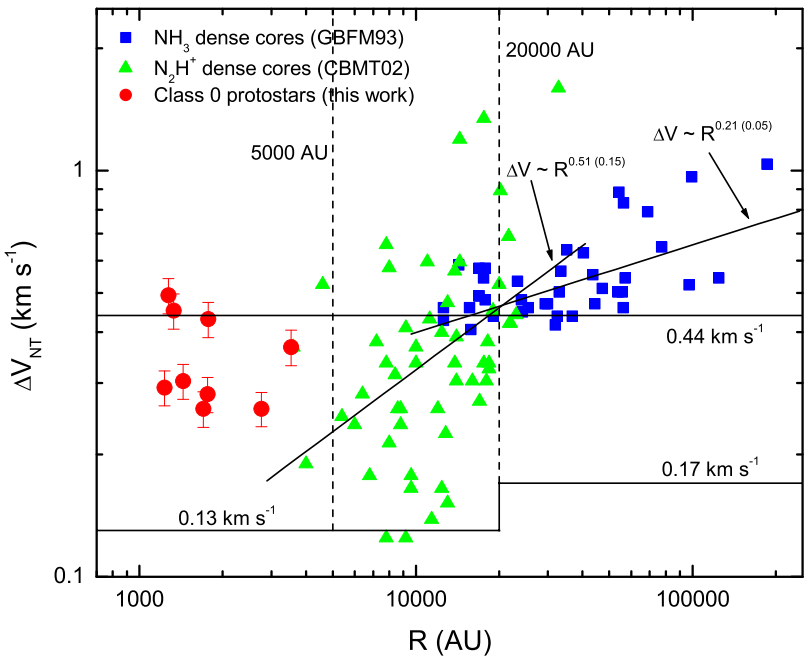

Figure 2.11: Non-thermal line width $\triangle V_{NT}$ versus size R of dense molecular cloud cores. Data of NH_3 (open squares) and N_2H^+ (open triangles) dense cores are adopted from GBFM93 and CBMT02, respectively. Solid lines marked 0.13, 0.17 and 0.44 km s^{-1} represent thermal line widths of N_2H^+, NH_3, and 2.33 m_H mass "average" particle at 10 K, respectively. The fit to the GBFM93 and CBMT02 data results in power-law indexes of 0.21±0.05 and 0.51±0.15, respectively. The levels (p-values) of statistical significance are $<$ 0.01% (GBFM93) and $\sim$ 0.1% (CBMT02), respectively.

by N_2H^+ (CBMT02; 5000 AU $< R <$ 20000 AU), the line widths decrease with an index of $\sim$ 0.5. This suggests that non-thermal motions are more quickly damped in smaller cores (see also Fuller & Myers 1992). Comparing our data with CBMT02, we find that the relation between line width and core size no longer holds at $R <$ 10000 AU, suggesting the inner parts of dense cores are "velocity coherent". The radius at which the gas becomes "coherent" is less than 0.1 pc, as suggested in Goodman et al. (1998). Also note that the mean non-thermal line width in our sample (0.35 km s^{-1}) is even larger than the widths in some larger scale dense cores (see Fig. 2.11). We speculate that the heating from an internal protostar, as well as related activities, like e.g., infall and/or outflow, contribute to the line widths in these protostellar cores.

2.4.3 Systematic gas motions

For the fragmentation model of binary star formation, some initial angular momentum must be present, otherwise the cores will collapse onto a single star. The source of this angular momentum is generally suggested to be the bulk rotation of the core. As

suggested in the earlier study by GBFM93, rotation is a common feature of dense cores in molecular clouds. In our observations, most objects show well-ordered velocity fields with symmetric gradients and the motions of several objects could be interpreted as bulk rotation. The results from our ATCA and PdBI observations show similar well-ordered velocity fields (see Chapter 3 and Chapter 4), supporting the view in GBFM93.

Up to now only a few Class 0 objects have been studied in detail kinematically. Typical examples are the nearby, isolated object IRAM 04191 (Belloche et al. 2002), or NGC 1333 IRAS 4A (Di Francesco et al. 2001 and Belloche et al. 2006), which is actually a binary protostar at a separation of ~ 600 AU (Looney et al. 2000). Below, we analyze our eight Class 0 objects together with these two sources. Of the eight Class 0 targets, CB 230, IRAS 03828, and L723 VLA2 are resolved as binary protostars by our mm observations, while IRAS 04166, RNO 43, CB 68, CB 224, and CB 244 remain single or unresolved. We treat RNO 43 and CB 230 as objects which provide reliable rotation velocity gradients and take the other six measurements as upper limits. The ASURV[2] software package was used for the statistical analysis of the results. This package performs a "survival analysis" which takes into account upper limits and allows to compute a statistical sample mean. It must, however, be noted that two real measurements and six upper limits are not sufficient to derive statistically significant correlations.

The velocity gradients derived in our sample range from 5.8 to ≤ 24.2 km s^{-1} pc^{-1} (see Table 2.5). The mean value derived by the cumulative Kaplan-Meier (KM) estimator in ASURV is 7.0 ± 0.8 km s^{-1} pc^{-1}. This result is consistent with the gradients derived in IRAM 04191 (~ 7 km s^{-1} pc^{-1}) and IRAS 4A (~ 10 km s^{-1} pc^{-1}), but it is much larger than the velocity gradients of dense cores derived from single-dish observations in GBFM93 and CBMT02 ($1-2$ km s^{-1} pc^{-1}). The correlation between velocity gradient (g) and core size (R) is shown in Figure 2.12. It shows a clear trend with smaller cores ($R < 5000$ AU) having larger velocity gradients. Taking into account only RNO 43 and CB 230, the entire dataset could be fitted by a relation of $g \propto R^{-0.6\pm0.1}$, which is steeper than the slope of $\propto R^{-0.4}$ obtained by GBFM93 for the larger scale cores only. As expected, smaller (more evolved) protostellar cores rotate much faster than larger (prestellar) cores.

2.4.4 Constraints on angular momentum

Assuming that the velocity gradients are due to core rotation, the specific angular momentum J/M of the objects can be calculated with the following equation (see GBFM93):

$$J/M = \alpha_{\rm rot}\omega R^2 = \frac{2}{5+2\alpha}\frac{g}{sini}R^2 \approx \frac{1}{4}gR^2, \qquad (2.5)$$

where the coefficient $\alpha_{\rm rot} = 2/(5+2p)$, p is the power-law index of the radial density profile (here we adopt $p = 1.5$), g is the velocity gradient, and i is the inclination angle to the line of sight direction. Here we assume $sin\, i$ to be 1 for all sources. The derived specific angular momenta J/M for our eight Class 0 protostars are listed in column (6)

[2]ASURV Rev.1.2 (LaValley, Isobe & Feigelson 1992) is a software package which implements the methods presented in Feigelson & Nelson (1985). For details see http://astrostatistics.psu.edu/.

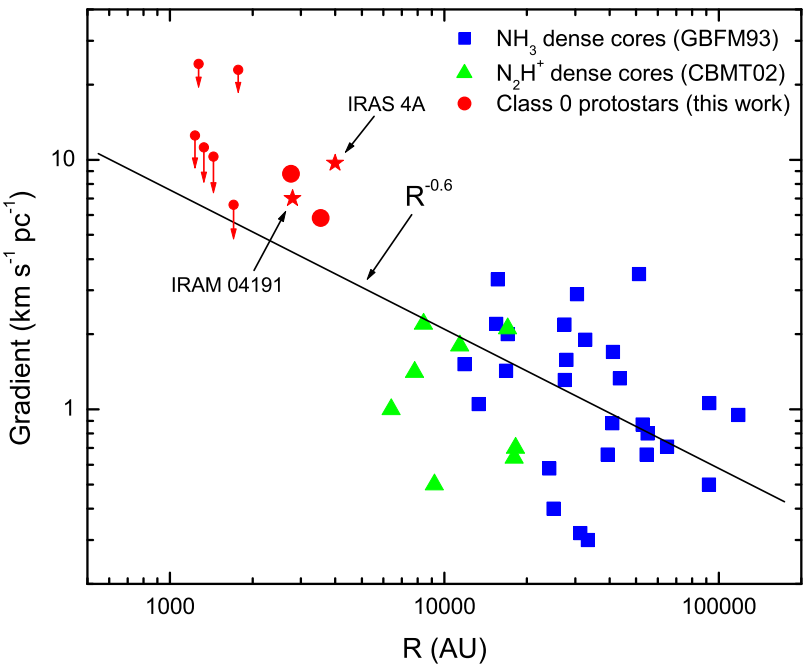

Figure 2.12: Mean velocity gradient versus size R of dense molecular cloud cores. Data of NH_3 (open squares) and N_2H^+ (open triangles) dense cores are adopted from GBFM93 and CBMT02, respectively. Data of IRAM 04191 and NGC1333 IRAS4A (asterisks) are adopted from Belloche et al. (2002; 2006). Solid line shows the fitting result with a power-law index of -0.6 ± 0.1.

in Table 2.5. We derived values between < 0.12 and 0.45×10^{-3} km s^{-1} pc, with a KM sample mean of $0.21 \pm 0.1 \times 10^{-3}$ km s^{-1} pc.

In Figure 2.13 we show the distribution of specific angular momentum versus size scale for Class 0 single (unresolved) and binary protostars (this work), together with molecular cloud cores, PMS binary stars, and single stars, etc. The data of NH_3 dense cores and N_2H^+ starless cores are from GBFM93 and CBMT02, respectively. For PMS binary stars, the specific orbital angular momenta are derived as $J/M = \sqrt{GM_BD}\times q/(1+q)^2$ (where M_B is the total stellar mass, D is the separation, and q is the mass ratio). Data of Class I and T Tauri binaries are from Chen et al. (2008, in prep.; see Chapter 5)[3]; data of very low-mass ($< 0.1\ M_\odot$) and brown dwarf binaries are from Burgasser et al. (2007). The specific angular momentum of Class I single stars is derived from $J/M = vR$, where v of 38 km s^{-1} and R of 2.7 $R_\odot$ are mean values from the sample of Class I stars in Covey et al. (2005) and adopted as representative values here.

[3]The masses of Class I and T Tauri binaries are dynamic masses. The angular momentum plotted in Fig. 2.11 for these binaries does not include the angular momentum from the stellar rotation.

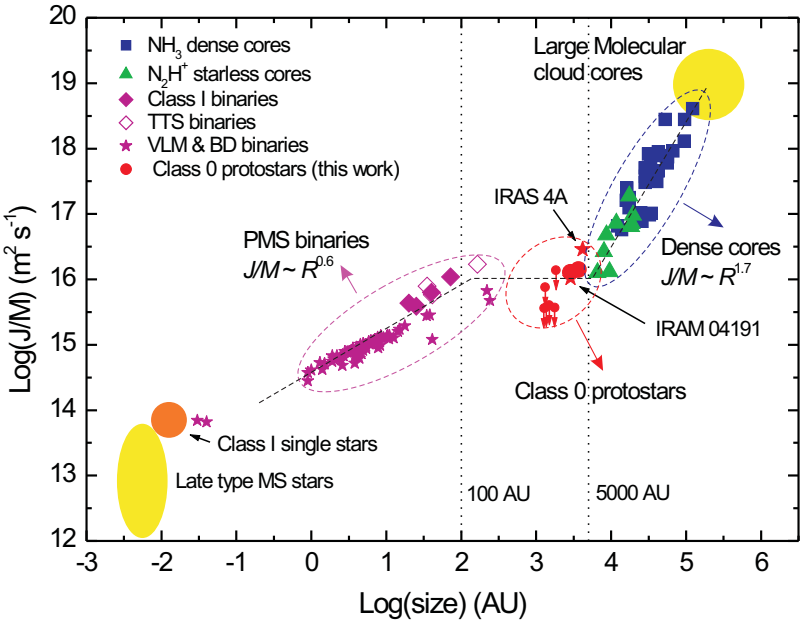

Figure 2.13: Distribution of specific angular momentum J/M versus size R of molecular cloud cores, protostars, and stars. For the dense cores, the specific angular momenta are derived from $J/M = 2/5\ (R^2 \times g)$ (see text). The data of the NH_3 dense cores are from Goodman et al. (1993); the data of the N_2H^+ starless cores are from Caselli et al. (2002). For the binary stars, the orbital specific angular momenta are derived from $J/M = \sqrt{GMD} \times q/(1+q)^2$ (see text). The data of Class I binaries and T Tauri binaries are from Chen et al. (2008, in prep.; see Chapter 5), and the masses are all dynamic masses; The data of very low-mass (< 0.1 $M_\odot$) and brown dwarf binaries are from Burgasser et al. (2007).

As shown in Fig. 2.13, there is a strong correlation between J/M and size scale in dense cores ($\geq$ 5000 AU). The data can be fitted with a power-law correlation of $J/M \sim R^{1.7 \pm 0.1}$, which is consistent with the index 1.6 $\pm$ 0.2 obtained by GBFM93. This means that in these dense cores the angular velocity is locked at a constant value to the first order, which is generally explained by the mechanism of magnetic braking (see Basu & Mouschovias 1994). In addition, Fig. 2.13 shows that the mean J/M value in this region is considerably ($\sim$ 2 magnitudes) larger than the typical orbital angular momentum of T Tauri binary systems. However, stars are not formed from the entire cloud (large dense cores), but only from the dense inner $R \leq 5000$ AU part of the cores that undergoes dynamical gravitational collapse and decouples from the rest of the cloud. Fig. 2.13 shows that such cores have almost the same specific angular momentum as the widest (few hundred AU) PMS binaries. But, there is a gap in size scale between the smallest prestellar cores and the widest binaries. We find that the specific angular momenta of Class 0 protostellar cores are located in this gap, but nearly indistinguishable from those of wide PMS binary systems, i.e., angular

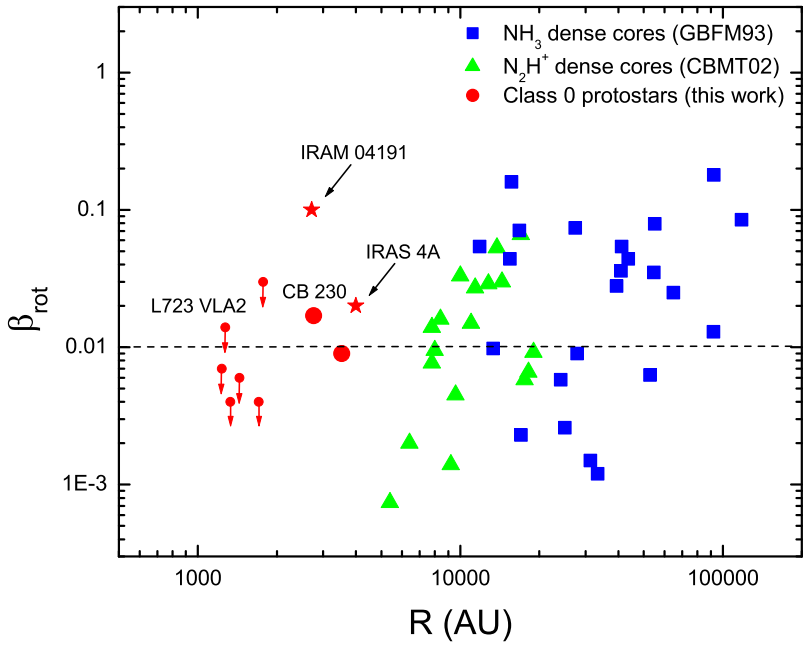

Figure 2.14: Ratio of rotational to gravitational energy $\beta_{\rm rot}$ versus size R. Data of NH_3 (open squares) and N_2H^+ (open triangles) dense cores are adopted from GBFM93 and CBMT02, respectively. Data of IRAM 04191 and NGC1333 IRAS4A (asterisks) are adopted from Belloche et al. (2002; 2006).

momentum is basically maintained (conserved) from the smallest prestellar cores via protostellar cores to wide PMS binary systems. In the context that most protostellar cores are assumed to fragment and form binary stars, this means that most of the angular momentum contained in the collapse region is transformed into orbital angular momentum of the resulting stellar binary system.

2.4.5 Energy balance

In this section we estimate the contribution of different terms to the total energy balance of the protostellar cores in our sample. In Table 2.6 we summarize the basic equations and the estimated ratios of the rotational, thermal, and turbulent energy to the gravitational potential energy. Here we assume a mean kinetic gas temperature $\sim$ 10 K for all objects. The masses and radii used in the equations are virial masses and FWHM radii listed in Table 2.4.

The ratios of thermal and turbulent energy to gravitational potential energy ($\langle\beta_{\rm therm}\rangle \approx 0.26$ and $\langle\beta_{\rm turb}\rangle \approx 0.15$) show that in these protostellar cores both thermal and turbulent contribution together appear to dominate the support of the cores, but the thermal contribution $\sim$ 2 times outweighs turbulence. The estimated $\beta_{\rm rot}$ values range from < 0.004 to 0.017, with a KM sample mean of $\sim 0.007 \pm 0.002$, which is much lower than

Table 2.6: Energy balance

Source	$E^a_{\rm grav}$ $[\times 10^{35} J]$	$\beta^b_{\rm rot}$	$\beta^c_{\rm therm}$	$\beta^d_{\rm turb}$	$\beta^e_{\rm vir}$
IRAS 03282	1.34	<0.004	0.33	0.11	−0.11
IRAS 04166	0.99	<0.007	0.33	0.14	−0.05
RNO 43 MM	5.51	0.009	0.24	0.16	−0.19
CB 68	1.29	<0.006	0.31	0.14	−0.08
L723 VLA2	4.36	<0.014	0.16	0.19	−0.27
CB 224	3.19	<0.004	0.19	0.19	−0.23
CB 230	2.40	0.017	0.31	0.11	−0.12
CB 244	3.91	<0.03	0.20	0.18	−0.18

[a]Gravitational potential energy: $E_{\rm grav} = \alpha_{\rm vir} GM^2/R$.
[b]$\beta_{\rm rot} = \frac{E_{\rm rot}}{E_{\rm grav}} = \frac{1}{2}\frac{\alpha_{\rm rot}}{\alpha_{\rm vir}}\frac{\omega^2 R^3}{GM} = 0.17\frac{g^2}{sin^2 i}\frac{R^3}{GM}$. Here we assume $sini = 1$ for all the objects.
[c]$\beta_{\rm therm} = \frac{E_{\rm therm}}{E_{\rm grav}}$ and $E_{\rm therm}$ is the thermal energy estimated from $E_{\rm therm} = \frac{3}{2} M \frac{kT}{\mu m_{\rm H}}$ (k is the Boltzman constant and $\mu = 2.33$ is the mean molecular weight).
[d]$\beta_{\rm turb} = \frac{E_{\rm turb}}{E_{\rm grav}}$ and $E_{\rm turb}$ is the turbulent energy estimated from the non-thermal line width $E_{\rm turb} = 3/2 M\sigma^2_{\rm NT}$ ($\sigma^2_{\rm NT} = \frac{\triangle v_{\rm turb}}{8ln2}$. Here we assume that the non-thermal line widths at the given temperature in our sample are from turbulence.
[e]$\beta_{\rm vir} = 2(\beta_{\rm rot} + \beta_{\rm therm} + \beta_{\rm turb}) - 1$.

$\beta_{\rm therm}$ and $\beta_{\rm turb}$. This suggests that rotation is not dominating in the support of the protostellar cores. When we apply the equilibrium virial theorem $2[E_{\rm therm} + E_{\rm turb} + E_{\rm rot}]$ $+ E_{\rm grav} = 0$ (in the absence of magnetic fields), we find that all the Class 0 protostellar cores in our sample are slightly supercritical (see Table 2.6).

Although the rotation energy is relatively small, it is thought to play an important role in the fragmentation process (see reviews by Bodenheimer et al. 2000 and Tholine 2002). In general, if $\beta_{\rm rot}$ is very large ($\beta_{\rm rot} \geq 0.25-0.3$), a gas cloud can be stable against dynamical collapse, potentially inhibiting fragmentation and star formation. However, if $\beta_{\rm rot}$ is very small, a cloud will not have enough rotational energy to experience fragmentation. Boss (1999) has shown that rotating, magnetized cloud cores fragment when $\beta_{\rm rot} > 0.01$ initially[4]. It should be noted that three sources in our sample might have a $\beta_{\rm rot} > 0.01$. Of these, CB 230 ($\beta_{\rm rot} \sim 0.017$) and L723 VLA2 ($\beta_{\rm rot} < 0.014$) have been resolved as binary protostars. On the other hand, IRAS 03282, a resolved binary protostar, has a very low $\beta_{\rm rot}$ (~ 0.004), and IRAS 04166, a single (unresolved) protostar, has $\beta_{\rm rot}$ value close to 0.01. Thus, our observations can neither confirm nor disprove a relation between $\beta_{\rm rot}$ and fragmentation (but see Chapter 6). This could be due to low-number statistics combined with observational uncertainties. Figure 2.14 shows the distribution of $\beta_{\rm rot}$ with core size R for our sample, together with the cores from GBFM93 and CBMT02. It shows that $\beta_{\rm rot}$ is roughly independent of R, as suggested before by GBFM93.

[4]Machida et al. (2005) find that the fragmentation does occur in rotating, magnetized clouds when $\beta_{\rm rot} \geq 0.04$, considering magnetic fields suppress fragmentation.

2.5 Conclusions

We present N_2H^+ (1-0) observations of nine isolated low-mass protostellar cores using the OVRO mm array. The main conclusions of this chapter are summarized as follows:

(1) N_2H^+ emission is detected in all target objects and the emission is spatially consistent with the thermal dust continuum emission. The mean excitation temperature of the N_2H^+ line is ~ 4.9 K. The mean FWHM core radius is $\langle R \rangle = 2000 \pm 800$ AU. The derived virial masses of the N_2H^+ cores in our sample range from 0.3 to 1.2 $M_\odot$, with a mean value of 0.6 $M_\odot$. The corresponding mean hydrogen number densities range from 10^6 to 10^7 cm^{-3}. The N_2H^+ column densities in our sample range from 0.6 to 2.8 $\times$ 10^{12} cm^{-2}, with a mean value of 1.4 $\times$ 10^{12} cm^{-2}. The average fractional abundances of N_2H^+, calculated by relating the N_2H^+ column densities derived from the line strength to the virial masses, was found to be $\sim 3.3 \times 10^{-10}$. This is consistent with the result obtained in other surveys with single-dish observations.

(2) The observed mean line widths range from 0.29 to 0.51 km s^{-1}, with a mean value of 0.37 km s^{-1}. The non-thermal contribution is about 2.5 times larger than the thermal line width, suggesting that the protostellar cores in our sample are not purely thermally supported. We find that line widths are roughly constant within the interiors of the cores and larger line widths only occur at the edges of the cores. We conclude that turbulence is not negligible but subsonic in the protostellar cores.

(3) We derive the N_2H^+ velocity fields of eight Class 0 protostellar cores. CB 230 and RNO 43 show symmetrical velocity gradients that can be explained by bulk rotation. In L723 VLA2, IRAS 03282, and IRAS 04166, outflow-envelope interaction appears to dominate the velocity fields. CB 68, CB 224, and CB 244 show complicated velocity fields, which could be affected by infall or large-scale turbulence. We argue that in these cores the observed velocity gradients provide an upper limit to any underlying bulk rotation.

(4) The velocity gradients over the cores range from 6 to 24 km s^{-1} pc^{-1}, with a mean value of $\sim$ 7 km s^{-1} pc^{-1}. This is much larger than what has been found in single-dish observations of prestellar cores, but agrees with recent interferometric observations of other Class 0 protostellar cores. Assuming these gradients are due to rotation, the comparison between gradients and core sizes suggests that smaller (evolved) protostellar cores rotate much faster than larger dense (prestellar) cores. The data could be fitted by a relation of $g \propto R^{-0.6\pm0.1}$.

(5) We find that in terms of specific angular momentum and size scale Class 0 protostellar cores fill the gap between dense molecular cloud cores and PMS binary systems. There appears to be no evolution (decrease) of angular momentum from the smallest prestellar cores via protostellar cores to wide PMS binary system. In the context that most protostellar cores are assumed to fragment and form binary stars, this means that most of the angular momentum contained in the collapse region is transformed into orbital angular momentum of the resulting stellar binary system.

(6) Both thermal and turbulent energy together dominate the support against gravity, but the thermal contribution is about 2 times larger than turbulence. All protostellar cores in our sample are found to be slightly virially supercritical.

(7) The ratio $\beta_{\rm rot}$ of rotational energy to gravitational energy is relatively small in our sample, ranging from 0.004 to 0.02, with a mean value of 0.007. We find that $\beta_{\rm rot}$ values in our sample show no clear correlation with observed binary protostars. On the other hand, the three identified binary protostars are also not distinguished by $\beta_{\rm turb}$ values. This could be due to low-number statistics combined with observational uncertainties.

Chapter 3

ATCA and Spitzer observations of two southern binary protostars

This chapter is based on a paper submitted to Astrophysics Journal by Chen, Launhardt, Bourke, Henning, & Barnes (2007).

Abstract

We present interferometric observations of the isolated, low-mass protostellar double cores CG 30 and BHR 71 in the N_2H^+ (1–0) line and at 3 mm dust continuum, using the Australian Telescope Compact Array (ATCA). The results are complemented by infrared data from the *Spitzer Space Telescope*. In CG 30, the 3 mm dust continuum images resolve two compact sources with a separation of 21″. In BHR 71, strong dust continuum emission is detected at the position of the mid-infrared source IRS1, while only weak emission is detected from the secondary mid-infrared source IRS2. Assuming standard gas to dust ratio and optically thin 3 mm dust continuum emission, we derive hydrogen gas masses of $0.05 - 2.1\,M_\odot$ for the four sub-cores. N_2H^+ (1–0) line emission is detected in both CG 30 and BHR 71, and is spatially associated with the thermal dust continuum emission. By simultaneously fitting the seven hyperfine line components of N_2H^+, we derive the velocity fields and find symmetric velocity gradients in both sources. Assuming that these gradients are due to core rotation, we estimate the specific angular momenta and the energy balance for all cores. Estimated virial masses of the sub-cores range from $0.3 - 0.9\,M_\odot$. We also find that the N_2H^+ emission is strongly affected by the outflows, both in terms of entrainment and molecule destruction. *Spitzer* images show the mid-infrared emission from all four sub-cores, which is spatially associated with the 3 mm dust continuum emission. All four sources appear to drive their own outflows, as seen in the shock-excited 4.5 μm images. Based on the ATCA and *Spitzer* observations, we construct spectral energy distributions (SEDs) and derive temperatures and luminosities for all cores. The analysis of the SEDs suggests an evolutionary discrepancy between the two sub-cores in both CG 30 and BHR 71. We speculate that the sources may still be coeval but that the evolutionary discrepancy is due to unequal masses and hence evolutionary speeds. Based on the morphology and velocity structure, we suggest that the sub-cores in CG 30 were formed by the initial

fragmentation of a filamentary prestellar core, while those in BHR 71 could originate from rotational fragmentation of a single collapsing protostellar core.

3.1 Introduction

In this chapter I present ATCA observations of two southern protobinaries in the N_2H^+ (1–0) molecular line and at 3 mm dust continuum, together with complementary mid-infrared (MIR) data from the *Spitzer Space Telescope* (hereafter *Spitzer*).

CG 30 (also known as BHR 12 or DC 253.3−1.6) is a bright-rimmed cometary globule located in the Gum Nebula region. The distance towards CG 30 is somewhat uncertain, with estimates ranging from 200 pc (Knude et al. 1999) to 400 pc (Brandt 1971; Reipurth 1983). For consistency with earlier papers (e.g., Henning & Launhardt 1998), we use here 400 pc. The globule harbors an elongated protostellar core as seen in the single-dish mm dust continuum image. Higher resolution submm continuum observations (SCUBA) resolve the source into two sub-cores with a projected separation of $\sim 20''$ and masses of 0.17 ± 0.05 and 0.14 ± 0.05 $M_\odot$ for the northern and southern sub-cores, respectively (Henning et al. 2001). The northern core is associated with a near-infrared (NIR) source, which drives the Herbig-Haro flow HH 120 (see Hodapp & Ladd 1995 and references therein). The newly discovered southern core is the origin of a protostellar jet with position angle (P.A.) 44° (Hodapp & Ladd 1995), but no NIR source is seen at this position (see Launhardt et al. 2001).

BHR 71 (also known as DC 297.7−2.8) is an isolated Bok globule located at a distance of $\sim$ 200 pc (Bourke et al. 1997; hereafter B97). A highly-collimated bipolar outflow, which is lying almost in the plane of the sky, was discovered by CO observations in this region. The driving source is associated with IRAS 11590−6452 and was classified as a Class 0 protostar with a total luminosity of $\sim 9\,L_\odot$ (B97). ISOCAM observations have revealed that the IRAS source is associated with two embedded protostars, IRS1 and IRS2, with a projected separation of $\sim 17''$ (Bourke 2001; hereafter B01). IRS1 and IRS2 each drive a CO outflow: the well-known large-scale collimated bipolar outflow is driven by IRS1 and another fainter and smaller bipolar outflow is driven by IRS2 (see B01 and Parise et al. 2006). Only IRS1 appears to be associated with a substantial amount of circumstellar material (B01).

3.2 Observations and data reduction

3.2.1 ATCA observations

Millimeter interferometric observations at 95 GHz of CG 30 and BHR 71 were carried out using ATCA with five 22 m telescopes in May and August 2005. Observations were obtained in two different array configurations (H168 and H75) with projected baselines ranging from 6 to 60 kλ. All antennas were equipped with cooled SIS receivers, which provided average system temperatures of $200 - 350$ K at the observing frequency. A digital correlator was used with 2 independent spectral windows. The narrow window (bandwidth $\sim$ 8 MHz), with a channel width of 0.019 MHz, was centered on the

Table 3.1: Target list and summary of observations

Object Name	Other Name	IRAS Source	R.A. & Dec. (J2000)[a] [h : m : s, ° : ′ : ″]	Distance [pc]	Array configuration	HPBW[b] [arcsecs]	rms[c] [mJy/beam]
CG 30	BHR 12	08076−3556	08:09:33.0, −36:05:01.00	400	H75+H168	4.6×3.3/4.6×3.2	65/0.5
BHR 71	B 213	11590−6452	12:01:36.5, −65:08:49.49	200	H75+H168	3.6×2.9/3.9×3.1	20/2.0

[a]Reference position for figures and tables in this chapter (except *Spitzer* images).
[b]Synthesized FWHM beam sizes at N_2H^+(1-0) line / 3 mm dust continuum with robust weighting 1.
[c]1 σ noises at N_2H^+(1-0) line / 3 mm dust continuum.

Table 3.2: ATCA 3 mm dust continuum results for CG 30 and BHR 71.

Source	R.A.[a] (J2000)	Dec.[a] (J2000)	S_ν [mJy]	FWHM sizes[a] maj.×min.	FWHM sizes[a] P.A.	M_H [$M_\odot$]	$\langle n_H \rangle$[b] [$\times 10^7 cm^{-3}$]	N_H[c] [$\times 10^{23} cm^{-2}$]
CG 30N	08:09:33.12	−36:04:58.12	15.8±3.2	5.″1×3.″1	89±7°	1.10±0.26	1.11	4.51
CG 30S	08:09:32.67	−36:05:19.09	6.0±1.3	4.″8×3.″1	74±15°	0.33±0.10	0.37	1.45
BHR 71 IRS1	12:01:36.81	−65:08:49.22	140±28	7.″8×7.″1	−73±20°	2.12±0.41	2.64	9.94
BHR 71 IRS2	12:01:34.09	−65:08:47.36	2.8±2.1	2.″6×2.″1	76±40°	0.05±0.02	2.18	2.58

[a]Center position and FWHM sizes of the continuum sources derived from gaussian uv plane fitting.
[b]Assuming a spherical morphology for the objects, the mean volume density of hydrogen atoms $n_H = n(H) + 2n(H_2)$ was calculated by $n_H = M_H/m_H V$, with $V \sim \pi/6(\theta_S D)^3$ being the Volume of the sources.
[c]The hydrogen column density $N_H = N(H) + 2\,N(H_2)$ was derived from the flux densities by $N_H = \frac{S_\nu}{\kappa_d(\nu)\,\Omega_S\,B_\nu(\nu,T_d)}\,\frac{1}{m_H}\left(\frac{M_H}{M_d}\right)$, where Ω_S is the solid angle of the objects and m_H is the proton mass.

N_2H^+ (1-0) line at 93.17 GHz, adopting the systemic velocity of two sources during the observations. The broad window (bandwidth $\sim$ 128 MHz) was centered at 95.0 GHz and was used to measure the 3.1 mm dust continuum emission simultaneously with N_2H^+. The two sources were observed with 2-point mosaics each. The primary beam size at 93 GHz is $\sim 38''$. Amplitude and phase were calibrated through frequent observations of quasars nearby to each source (0745−330 for CG 30 and 1057−797 for BHR 71), typically every 20 minutes, resulting in an absolute position uncertainty of $\leq 0\farcs2$. Flux densities were calibrated using the secondary calibrator 1253−055, the flux of which was regularly compared to Uranus and adopted as 19.0 Jy for May observations (H168 configuration) and 14.7 Jy for August observations (H75 configuration). Additional effort was made to improve the gain-elevation calibration of the antennas, which can significantly affect the flux density scale, especially when observing at high elevation. The estimated total flux uncertainty is $< 20\%$. Observing parameters are summarized in Table 3.1.

The data were calibrated and images produced using MIRIAD (Sault et al. 1995) and its CLEAN algorithm, with "robust" *uv* weighting parameter +1 (Briggs et al. 1999). Synthesized beam sizes are $3'' - 4''$. Noise levels ($1\,\sigma$ rms) in the final maps are $0.5 - 2$ mJy/beam for the continuum and $20 - 65$ mJy/beam for the N_2H^+ line (see Table 3.1). Further analysis and figures were done with the GILDAS software package.

3.2.2 Spitzer observations

Mid-infrared data of CG 30 and BHR 71 were obtained from the *Spitzer* Science Center[1]. CG 30 was observed on 2004 April 9 with the Multiband Imaging Photometer for *Spitzer* (MIPS: AOR key 9426688) and May 26 with the Infrared Array Camera (IRAC; AOR key 5097216). BHR 71 was observed on 2004 June 10 with IRAC (AOR key 5107200) and 2005 March 7 with MIPS (AOR key 9434112). Both sources were observed as part of the c2d Legacy program (Evans et al. 2003).

The data were processed by the *Spitzer* Science Center using their standard pipeline (version S14.0) to produce Post Basic Calibrated Data (P-BCD) images, which are flux-calibrated into physical units (MJy sr^{-1}). Flux densities in the IRAC bands were measured with aperture photometry in the IRAF APPHOT package, using the radii, sky annuls, and aperture corrections recommended by the *Spitzer* Science Center. The results were compared to c2d, which used PSF fitting, and found to be within the uncertainties. Flux densities in the MIPS bands were measured with GILDAS because sources in the MIPS images are not fully resolved (see § 3.3.3). Further figures were completed with the GILDAS package.

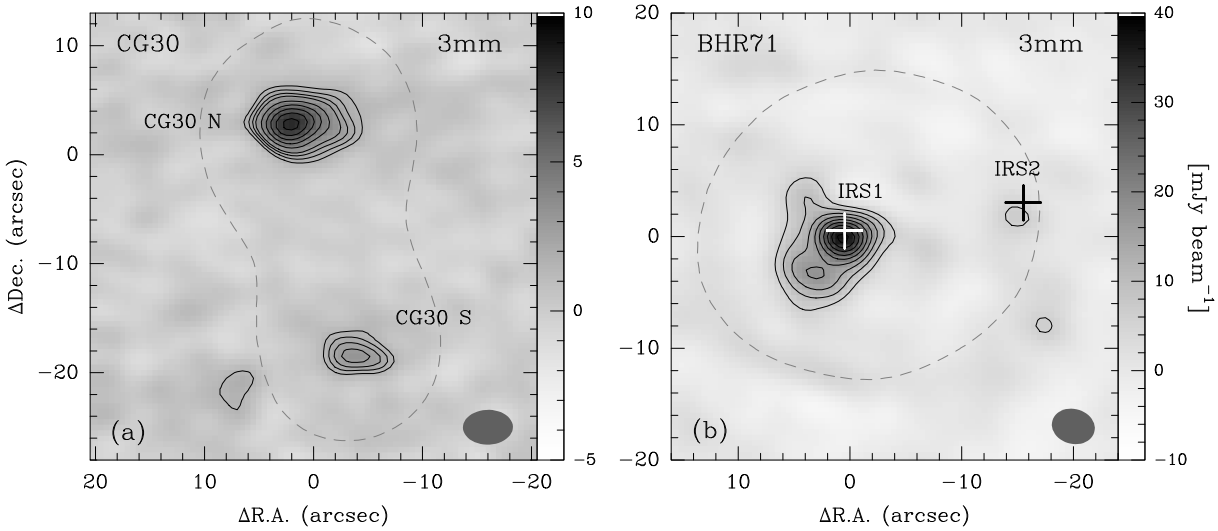

Figure 3.1: (a) 3 mm dust continuum image of CG 30. Contours start at $\sim 3\,\sigma$ (0.5 mJy) with steps of $\sim 2\,\sigma$. The grey dashed contour represents the half-maximum level of the 850 μm emission peak obtained by SCUBA observation (Henning et al. 2001). (b) The same for BHR 71. Contours start at $\sim 3\,\sigma$ (2 mJy) with steps of $\sim 2\,\sigma$. The crosses mark the positions of the *Spitzer* MIR sources. The grey dashed contour represents the half-maximum level of the 1.2 mm emission peak obtained by SEST observation (B97). Synthesized ATCA beams are shown as grey ovals in the two maps.

3.3 Results

3.3.1 Dust continuum

The 3 mm dust continuum image of CG 30 (Fig. 3.1a) shows two compact sources with an angular separation of $21\farcs7 \pm 0\farcs6$, corresponding to a projected linear separation of 8700 ± 240 AU at a distance of 400 pc. Following Henning et al. (2001), we refer the northern source as CG 30N and the southern source as CG 30S. From gaussian *uv* plane fitting, we derive flux densities of 15.8 ± 3.2 mJy[2] for source N and 6.0 ± 1.3 mJy for source S. The large-scale common envelope, detected in the submm single-dish maps with a radius of ~ 14000 AU and a flux density of ~ 7.4 Jy (Henning et al. 2001), is completely resolved out by the interferometer at 3 mm. Both embedded sources are spatially resolved. Source positions and deconvolved FWHM sizes, derived from gaussian *uv* plane fitting, are listed in Table 3.2.

In the 3 mm dust continuum image of BHR 71 (Fig. 3.1b), strong emission is detected at the position of IRS1, and only weak emission ($\sim 3\,\sigma$ level) is detected at the position of IRS2. The flux densities of IRS1 and IRS2 are derived to be 140 ± 28 mJy

[1] http://ssc.spitzer.caltech.edu

[2] The error bar is derived from $\sqrt{\sigma_{\rm cali}^2 + \sigma_{\rm fit}^2}$, where $\sigma_{\rm cali}$ is the uncertainty from calibration ($\sim 20\%$ of flux density) and $\sigma_{\rm fit}$ is the uncertainty from gaussian fitting.

and 2.8 ± 2.1 mJy, respectively. The large-scale envelope detected in the 1.3 mm single-dish map, with a radius of ~ 9000 AU and a flux density of ~ 3.7 Jy (B97), is also resolved out here. Positions and FHWM sizes of the sources are listed in Table 3.2. The angular separation of $17'' \pm 1''$ between IRS1 and IRS2 corresponds to a projected linear separation of 3400 ± 200 AU at a distance of 200 pc. We also note that IRS1 is elongated northwest-southeast and consists of two separate peaks in the region enclosed by the $5\,\sigma$ level (see Fig. 3.1b). The main peak is spatially coincident with the MIR source and the fainter peak is located $\sim 2''$ southeast of IRS1 (see below § 3.3.3).

Assuming that the 3 mm dust continuum emission is optically thin, the hydrogen gas mass $M_{\rm H} = M({\rm H}) + 2\,M({\rm H_2})$ in the circumstellar envelope was calculated by

$$M_{\rm H} = \frac{S_\nu\, D^2}{\kappa_{\rm d}(\nu)\, B_\nu(\nu, T_{\rm d})} \left(\frac{M_{\rm H}}{M_{\rm d}}\right), \tag{3.1}$$

where S_ν is the flux density, $\kappa_{\rm d}(\nu)$ is the dust opacity, $B_\nu(\nu, T_{\rm d})$ the Planck function, $T_{\rm d}$ the mean dust temperature, and $M_{\rm H}/M_{\rm d}$ the hydrogen-to-dust mass ratio. We adopt an interstellar hydrogen-to-dust mass ratio of 110, and a dust opacity $\kappa_{\rm 3mm} \approx 0.2\,{\rm cm^2\,g^{-1}}$ (using $\kappa_{\rm 1.3mm} = 0.8\,{\rm cm^2\,g^{-1}}$ and $\kappa \propto \nu^{1.8}$), a fairly typical value for dense protostellar cores (Ossenkopf & Henning 1994). Dust temperatures are derived from SED fitting (see § 3.4.1) and are listed in Table 3.7. The derived hydrogen masses ($0.05 - 2.1\,M_\odot$), together with mean volume densities ($0.4 - 2.6 \times 10^7\,{\rm cm^{-3}}$) and column densities ($1.5 - 9.9 \times 10^{23}$ cm^{-3}), are listed in Table 3.2. The resulting optical depths are $\tau_{\rm 3mm} \sim 0.4 - 3 \times 10^{-3}$, thus justifying the optically thin approximation.

3.3.2 N_2H^+ (1−0)

N_2H^+ emission is detected from both CG 30 and BHR 71. Figure 3.2a shows the velocity-integrated N_2H^+ intensity image of CG 30. Two cores, spatially associated with the 3 mm dust continuum sources, are seen. The northern core is elongated east-west with a long ($\sim 20''$) extension to the west, along the direction of the protostellar jet HH 120 (see Fig. 3.7c). The southern core is more compact and peaks at the position of the dust continuum source.

Figure 3.2b shows the integrated N_2H^+ intensity image of BHR 71. Two cores are found to the east and west of IRS1 (see below and discussion in § 3.4.4). We refer to these as BHR 71E and BHR 71W, respectively. The two cores are elongated in the north-south direction. Several smaller clumps are also seen north and south of the two main cores, along both sides of the large-scale CO outflow (see Fig. 3.2b). The mean radii of the N_2H^+ cores (Table 3.4) were measured with the same method described in Chapter 2.

Figure 3.3 shows the N_2H^+ spectra at the peak positions of CG 30 and BHR 71[3]. The spectra were fitted using the hyperfine program in CLASS. The fitting results, such as LSR velocities ($V_{\rm LSR}$), intrinsic line width ($\triangle v$; corrected for instrumental effects), total optical depths ($\tau_{\rm tot}$), and excitation temperatures ($T_{\rm ex}$), are listed in Table 3.3.

[3]During the observations towards BHR 71, the correlator was not well centered due to an uncertainty in the Doppler correction calculation, resulting in the N_2H^+ $JF_1F = 101 - 012$ component not being covered. However, the absence of this line component did not affect our final results.

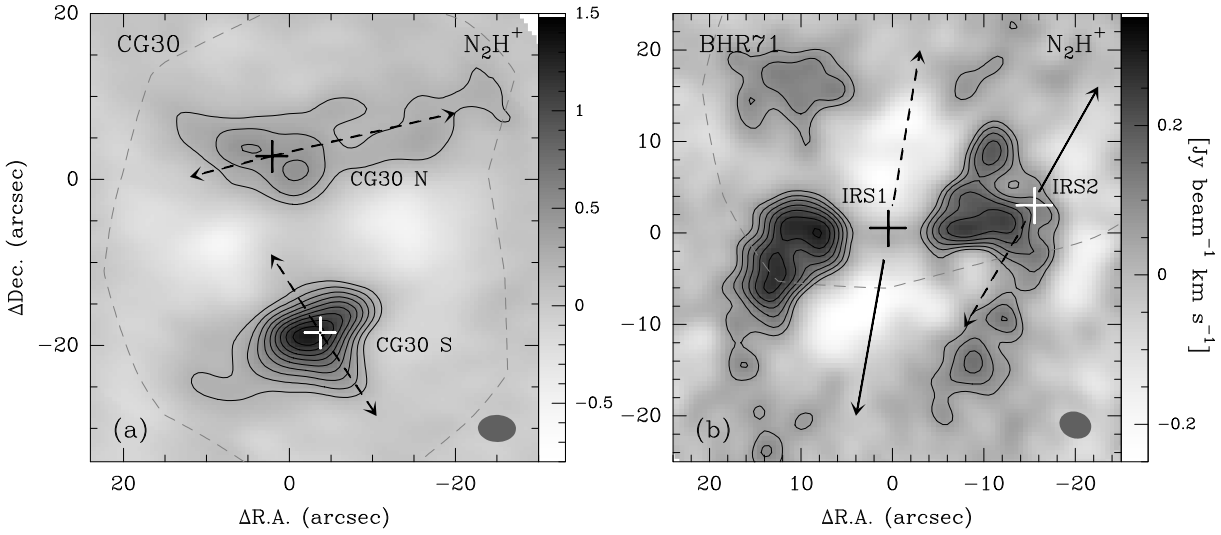

Figure 3.2: (a) Image of the N_2H^+ (1–0) intensity integrated over the seven hyperfine components for CG 30. Contours start at $\sim 3\,\sigma$ (~ 60 mJy) with steps of $\sim 2\,\sigma$. The arrows show the directions of protostellar jets (see § 3.3.3). The grey dashed contours show the half-maximum level of the single-dish Mopra observation. (b) The same for BHR 71. The solid and dashed arrows show the directions of the blue-shifted and red-shifted CO outflows (see § 3.3.3). The crosses in both images represent the peaks of 3 mm dust continuum emission. Synthesized ATCA beams are shown as grey ovals.

Table 3.3: Observing parameters from N_2H^+ (1-0) spectra fitting

	$V_{\rm LSR}{}^a$ [km s^{-1}]	$\triangle v^a$ [km s^{-1}]	$\tau_{\rm tot}{}^a$	$T_{\rm ex}{}^a$ [K]	$\triangle v_{\rm mean}{}^b$ [km s^{-1}]	$\triangle v_{\rm NT}{}^c$ [km s^{-1}]
CG 30 N	6.64±0.02	0.53±0.03	1.0±0.1	4.66±0.09	0.51±0.01	0.47
CG 30 S	6.48±0.01	0.52±0.02	1.4±0.1	6.81±0.05	0.52±0.01	0.48
BHR 71 E	−4.35±0.02	0.44±0.10	1.9±0.4	4.44±0.13	0.28±0.01	0.20
BHR 71 W	−4.42±0.02	0.38±0.06	2.5±0.2	3.91±0.05	0.33±0.01	0.27

[a] Value at the intensity peak. The error represents $1\,\sigma$ error in the hyperfine fitting.
[b] Mean line width obtained through gaussian fitting.
[c] Non-thermal line width at the given dust temperature (see Table 3.7).

Table 3.4: Volume size, density, and mass of N_2H^+

Source	R [AU]	$M_{\rm vir}$ [$M_\odot$]	$n_{\rm vir}$ [$\times 10^6$ cm^{-3}]	$N(N_2H^+)$ [$\times 10^{12}$ cm^{-2}]	$M_{N_2H^+}$ [$\times 10^{-10}$ $M_\odot$]	$X(N_2H^+)$ [$\times 10^{-10}$]
CG 30 N	1300	0.63	10.4	1.29	0.51	1.10
CG 30 S	1650	0.91	7.4	3.42	1.94	2.91
BHR 71 E	960	0.21	8.9	1.95	0.34	2.18
BHR 71 W	730	0.18	17.2	1.87	0.21	1.51
BHR 71 IRS1[a]	3000	0.80	1.1	1.90	3.07	5.13

[a] Assuming that the two N_2H^+ cores found in BHR 71 are part of a physical structure around IRS1 with a radius of ~ 3000 AU (see Fig. 3.2b) and a mean line width of 0.33 km s^{-1} (see Table 3.3).

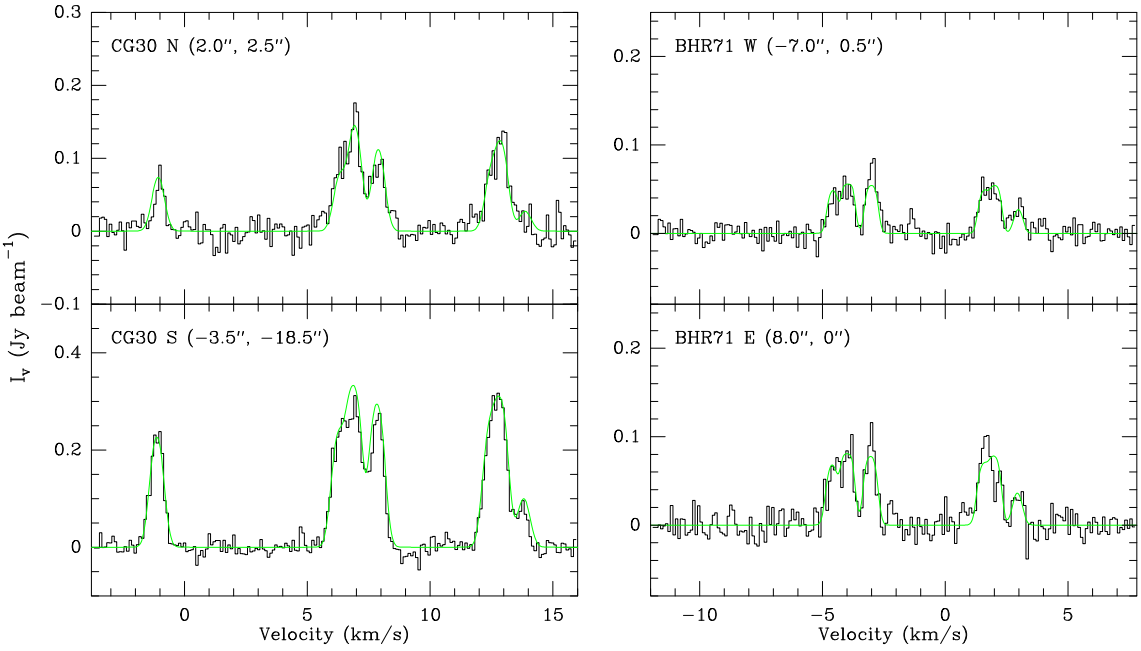

Figure 3.3: N_2H^+ spectra at the peak positions of the two cores in CG 30 (left) and BHR 71 (right). Green curves show the results of hyperfine structure line fitting. Fit parameters are given in Table 3.3.

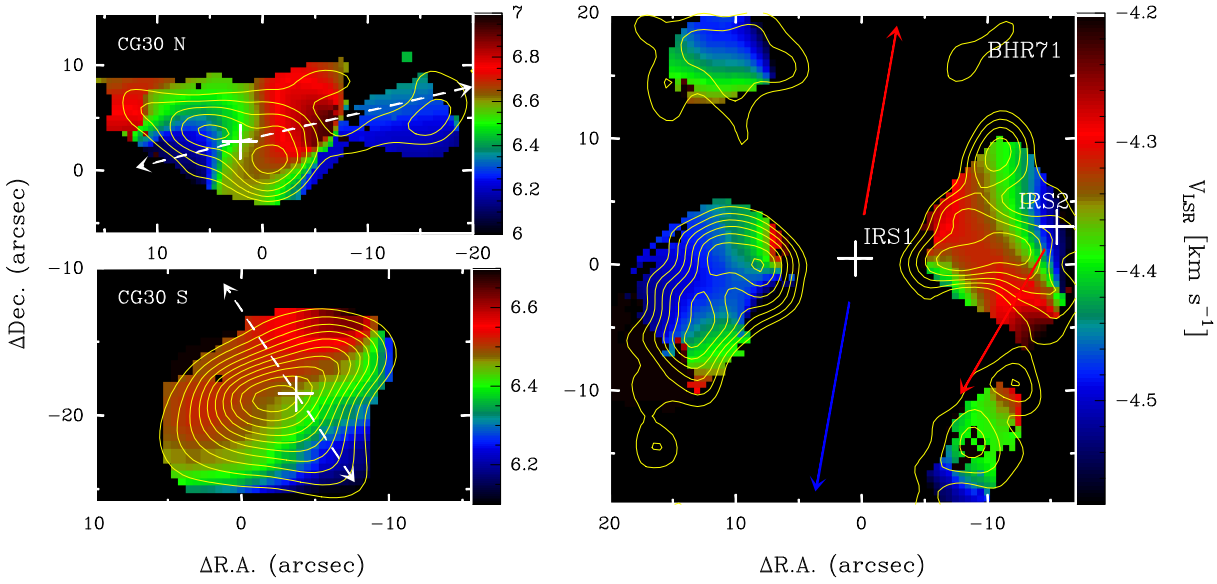

Figure 3.4: N_2H^+ velocity field maps of CG 30 (left) and BHR 71 (right). Contours are same as in Fig. 3.2. The white arrows in CG 30N and CG 30S show the directions of protostellar jets. The red and blue arrows in the BHR 71 map show the directions of CO outflows.

Table 3.5: Velocity gradients and specific angular momentum

Source	mean velocity [km s^{-1}]	g [km s^{-1} pc^{-1}]	Θ_g^a [degree]	g_r [km s^{-1}]	J/M [$\times 10^{-3}$ km s^{-1} pc]
CG 30 N	6.62	$<$24.4$\pm$0.2	$-$79.7$\pm$0.4	0.32	$<$ 0.26
CG 30 S	6.45	$<$17.8$\pm$0.2	33.9$\pm$0.3	0.29	$<$ 0.30
BHR 71 IRS1^b	$-$4.39	$\sim$13.0$\pm$0.4	$-$159.8$\pm$1.0	0.39	$\sim$ 0.73

^{a}East of north in the direction of increasing velocity
^{b}The same assumption as in Table 3.4.

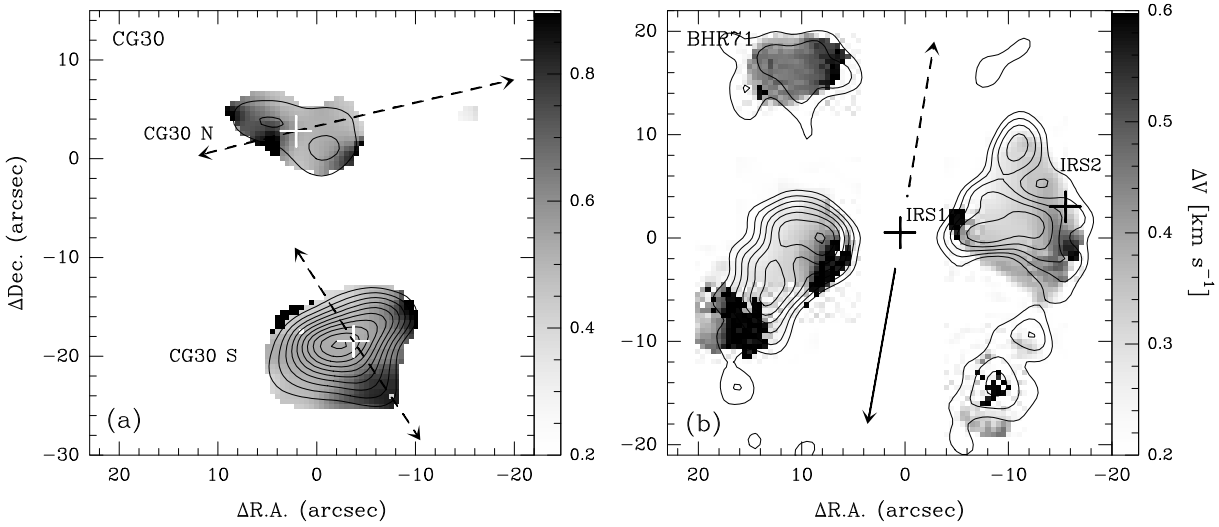

Figure 3.5: Spatial distribution of N_2H^+ line widths in CG 30 (left) and BHR 71 (right), as derived from the HFS line fitting. Contours and symbols are the same as them in Fig. 3.2.

Figure 3.4 shows the mean velocity fields of CG 30 and BHR 71, derived from the N_2H^+ line maps with the fitting routine described in Chapter 2. The jet/outflow information is also shown in each map. Both CG 30N and CG 30S show well-ordered velocity fields, with gradients parallel to the outflow directions. In BHR 71, there is a systematic velocity gradient across the two N_2H^+ cores, which is roughly perpendicular to the axis of the large-scale CO outflow. This may indicate that the two cores are actually part of one physical structure associated with IRS1 (see discussion in § 3.4.4). A least-squares fitting of the velocity gradients has been performed using the routine described in Goodman et al. (1993). The results are summarized in Table 3.5 and discussed in § 3.4.2.

Figure 3.5 shows the spatial distribution of N_2H^+ line widths for both sources. The line widths are roughly constant within the interiors of the cores, which is consistent with the observational results in Chapter 2. The mean line widths were derived through Gaussian fitting to the distribution of line widths versus solid angle area in the maps (see Fig. 3.6). We find that the sub-cores in each object have roughly equal line width,

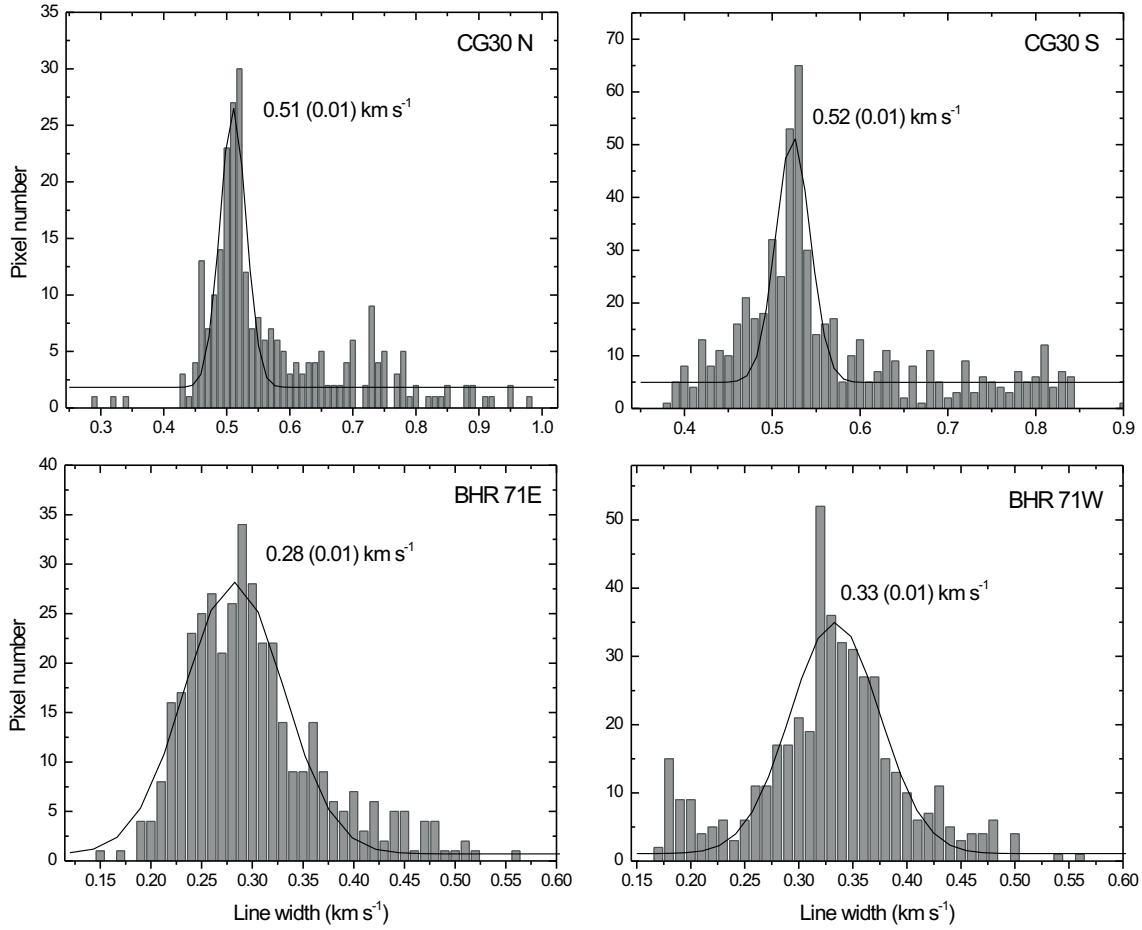

Figure 3.6: Distribution of N_2H^+ line widths versus solid angle areas for CG 30 (top) and BHR 71 (bottom). Black solid curves and numbers show the results of Gaussian fitting to the distributions.

but the mean line width in CG 30 ($\sim 0.5\,\mathrm{km\,s^{-1}}$) is ~ 1.7 times larger than that in BHR 71 ($\sim 0.3\,\mathrm{km\,s^{-1}}$).

Assuming that the observed N_2H^+ line widths are not dominated by systematic gas motions, the virial mass of the cores has been calculated as:

$$M_{\mathrm{vir}} = \frac{5}{8ln2}\frac{R\triangle v_{\mathrm{ave}}^2}{\alpha_{\mathrm{vir}}G}, \tag{3.2}$$

where G is the gravitational constant, R is the FWHM core radius, and $\triangle v_{\mathrm{ave}}$ is the line width of the emission from an "average" particle with mass $m_{\mathrm{ave}} = 2.33$ amu (assuming gas with 90% H_2 and 10% He). The coefficient α_{vir} is a correction for deviations from constant density and adopted as 0.75 here (see Chapter 2). $\triangle v_{\mathrm{ave}}$ is derived from the

observed spectra by

$$\triangle v_{\rm ave}^2 = \triangle v_{\rm obs}^2 + 8ln2\frac{kT_{\rm ex}}{m_{\rm H}}(\frac{1}{m_{\rm ave}} - \frac{1}{m_{\rm obs}}), \tag{3.3}$$

where $\triangle v_{\rm obs}$ is the observed mean line width of N_2H^+ and $m_{\rm obs}$ is the mass of the emitting molecule (here we use $m_{\rm N_2H^+} = 29$ amu). We derive virial masses between 0.2 and 0.9 $M_\odot$. The results are listed in Table 3.4.

The N_2H^+ column density has been calculated independently from the line intensity using the equation given by Benson et al. (1998):

$$N({\rm N_2H^+}) = 3.3 \times 10^{11}\frac{\tau\triangle v T_{\rm ex}}{1 - e^{-4.47/T_{\rm ex}}}\,({\rm cm^{-2}}), \tag{3.4}$$

where τ is the total optical depth, $\triangle v$ is the intrinsic line width in km s^{-1}, and $T_{\rm ex}$ is the excitation temperature in K. The gas-phase N_2H^+ mass of the core was then calculated from $M_{\rm N_2H^+} \approx N({\rm N_2H^+})_{\rm peak} \times m_{\rm N_2H^+} \times d^2 \times \Omega_{\rm FWHM}$, where d is the distance from the Sun and $\Omega_{\rm FWHM}$ is the solid angle enclosed by the FWHM contours for each core.

From the ratio of N_2H^+ gas mass to virial mass, we derived the average fractional abundance of N_2H^+ in each core (see Table 3.4). The average value $\langle X(N_2H^+)\rangle \sim 2.0 \times 10^{-10}$ for CG 30 and BHR 71 is close to the mean value found in Chapter 2 ($\sim 3.3 \times 10^{-10}$) for nine protostellar cores.

3.3.3 Spitzer images

Figure 3.7 shows the *Spitzer* images of CG 30. The infrared emission from CG 30N and CG 30S is detected at all IRAC bands (3.6 μm – 8.0 μm). Fig. 3.7a shows a wide-field IRAC band 2 (4.5 μm) image. Centered at CG 30S is a highly collimated bipolar jet, with P.A. $\sim 40°$. The knots in the jet are labeled with the same numbers as in Hodapp & Ladd (1995). The most distant knot (No. 8) is $\sim 90''$ away from CG 30S. Assuming a typical jet speed of 100 km s^{-1} (Reipurth & Bally 2001), an inclination angle of 90°, and a distance of 400 pc, the dynamical age of the jet is estimated to be $\sim$ 1700 yr. CG 30N appears to be the driving source of HH 120, which is $\sim 5''$ in size and extends to the west. Knot No. 6, located to the east of CG 30N, is probably ejected by CG 30N and part of the same outflow as HH 120.

Figs. 3.7b and 3.7c show enlarged views of the two sources, overlaid with the contours from the ATCA 3 mm dust continuum and N_2H^+ images. The two infrared sources are spatially coincident with the 3 mm dust continuum and N_2H^+ sources. However, when viewed in detail, CG 30S is elongated at the infrared bands and the continuum source is located at the apex of the infrared emission, implying that the infrared emission from CG 30S is due to scattered light in a cavity evacuated by the jet/outflow. In contrast, CG 30N shows a point-like structure at all IRAC bands, implying that the source is directly detected at NIR wavelengths ($\lambda < 5\,\mu$m)[4]. The N_2H^+ emission from CG 30N spatially follows the direction of the protostellar jet and the long extension to the west matches exactly the HH 120 flow (see Fig. 3.7c), indicating that the jet has a strong effect on the morphology of the N_2H^+ emission.

[4]Here we assume that if the NIR emission is point-like and spatially coincides with the circumstellar mm dust emission, it traces the source directly.

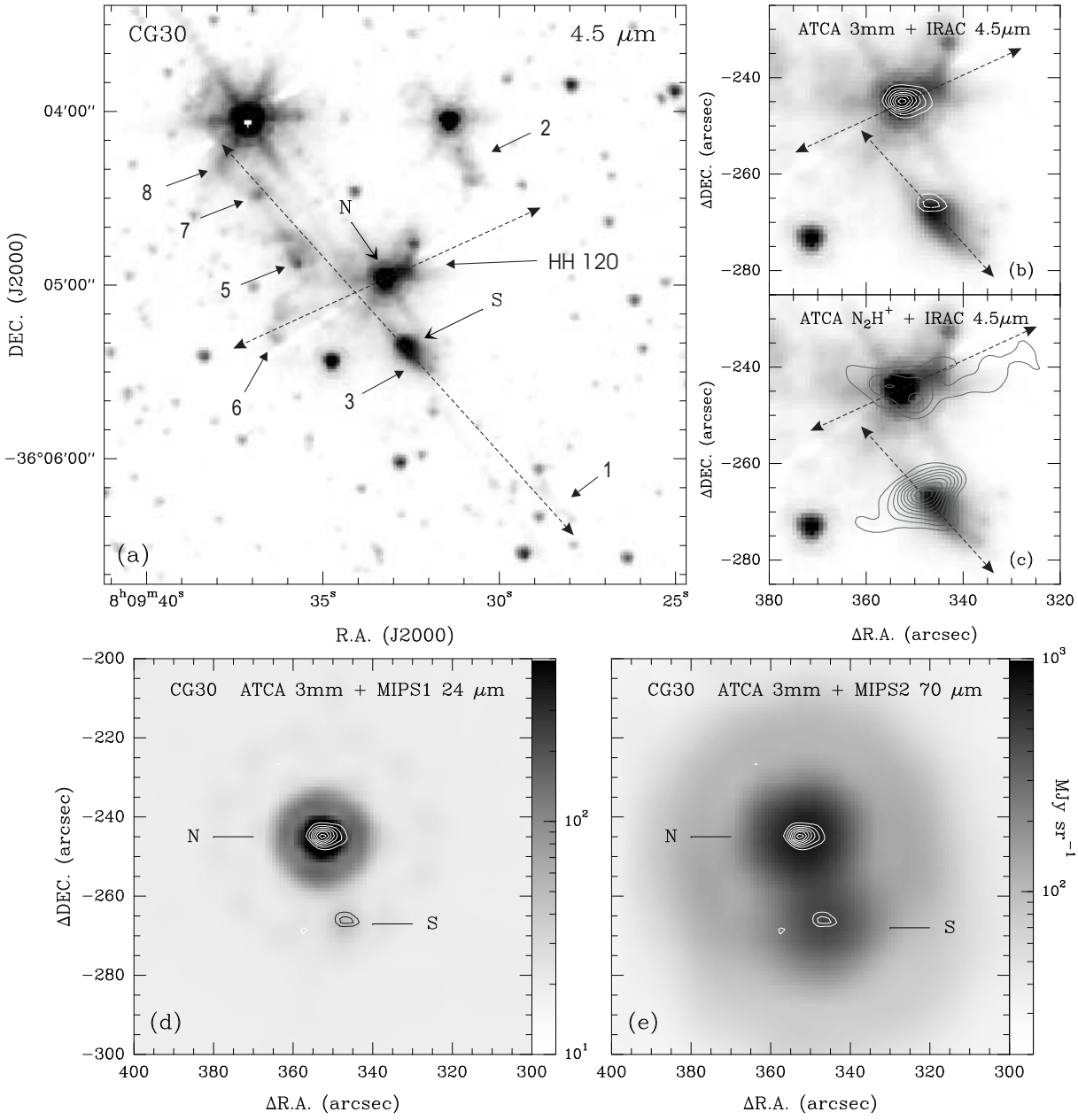

Figure 3.7: *Spitzer* images of CG 30. (a) *Spitzer* IRAC band 2 (4.5 μm) image of CG 30. Sources CG 30N and CG 30S are labeled as "N" and "S", respectively. Dashed arrows show the directions of the protostellar jets; (b) IRAC band 2 image overlaid with the ATCA 3 mm dust continuum contours (reference center at R.A.=08:09:04.082, DEC=−36:00:53.53, J2000); (c) Same, but overlaid with the ATCA N_2H^+ intensity contours; (d) *Spitzer* MIPS 1 (24 μm) image of CG 30, overlaid with the ATCA 3 mm dust continuum contours; (e) *Spitzer* MIPS 2 (70 μm) image of CG 30, overlaid with the ATCA 3 mm dust continuum contours.

Table 3.6: *Spitzer* flux densities of CG 30 and BHR 71[a].

Source	R.A.[b] (J2000)	Dec.[b] (J2000)	$S(3.6\,\mu m)$ [mJy]	$S(4.5\,\mu m)$ [mJy]	$S(5.8\,\mu m)$ [mJy]	$S(8.0\,\mu m)$ [mJy]	$S(24\,\mu m)$ [mJy]	$S(70\,\mu m)$ [mJy]
CG 30N	08:09:33.20	−36:04:58.17	55.7±1.4	123.4±2.1	256.1±3.0	395.8±3.8	3400±100	8700±430
CG 30S	08:09:32.68	−36:05:20.38	6.7±0.5	16.8±0.8	19.6±0.8	9.6±0.6	50±5	4200±340
BHR 71 IRS1	12:01:36.57	−65:08:49.52	32.4±1.1	82.4±1.7	123.3±2.1	210.2±2.8	5000±300	84000±800
BHR 71 IRS2	12:01:34.05	−65:08:47.03	4.5±0.4	12.4±0.7	15.4±0.7	9.3±0.6	90±30	−−

[a]Flux densities in the IRAC and MIPS bands were measured using IRAF APPHOT and GILDAS, respectively (see § 3.2.2).
[b]Peak position of infrared sources measured at the IRAC band 3 (5.8 μm).

Table 3.7: Fitting results of the spectral energy distribution

Source	$T_{\rm dust}$ [K]	$T_{\rm bol}$ [K]	$L_{\rm bol}$ [$L_\odot$]	$L_{\rm submm}$ [$L_\odot$]	$L_{\rm submm}/L_{\rm bol}$ [%]	Classification
CG 30N	22	102	13.6±0.8	0.49±0.10	3.6	Class I
CG 30S	27	37	4.3±0.5	0.32±0.05	7.4	Class 0
BHR 71 IRS1	25	44	13.5±1.0	0.49±0.05	3.6	Class 0/I
BHR 71 IRS2	20	56	0.5±0.1	0.02±0.01	2.2	Class 0

In the *Spitzer* MIPS 1 (24 μm) image shown in Fig. 3.7d, CG 30 is again resolved in two sources, but the emission is dominated by CG 30N and only weak emission is found at the position of CG 30S. In the MIPS 2 (70 μm) image (see Fig. 3.7e), the two sources are not fully resolved, but two peaks, with total flux ratio $\sim$ 2:1, can be clearly distinguished. Flux densities of CG 30N and CG 30S in the IRAC and MIPS bands are measured (see § 3.2.2) and listed in Table 3.6.

The *Spitzer* images of BHR 71 are shown in Figure 3.8, with the same sequence as in Fig. 3.7. The infrared emission from IRS1 and IRS2 is detected at all IRAC bands. A large-scale ($\sim$ 160″ in length) bipolar jet, centered at IRS1 with a P.A. of 165°, is seen in the IRAC images (Fig. 3.8a). The northern jet, spatially coincident with the red-shifted CO outflow, is S-shaped, while the southern jet, containing the HH object HH 321 (Corporon & Reipurth 1997), shows a V-shaped structure at the apex. This V-shaped structure may represent a conical cavity evacuated by the successive bow-shocks traced by the infrared emission (Fig. 3.8a) and the blue-shifted CO outflow (see B97 and Parise et al. 2006). Another bipolar jet, at P.A. $\sim$ 30°, is found with IRS2 being in the center. Its northwest lobe, containing another HH object HH 320 (Corporon & Reipurth 1997), also shows a V-shaped structure at the apex and could be explained in the same way.

IRS1 and IRS2 are spatially coincident with the dust continuum sources detected with ATCA (see Fig. 3.8b). The elongated structure and secondary peak found in the ATCA dust continuum image match the left wall of the outflow cavity, suggesting they result from the jet/outflow action (for a similar case, see Gueth et al. 2003). The N_2H^+ emission is located on both sides of the large-scale CO outflow and basically matches the wall of the cavity (see Fig. 3.8c). At the MIPS 1 band, BHR 71 is barely resolved into two sources and the emission is dominated by IRS1 (see Fig. 3.8d). The MIPS 2 image does not resolve the two sources and the emission is peaked at the position of IRS1 (see Fig. 3.8e). Flux densities of IRS1 and IRS2 are listed in Table 3.6.

3.4 Discussion

3.4.1 Spectral energy distributions and evolutionary stages

Figure 3.9 shows the spectral energy distributions (SEDs) of CG 30 N and S and BHR 71 IRS1 and IRS2, based on the infrared (ISOCAM, *Spitzer*, and IRAS), sub-mm (SCUBA, available only for CG 30), and mm (SEST and ATCA) observations. The NIR data of CG 30N are adopted from Persi et al. (1990). The SCUBA and SEST data for CG 30 are adopted from Henning et al. (2001) and Henning & Launhardt (1998), respectively. The ISOCAM and SEST data for BHR 71 are adopted from B01 and B97, respectively. Here we do not explicitly list all flux values, but show graphically the SEDs. Since IRAS observations could resolve neither CG 30 nor BHR 71, flux ratios at the IRAS wavelengths of 10:1 (CG 30N : CG 30S) and 20:1 (BHR 71 IRS1 : IRS2) were inferred from the *Spitzer* and ATCA observations. The ATCA measurements, which are not sensitive to extended emission, are indicated by up-arrows as lower limits in each map.

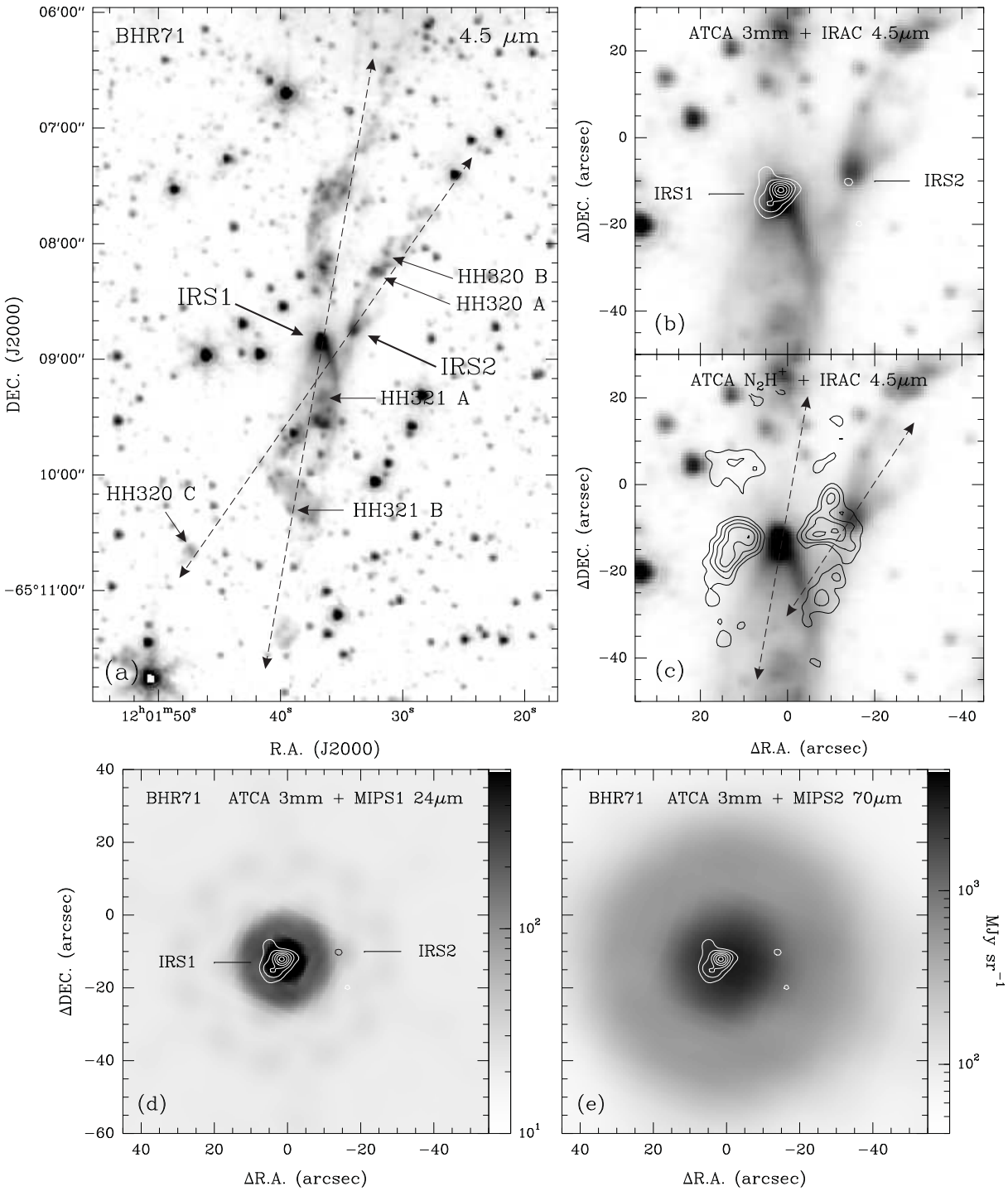

Figure 3.8: The same as Fig. 3.7, but for BHR 71 (reference center at R.A.=12:01:36.349, DEC=−65:08:37.50, J2000).

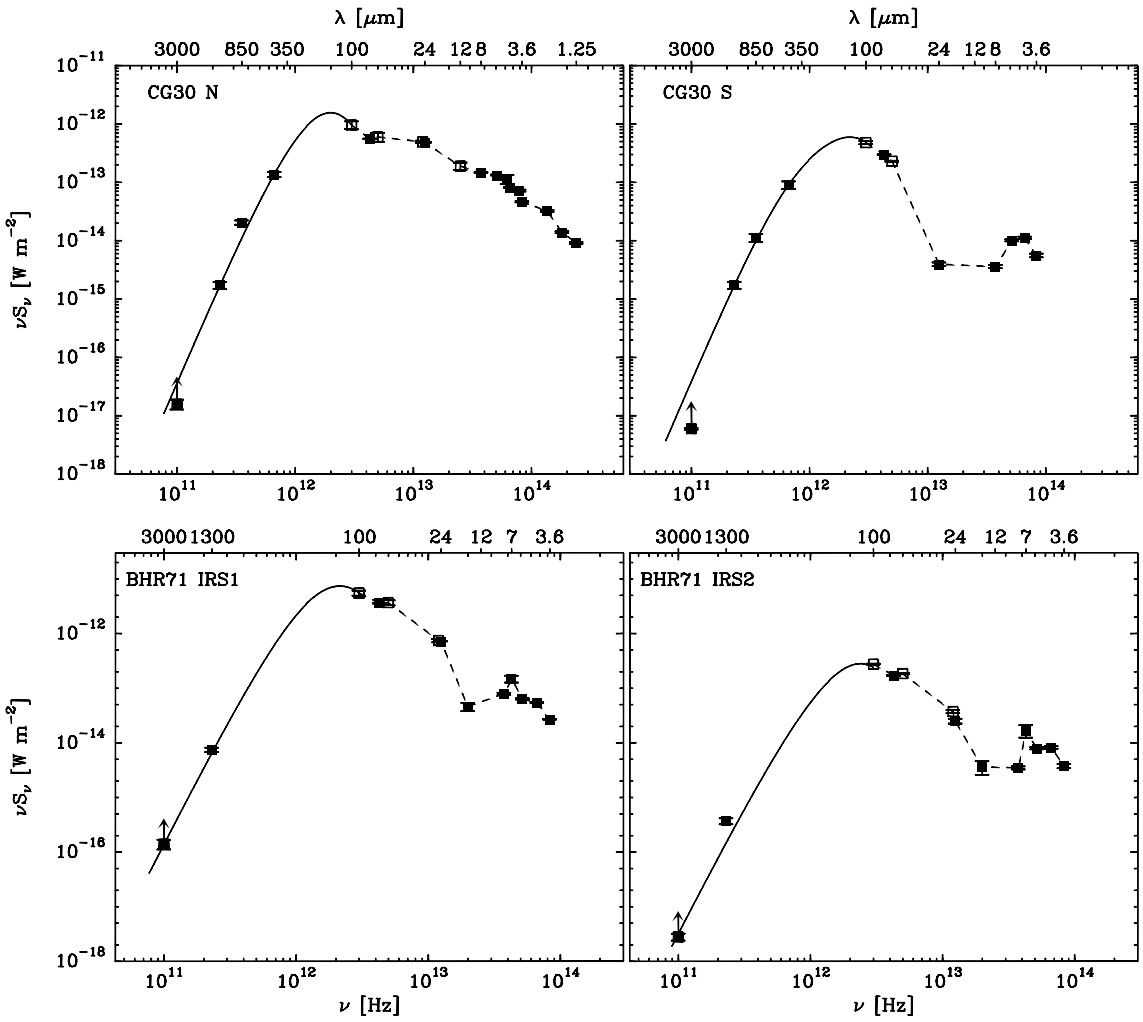

Figure 3.9: Spectral energy distribution of CG 30N (up left), CG 30S (up right), BHR 71 IRS1 (bottom left), and BHR 71 IRS2 (bottom right). Error bars ($1\,\sigma$) are indicated for all data points, but are mostly smaller than the symbol sizes. Open squares represent IRAS data points, where flux densities are divided into two sub-cores with ratios assumed in § 3.4.1. While most data points represent total fluxes, the 3 mm fluxes were measured from interferometric maps which resolved out the envelope and thus represent lower limits only. Solid lines show the best-fit for all points at $\lambda \geq 100\,\mu$m using a grey-body model. Dashed lines at $\lambda \leq 100\,\mu$m show the simple logarithmic interpolation used to derive the luminosity. The fitting results are summarized in Table 3.7.

In order to derive luminosities and bolometric temperatures, we first interpolated and then integrated the SEDs, always assuming spherical symmetry. Interpolation between the flux densities was done by a χ^2 grey-body fit to all points at $\lambda \geq 100\,\mu$m[5], using

$$S_\nu = B_\nu(T_\mathrm{d})(1 - e^{-\tau_\nu})\Omega, \tag{3.5}$$

where $B_\nu(T_\mathrm{d})$ is the Planck function at frequency ν and dust temperature T_d, τ_ν is the dust optical depth as a function of frequency $\tau \propto \nu^{1.8}$, and Ω is the solid angle of the source. A simple logarithmic interpolation was performed between all points at $\lambda \leq 100\,\mu$m. The fitting results, such as dust and bolometric temperatures, sub-mm ($\lambda \geq 350\,\mu$m) and bolometric luminosities, are listed in Table 3.7.

Based on these results, we try to address the evolutionary stages of CG 30 and BHR 71. A detailed definition and discussion for early stellar evolutionary phases can be found in André et al. (2000) and Froebrich (2005). The $L_\mathrm{submm}/L_\mathrm{bol}$ ratios of all sources are $\gg 0.5\%$ (the standard boundary of Class 0 protostars, see André et al. 2000) and the four sources each drive a bipolar jet (see § 3.3.3). However, the bolometric temperature of CG 30N is ~ 100 K and the object is also directly detected at NIR wavelengths, suggesting CG 30N is a Class I young stellar object. In contrast, the low bolometric temperature (37 K) of CG 30S suggests it is a Class 0 protostar. In BHR 71, both IRS1 and IRS2 have bolometric temperatures less than 70 K (see Table 3.7). Nevertheless, IRS1 is directly detected at NIR wavelengths (see Fig. 3.8a), suggesting that it is a transition object between Class 0 and I, while IRS2 could be a Class 0 protostar.

It should be noted that the analysis above does not take into account inclination effects: considering a protostar embedded in a circumstellar disk/envelope, its infrared emission could be detected through the outflow cavity when this system is face-on, but is not seen when it is edge-on. In BHR 71, the bipolar CO outflow powered by IRS1 is lying roughly in the plane of sky, implying the latter case; the bipolar outflow driven by IRS2 appears to favor the same situation (see Parise et al. 2006). In CG 30, however, the inclination effects could not be easily distinguished (especially for CG 30N) because the information about molecular outflows is still missing.

A possible explanation for the evolutionary discrepancy between the two sub-cores in both CG 30 and BHR 71 could be that the two sub-cores are indeed not coeval, which would be inconsistent with the assumption that they are physical binaries. On the other hand, the unequal masses, which implies unequal accretion rates, will result in unequal evolutionary speeds, i.e., the higher-mass component (i.e., source N in CG 30 and IRS1 in BHR 71) will evolve faster. Thus, another explanation for this evolutionary discrepancy could be that the two components are formed coevally in a binary system (see discussion in § 3.4.3), but evolve at different evolutionary rates. We also speculate that this evolutionary discrepancy might be slowly smoothed during the long accretion phase and will probably no longer be evident after both objects evolve into pre-main sequence stars (see Bate 2000).

[5]The 3 mm points were ignored in the fitting to CG 30 to give higher priority to the submm data, resulting in much better fitting.

3.4.2 Gas kinematics

Assuming that at the high densities of $> 10^6\,\mathrm{cm}^{-3}$ (see Table 3.2) the kinetic gas temperature is equal to the dust temperature derived in § 3.4.1, the thermal contribution to the N_2H^+ line width is calculated by $\triangle v_{\rm th}^2 = 8ln2\frac{kT_{\rm K}}{m_{\rm obs}}$, where k is the Boltzmann constant and $m_{\rm obs}$ is the mass of the observed molecule. The non-thermal contributions to the line widths ($\triangle v_{\rm NT} = \sqrt{\triangle v_{\rm mean}^2 - \triangle v_{\rm th}^2}$) were then calculated to be $\sim 0.5\,\mathrm{km\,s}^{-1}$ in CG 30 and $\sim 0.2\,\mathrm{km\,s}^{-1}$ in BHR 71 (see Table 3.3). Compared to the thermal line widths ($\sim 0.2\,\mathrm{km\,s}^{-1}$), these large non-thermal line widths (especially for CG 30) suggest that turbulence, the main contribution to the non-thermal line width (Goodman et al. 1998), plays a significant role in the protostellar cores. It should also be noted that the mean line widths derived for BHR 71 ($\sim 0.3\,\mathrm{km\,s}^{-1}$) are three times smaller than measured by single-dish observations in Mardones et al. (1997; $\sim 0.9\,\mathrm{km\,s}^{-1}$). Taking into account the systematic velocity gradient across the core ($\sim 0.3\,\mathrm{km\,s}^{-1}$; see Table 3.5), the combined line width in our maps is still smaller than the result from single-dish observations. It means that high-level (supersonic) turbulence occurs mainly in the extended envelope which is resolved out by the interferometer, but the inner core is much more "quiet". This is consistent with what we found in Chapter 2, namely that non-thermal motions are quickly damped from large-scale to smaller inner cores (see e.g., Fuller & Myers 1992).

The velocity fields of CG 30N, CG 30S, and BHR 71 show systematic velocity gradients (see Fig. 3.4). As discussed in Chapter 2, systematic velocity gradients are usually dominated by either rotation or outflow. In CG 30, the gradients in both cores are parallel to the jets. Although there is no molecular outflow information available yet for CG 30, these gradients are likely the results of outflows and we treat them as upper limits of underlying rotation velocity gradients. In BHR 71, the velocity gradient across two N_2H^+ cores is roughly perpendicular to the axis of the large-scale CO outflow and could be explained by rotation. [Here we assume that the two cores are associated with IRS1 (see § 3.4.4).] The velocity gradients measured in CG 30N, CG 30S, and BHR 71 are < 24.4, < 17.5, and $13.0 \pm 0.5\,\mathrm{km\,s}^{-1}\,\mathrm{pc}^{-1}$, respectively (see Table 3.5). The gradient in BHR 71 is somewhat larger than the rotation gradient derived for other protostellar cores in Chapter 2 ($\sim 7\,\mathrm{km\,s}^{-1}\,\mathrm{pc}^{-1}$) and other Class 0 protostars, e.g., IRAM 04199 ($7\,\mathrm{km\,s}^{-1}\,\mathrm{pc}^{-1}$, Belloche et al. 2002) and NGC 1333 IRAS 4A ($\sim 10\,\mathrm{km\,s}^{-1}\,\mathrm{pc}^{-1}$, Belloche et al. 2006). On the other hand, the upper limits measured in CG 30N and CG 30S are consistent with those in Chapter 2. Assuming that these velocity gradients are due to core rotation, the specific angular momentum J/M of the objects was calculated using the same method described in Chapter 2. The derived J/M for CG 30N, CG 30S, and BHR 71 are < 0.33, < 0.38, and $\sim 0.73 \times 10^{-3}\,\mathrm{km\,s}^{-1}\,\mathrm{pc}$, respectively (see Table 3.5).

Table 3.8 lists the estimated ratios of thermal, turbulent, and rotational energy to the gravitational potential energy (see Chapter 2 for equations). As found in Chapter 2, both thermal and turbulent energy support are about equally important in the cores, while rotational support is negligible. The estimated $\beta_{\rm rot}$ values for CG 30N, CG 30S, and BHR 71 are < 0.016, < 0.012, and ~ 0.043, respectively. When we apply the equilibrium virial theorem $2[E_{\rm therm} + E_{\rm turb} + E_{\rm rot}] + E_{\rm grav} = 0$ (in the absence of magnetic fields), all the cores are slightly supercritical (see Table 3.8).

Table 3.8: Energy balance[a]

Source	$E_{\rm grav}$ $[\times 10^{35} J]$	$\beta_{\rm rot}$	$\beta_{\rm therm}$	$\beta_{\rm turb}$	$\beta_{\rm vir}$
CG 30N	4.03	< 0.016	0.17	0.19	-0.26
CG 30S	6.64	< 0.012	0.15	0.17	-0.36
BHR 71 IRS1[b]	2.89	~ 0.043	0.30	0.10	-0.13

[a]For equations see Chapter 2
[b]The same assumption as in Table 3.4

3.4.3 How did the cores fragment?

Recent numerical simulations and observations support the hypothesis that the fragmentation of molecular cloud cores is the main mechanism for the formation of binary/multiple stellar systems, although the exact *when*, *where*, *why*, and *how* are still under debate (see reviews by Bodenheimer et al. 2000, Tohline 2002, and Goodwin et al. 2007). In this section, we try to examine the origin of the sub-cores in both CG 30 and BHR 71, i.e., whether they formed by initial cloud fragmentation prior to protostellar collapse or by prompt rotational fragmentation of a single core after the initial collapse.

In CG 30, our previous single-dish submm maps have shown a large-scale hourglass-shaped common envelope around the two sub-cores (Henning et al. 2001; see Fig. 3.1a). The separation between the sub-cores is ~ 8700 AU, which is roughly two times the typical Jeans length [$R_{\rm Jeans} = 0.19\,{\rm pc}\,(\frac{T}{10K})^{\frac{1}{2}}\,(\frac{n_{\rm H_2}}{10^4 cm^{-3}})^{-\frac{1}{2}}$; see Stahler & Palla 2004] in prestellar cores (~ 4000 AU at $T = 10$ K and $n_{\rm H_2} = 10^6\,{\rm cm^{-3}}$). The radial velocity difference between the two sub-cores is $\sim 0.16\,{\rm km\,s^{-1}}$ (see Tables 3.3 & 3.4). If we assume that the total binary mass is $1.4\,M_\odot$ (see Table 3.2) and the orbit is perpendicular to the plane of sky, the orbit velocity difference in a bound system with the separation of 8700 AU should be $\sim 0.38\,{\rm km^{-1}\,s^{-1}}$, about two times larger than the observed value. Furthermore, from this observed velocity difference, we estimate the $\beta_{\rm rot}$ of ~ 0.008 for the large-scale cloud core which contains the two sub-cores (radius ~ 8000 AU; see Fig. 3.2a). This $\beta_{\rm rot}$ is less than the typical boundary suggested by a series of numerical simulations (see e.g., Boss 1999 and Machida et al. 2005) for the rotational fragmentation. Based on the morphology and velocity structure, we suggest that the two sub-cores in CG 30 were formed by initial fragmentation of a large-scale filamentary prestellar core.

In BHR 71, the two sub-cores have a separation of ~ 3400 AU (less than the typical Jeans length) and are also surrounded by a large common envelope (Fig. 3.1b). Unfortunately, the observed velocity structure is mainly associated with IRS1 and kinematic information of IRS2 is missing. Here we can only speculate on the basis of separation that the two sub-cores could be formed by prompt rotational fragmentation of a collapsing protostellar core.

Numerical simulations also predict that the material collapses along the magnetic field lines while the fragmentation occurs in a plane perpendicular to the magnetic field. This is supported by our previous submm polarimetric observations towards

CG 30 (Henning et al. 2001). In contrast to a simple assumption that the angular momenta of two components will be parallel in the fragmentation, we find that the outflows, and hence the angular momentum, of the sub-cores are not aligned, neither in CG 30, nor in BHR 71. This phenomenon is also found in other binary protostars studied recently, like e,g., CB 230 and L 723 (Launhardt 2004; Chapter 2). This could mean that during core fragmentation the initial angular momentum is not evenly (in value and direction) divided between the sub-cores, although the mean direction is preserved all the time (see also discussion in Chapter 6).

3.4.4 N_2H^+ vs. dust vs. CO

From our observations conducted at OVRO (Chapter 2), ATCA (this work), and IRAM-PdBI (see Chapter 4), we find that in most objects the mm continuum source lies within the half maximum level of the N_2H^+ emission. This good general agreement indicates that N_2H^+ is spatially associated with thermal dust in dense protostellar cores and cannot be significantly depleted like, e.g., CO and CS (see Bergin et al. 2001 and Caselli et al. 1999).

Fig. 3.10a shows the distribution of N_2H^+ gas mass (derived independently from the N_2H^+ emission) versus hydrogen gas mass (derived from the dust continuum emission). A clear trend is seen, with higher hydrogen gas masses having higher N_2H^+ gas masses. The data could be fitted by a power-law index of 0.54 ± 0.08 with a correlation coefficient of ~ 0.67, indicating a close correlation. In contrast, the distribution of virial mass versus hydrogen gas mass (see Fig. 3.10b) is more scattered. There is a weak trend (correlation coefficient ~ 0.44) that the virial mass is increasing with the hydrogen gas mass with a power-law index of 0.17 ± 0.10. When viewed in detail, for example, in CG 30, the ratio of gas mass to virial mass is ~ 1.7 in the northern core but ~ 0.36 in the southern core (see Tables 3.2 & 3.4). These mass discrepancies could be understood as that the mm dust continuum emission traces mainly the dense structures (e.g., inner envelope or disk) while N_2H^+ emission traces the larger-scale envelope (see e.g., Figs. 3.1a & 3.2a), hence reflect masses at different scales. Nevertheless, Fig. 3.10b shows that the hydrogen gas mass and virial mass are still consistent with each other at a factor of ~ 2.

On the other hand, we also find that in most objects the morphology of the N_2H^+ emission is directly related to the jet/outflow actions. For example, in BHR 71, two N_2H^+ cores, located to the east and west of the outflow-driving source IRS1, are rotating perpendicular to the outflow axis, and there is no N_2H^+ emission detected at the origin and along the large-scale CO outflow. These features suggest a large N_2H^+ hole has been formed and the two cores may be the remnant of a larger N_2H^+ envelope[6]. It is likely that a large amount of N_2H^+ in the way of the outflow has been destroyed by CO molecules, which is one of the main destroyers of N_2H^+ in the gas phase (Aikawa et al. 2001). For this and this reason, we think that the emission at the position of IRS2 (see Fig. 3.2b) is part of the structure around IRS1 and does not originate from IRS2.

[6]for similar cases see low-mass protostars L 483 (Jørgensen 2004) and IRAM 04191 (Belloche & André 2004).

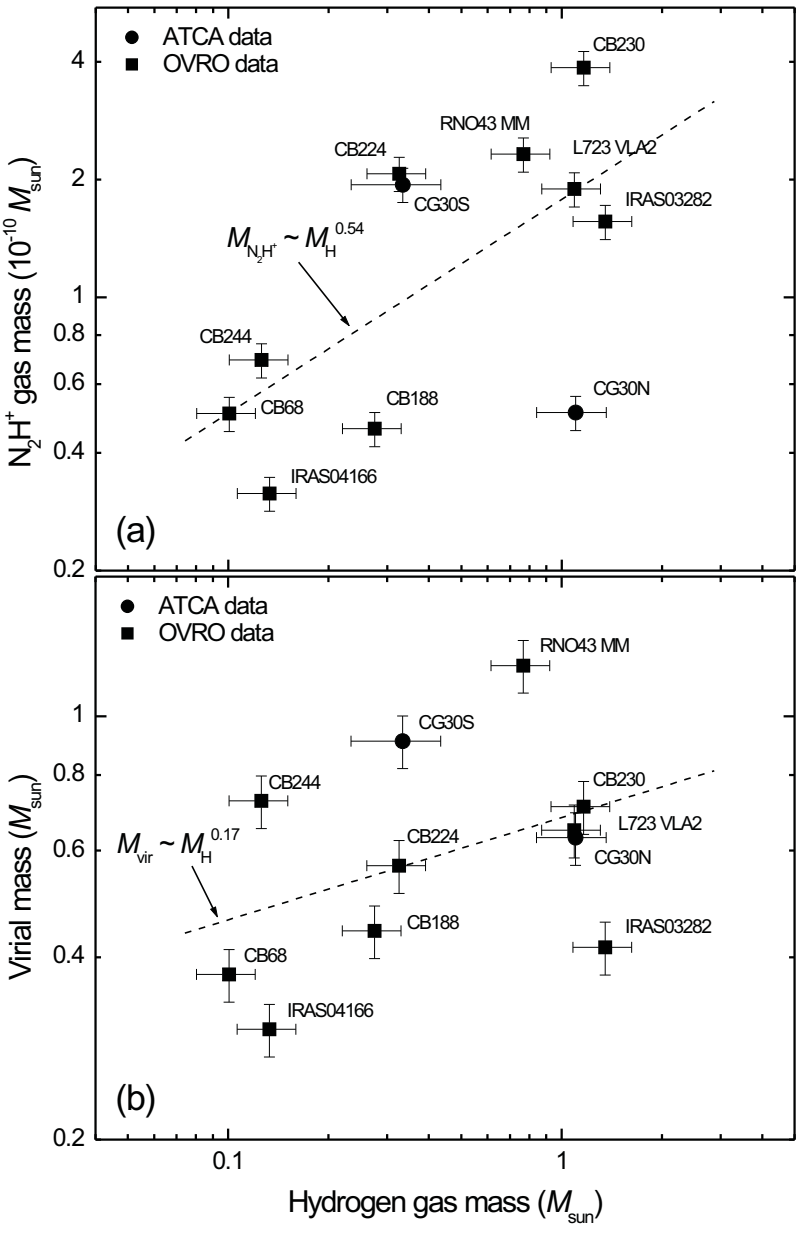

Figure 3.10: (a) N_2H^+ gas mass (derived from the N_2H^+ emission) versus hydrogen gas mass (derived from 3 mm dust continuum emission), and (b) virial mass versus hydrogen gas mass for protostellar cores studied in Chapter 2 and this work. Dashed lines show the fitting results with power-law indexes.

Based on the observational results, we speculate that there are three evolutionary stages during the interaction between N_2H^+ and jets/outflows. (1) When jets are ejected from a protostar, N_2H^+ molecules in the envelope are entrained and show a jet-like morphology in the images, like, e.g., L723 VLA2 (Chapter 2) and CG 30N (this chapter). (2) Molecular outflows, following the jets, release CO from grain surfaces back into the gas phase and start destroying the N_2H^+ molecules on the way, leading to the observed hourglass structure perpendicular to the CO outflow axis, like e.g., IRAS 03282+3035, IRAS 04166+2706, and CB 224 (see Chapter 2). (3) At the end stage, large N_2H^+ holes in the envelopes are finally formed, like, e.g., BHR 71 IRS1 (this chapter), L 483 (Jørgensen 2004), and IRAM 04191 (Belloche and André 2004).

3.5 Conclusions

We have presented ATCA and *Spitzer* observations of the two isolated protostellar double cores CG 30 and BHR 71 in the southern sky. The main conclusions of this work are summarized as follows:

(1) The 3 mm dust continuum image of CG 30 resolves two compact sources with a separation of $\sim 21''$ (8400 AU). In BHR 71, one strong dust continuum source is detected at the position of mid-infrared source IRS1, while only weak emission is detected from the secondary mid-infrared source IRS2. The separation between IRS1 and IRS2 is $\sim 17''$ (3400 AU). Assuming optically thin dust emission, we derive hydrogen gas masses of 1.1 $M_\odot$ and 0.33 $M_\odot$ for northern and southern sources in CG 30, and 2.1 $M_\odot$ and 0.05 $M_\odot$ for IRS1 and IRS2 sources in BHR 71.

(2) N_2H^+ (1–0) emission is detected in both CG 30 and BHR 71. In CG 30, the two dust continuum sources are directly associated with N_2H^+ cores. In BHR 71, two N_2H^+ cores are detected around primary dust continuum source, probably part of one large envelope, but no N_2H^+ is detected at the position of the dust source. The secondary IR source is not detected in N_2H^+.

(3) The excitation temperatures of the N_2H^+ line are $4.7 - 6.8$ K for CG 30 and $3.9 - 4.4$ K for BHR 71. The FWHM radii of N_2H^+ cores range from 730 to 1700 AU. The average fractional abundances of N_2H^+, derived from the ratio of N_2H^+ gas mass to virial mass, is $\sim 2.0 \times 10^{-10}$, which is consistent with the results obtained in our previous study of the cores in northern sky. The observed mean N_2H^+ line widths are $\sim 0.5\,\mathrm{km\,s^{-1}}$ for CG 30 and $\sim 0.3\,\mathrm{km\,s^{-1}}$ for BHR 71. The line widths are roughly constant within the interiors of the cores and large line widths only occur at the edges of the cores. The derived virial masses of the N_2H^+ cores range from 0.2 to 0.9 $M_\odot$.

(4) We derive the N_2H^+ radial velocity fields for CG 30 and BHR 71. The two N_2H^+ cores in CG 30 show systematic velocity gradients of $\sim 24.4\,\mathrm{km\,s^{-1}\,pc^{-1}}$ and $\sim 17.8\,\mathrm{km\,s^{-1}\,pc^{-1}}$ that are parallel to the outflow directions and could be affected by the outflows. In BHR 71, a systematic velocity gradient of $\sim 13\,\mathrm{km\,s^{-1}\,pc^{-1}}$ across the two cores is perpendicular to the large-scale outflow and could be explained by rotation.

(5) Assuming that the observed systematic velocity gradients are due to core rotation (if perpendicular to outflow) or place an upper limit to rotation (if parallel to outflow), we estimate specific angular momenta of < 0.26, < 0.30, and $\sim 0.73 \times 10^{-3}\,\mathrm{km\,s^{-1}\,pc}$ for CG 30N, CG 30S, and BHR 71, respectively. The ratios for the ra-

tional energy to the gravitational potential energy for CG 30N, CG 30S, and BHR 71 are estimated to be < 0.016, < 0.012, and ~ 0.043, respectively. We find that thermal and turbulent energy support are about equally important in the cores, while rotational support is negligible. The cores in both CG 30 and BHR 71 are found to be slightly virially supercritical.

(6) Infrared emission from both sub-cores in both CG 30 and BHR 71 is detected at *Spitzer* IRAC bands and MIPS bands. Each source is driving its own outflow, as seen in the shock-excited 4.5 μm infrared images. CG 30N is associated with a Herbig-Haro flow, while the southern source is driving a large bipolar jet. In BHR 71, both IRS1 and IRS2 are associated with Herbig-Haro objects and driving bipolar jets which coincide spatially with the CO outflows.

(7) By fitting the spectral energy distributions, we derive the dust temperature, bolometric temperature, and bolometric luminosity of the sources. We find that CG 30N is a Class I object while the southern source is a Class 0 protostar. In BHR 71, the properties of IRS1 resemble a Class 0/I transition object, while IRS2 is a Class 0 protostar. We speculate that the sources may nevertheless be coeval but that this evolutionary discrepancy is due to unequal masses and evolutionary speeds.

(8) Based on the morphologies and velocity structures, we suggest that the double cores in CG 30 were formed by initial fragmentation of a filamentary prestellar core, while BHR 71 may originate from rotational fragmentation of a single collapsing protostellar core. We also find that the angular momenta of the sub-cores are not aligned in either pair of sources.

(9) Our observations show a close correlation between thermal dust emission and N_2H^+. The N_2H^+ emission is spatially associated and quantitatively correlated with the dust continuum emission. However, we also find a strong relationship between the morphology of the N_2H^+ emission and the jet/outflow actions. Outflows first seem to entrain N_2H^+ and then gradually destroy it, which leads to the observed hourglass-shaped intensity maps and N_2H^+ hole.

Chapter 4

IRAM-PdBI observations of two binary protostars L1448 IRS3 and SVS 13

This chapter is based on a paper to be submitted to Astrophysics Journal by Chen, Launhardt, & Henning (2008) and a paper prepared for Astrophysics Journal by Chen, Launhardt, Henning, & Goodman, et al. (2008).

4.1 Introduction

Following our observations at OVRO and ATCA, we continue our program at the IRAM Plateau de Bure (PdBI) array. In this chapter, I present our first results from IRAM-PdBI toward two binary protostars L1448 IRS3 and SVS 13. Complementary infrared data from the *Spitzer Space Telescope* (hereafter *Spitzer*) and the ESO *Very Large Telescope* (VLT) are also presented here.

The L1448 complex is located within the Perseus molecular cloud at a distance of ~ 300 pc (Herbig & Jones 1983). Three IRAS point sources, IRS1, IRS2, and IRS3, are revealed in this region. Of these, L1448 IRS3 (IRAS 03225+3034), the brightest source at far-infrared wavelengths, lies in the center of a large-scale NH_3 molecular cloud core (Bachiller & Cernicharo 1986) and is also known as L1448N. L1448 IRS3 consists of three distinct sources which have been resolved at 2.7 mm dust continuum and named A, B, and C, respectively (Looney et al. 2000; hereafter LMW2000). Source A was first detected at 2 and 6 cm by Curiel et al. (1990), coincident with a strong H_2O maser (Anglada et al. 1989; Persi et al. 1994). Source B, located $\sim 7''$ southwest of source A, is a weaker source at cm wavelengths (Curiel et al. 1990), but dominates the emission at mm wavelengths (Terebey & Padgett 1997; LMW2000). Both Barsony et al. (1998) and LMW2000 suggest that sources A and B form a protobinary system embedded in a common envelope. The former study estimates the circumbinary structure contains $1.4\,M_\odot$ of material, while the latter study estimates individual envelopes masses of $0.09\,M_\odot$ and $0.52\,M_\odot$ around sources A and B, respectively. Source C, also called L1448NW (Terebey & Padgett 1997), is located $\sim 20''$ northwest to the AB pair. Barsony et al. (1998) fitted its spectral energy distribution and estimated a bolometric luminosity of $2.7\,L_\odot$ and an envelope mass of $\sim 0.8\,M_\odot$. All three sources were clas-

sified as Class 0 protostars by Barsony et al. (1998). Bipolar CO outflows were also detected from sources A and B (Wolf-Chase et al. 2000).

SVS 13 is a young stellar object (YSO) located in the NGC 1333 star-forming region at a distance of 350 pc (Herbig & Jones 1983)[1]. It was discovered as a near-infrared (NIR) source by Strom et al. (1976). There are at least three mm continuum sources detected around SVS 13 (Chini et al. 1997; Bachiller et al. 1998, hereafter B98) and named A, B, and C, respectively (LMW2000). Source A is coincident with the infrared/optical source SVS 13, source B located $\sim 15''$ southwest of A, and source C further to the southwest (B98; LMW2000). With high-resolution observations, LMW2000 detected another mm source located $\sim 6''$ southwest of source A, which is coincident with the radio source VLA 3 in the VLA survey of this region (Rodríguez et al. 1997; 1999). More recently, Anglada et al. (2000; 2004) revealed that source A is actually a binary system with an angular separation of $0\farcs3$. Located to the southeast of SVS 13 is a classical Herbig-Haro (HH) objects chain 7−11, which was first discussed by Herbig (1974) and Strom et al. (1974), and has been well-studied in the past two decades (see e.g., Khanzadyan et al. 2003 and references therein). Although several possible driving candidates have been proposed for this large-scale HH chain (e.g., Rodríguez et al. 1997), high-resolution CO (2–1) observations (Bachiller et al. 2000, hereafter B2000), as well as an analysis of spectral energy distribution (see LMW2000), clearly favor that SVS13 A is the driving source of the HH 7−11 flow.

4.2 Observations and data reduction

4.2.1 IRAM-PdBI observations

Millimeter interferometric observations of L1448 IRS3 and SVS 13 were carried out with the IRAM PdBI in 2006 March (C configuration with 6 antennas) and July (D configuration with 5 antennas). The two targets were observed with track-sharing mode. The 3 mm and 1 mm bands were observed simultaneously, with baselines ranging from 16 m to 176 m. During the observations, two receivers were tuned to the N_2H^+ (1–0) line at 93.14 GHz and ^{13}CO (2–1) line at 220.40 GHz, respectively. Bandwidths at N_2H^+ line and ^{13}CO line were 20 MHz and 40 MHz, resulting in spectral spacing of 39 kHz and 79 kHz and velocity resolution of 0.2 km s^{-1} and 0.1 km s^{-1}, respectively. The remaining windows of the correlator were combined to observe the continuum emission with a total band width of 500 MHz at both λ 3.1 mm and λ 1.4 mm. The system temperatures of 3 mm and 1 mm receivers were typically $110 - 200$ K and ~ 300 K, respectively. The (naturally-weighted) synthesized beam sizes were $2\farcs8 \times 2\farcs5$ at 93.2 GHz and $1\farcs2 \times 1\farcs1$ at 220.4 GHz. The FWHM primary beam sizes were $\sim 54''$ and $23''$, respectively. Several nearby phase calibrators were observed to determine the time-dependent complex antenna gains. The correlator bandpass was calibrated with the sources 3C273 and 1749+096, while the absolute flux density scale was derived from 3C345. The calibration uncertainty was estimated to be $\sim 15\%$. Only N_2H^+ line data were used here

[1] Although recent VLBA observations suggest a distance of 220 pc (see Hirota et al. 2008), we use here 350 pc for consistency with early papers.

because the signal-to-noise ratio of the ^{13}CO (2–1) line data was too low. Nevertheless, the quality of the 1.4 mm dust continuum data was sufficient for our analysis. The data were calibrated and imaged using the GILDAS software. Observing parameters are summarized in Table 4.1.

4.2.2 Spitzer observations

Mid-infrared data of L1448 IRS3 and SVS 13 were obtained from the *Spitzer* Science Center. L1448 IRS3 was observed by *Spitzer* on 2004 September 8 with the Infrared Array Camera (IRAC; AOR key 5786624) and September 19 with the Multiband Imaging Photometer for *Spitzer* (MIPS: AOR key 5798656). SVS 13 was observed on 2004 September 8 with the IRAC (AOR key 5793280) and September 20 with the MIPS (AOR key 5789440). Both sources were observed as part of the c2d Legacy program (Evans et al. 2003).

The data were processed by the *Spitzer* Science Center using their standard pipeline (version S14.0) to produce Post Basic Calibrated Data (P-BCD) images, which are flux-calibrated into physical units (MJy sr^{-1}). Further analysis and figures were completed with the IRAF and GILDAS software packages.

4.2.3 VLT observations

Near-infrared data of SVS 13 were obtained from the ESO/ST-ECF Science Archive Facility[2]. SVS 13 was observed with NACO (Lenzen et al. 2003; Rousset et al. 2003) at the ESO *VLT* (UT4) on Cerro Paranal in Chile in January and February 2005. The detector of NACO is an Aladdin InSb 1024 × 1024 pixel array. The camera used was S27, which provides pixel scale of 27.03 mas pixel^{-1} with a field of view of $28'' \times 28''$.

The observations were carried out in the H_2 (1–0) S(1) band (central wavelength 2.122 μm, bandwidth $\sim$ 0.022 μm). Observation parameters are summarized in Table 4.2. The data reduction was carried out using self-developed IDL scripts. After bad-pixel filtering, flat-field correction, and sky removal, the individual dithering positions were combined into a resulting mosaic image. Further analysis and figures were completed with the GILDAS software package.

4.3 Results

4.3.1 PdBI results

The 3 mm dust continuum images (see Fig. 4.1) show three distinct sources in both L1448 IRS3 and SVS 13. Following LMW2000, the sources are labeled A, B, and C, respectively. L1448 IRS3 C and SVS 13 C, the weakest sources in both objects, unfortunately lie outside the field of view at 1.4 mm. From gaussian *uv* plane fitting, we derive flux densities and deconvolevd FWHM sizes for all sources (see Table 4.3).

[2]http://archive.eso.org

Table 4.1: Target list and summary of the IRAM-PdBI observations.

Object Name	Other Name	R.A. & Dec. (J2000)[a] [h : m : s, ° : ′ : ″]	Distance [pc]	Array configuration	HPBW[b] [arcsecs]	rms[c] [mJy/beam]
L1448 IRS3	L1448N	03:25:36.30, 30:45:15.00	300	CD	2.8×2.5, 1.2×1.1	18.6, 0.66, 3.9, 100
SVS13	HH 7−11	03:29:03.20, 31:15:56.00	350	CD	2.8×2.5, 1.2×1.1	15.5, 0.62, 3.7, 120

[a]Reference position for figures and tables in this chapter, except *Spitzer* images.
[b]Naturally-weighted synthesized FWHM beam sizes at 3 mm and 1.4 mm dust continuum.
[c]1 σ noises at N_2H^+ (1–0) channel, 3 mm dust continuum, 1.4 mm dust continuum, and velocity-integrated N_2H^+ intensity maps.

Table 4.2: VLT/NACO observation logs of SVS 13[a].

Obs. date (UT Date)	DIT×N[b] [s]	Seeing [″]	Airmass
2005 Jan. 11	5.0×5	0.73	1.8
2005 Jan. 21	5.0×2	1.00	1.9
2003 Jan. 29	5.0×5	0.94	2.0
2003 Feb. 17	15.0×5	0.86	2.3

[a]The observations were carried out in the H_2 (1–0) S(1) band with S27 camera.
[b]DIT and N correspond to the exposure integration time and the number of exposures, respectively.

Table 4.3: PdBI mm dust continuum results for L1448 IRS3 and SVS 13.

Source	Position[a]		S_ν[b] [mJy]		FWHM sizes at 3 mm		$M_{\rm H}$ (3 mm)	$M_{\rm H}$ (1.4 mm)
	α(J2000)	δ(J2000)	λ3.1 mm	λ1.4 mm	maj.×min.	P.A.	[$M_\odot$]	[$M_\odot$]
L1448 IRS3 A	03:25:36.53	30:45:21.35	12.2±1.8	104±16	$\sim 1\farcs5$	−−	0.6±0.1	0.39±0.06
B	03:25:36.33	30:45:14.87	84±12	602±90	$2\farcs4\times2\farcs0$	31±4°	4.1±0.6	2.23±0.33
C	03:25:35.68	30:45:33.39	7.1±2.3	−−	$\sim 1\farcs1$	−−	0.3±0.1	−−
SVS 13 A	03:29:03.75	31:16:03.76	30.0±4.5	135±21	$2\farcs4\times1\farcs4$	–58±6°	1.3±0.2	0.42±0.07
B	03:29:03.07	31:15:52.02	42.4±6.4	193±30	$2\farcs7\times1\farcs8$	–46±5°	2.8±0.4	0.97±0.15
C	03:29:01.96	31:15:38.26	6.5±1.0	−−	$\sim 0\farcs7$	−−	0.3±0.1	−−

[a]Center position of the continuum sources from gaussian uv plane fitting at 3 mm.
[b]The error bar is derived from $\sqrt{\sigma_{\rm cali}^2+\sigma_{\rm fit}^2}$, where $\sigma_{\rm cali}$ is the uncertainty from calibration ($\sim$15% of flux density) and $\sigma_{\rm fit}$ is the uncertainty from gaussian fitting.

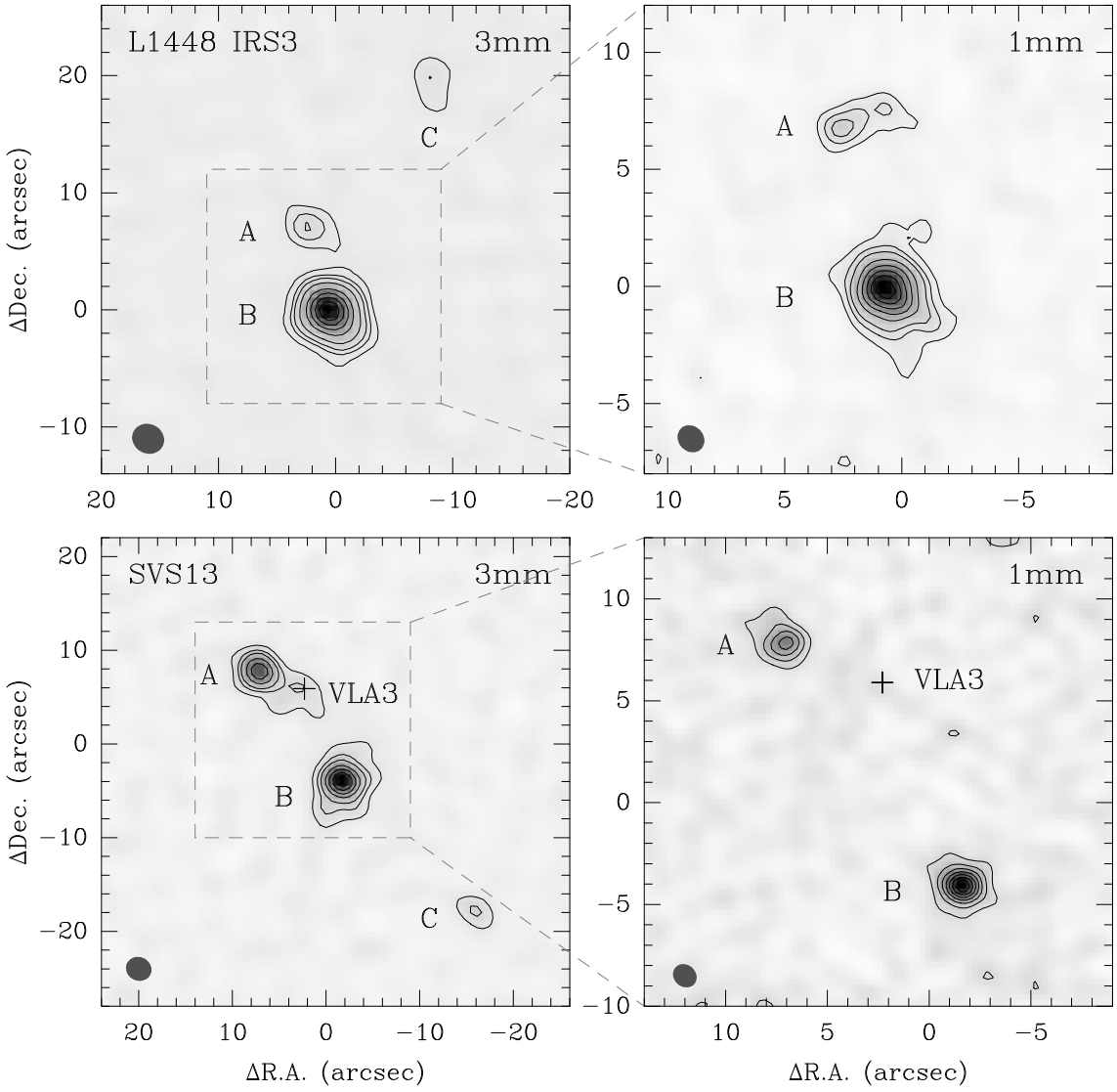

Figure 4.1: IRAM-PdBI 3 mm and 1.4 mm dust continuum images of L1448 IRS3 (up) and SVS 13 (bottom). Contours start at $\sim 3\,\sigma$ (see Table 4.1) by steps of $\sim 2\,\sigma$. The crosses in the SVS 13 images mark the position of the radio source VLA 3 (Rodríguez et al. 1997). The synthesized PdBI beams are shown as grey ovals.

In L1448 IRS3, the dust continuum emission is dominated by source B at both 3 mm and 1.4 mm. The common envelope around sources A and B, detected by single-dish sub-mm observations (Barsony et al. 1998), is resolved out by the interferometer at both wavelengths. Compared with compact structures seen at 3 mm, both A and B show relatively extended emission at 1.4 mm. The separation between A and B is measured to be $6\farcs7 \pm 0\farcs5$, corresponding to ~ 2000 AU at a distance of 300 pc.

In SVS 13, the large-scale common envelope of the three sources, detected in the submm (SCUBA; Chandler & Richer 2000) and mm (IRAM-30 m; Chini et al. 1997) single-dish maps, is also resolved out. The measured angular separations are $14\farcs6 \pm 0\farcs2$

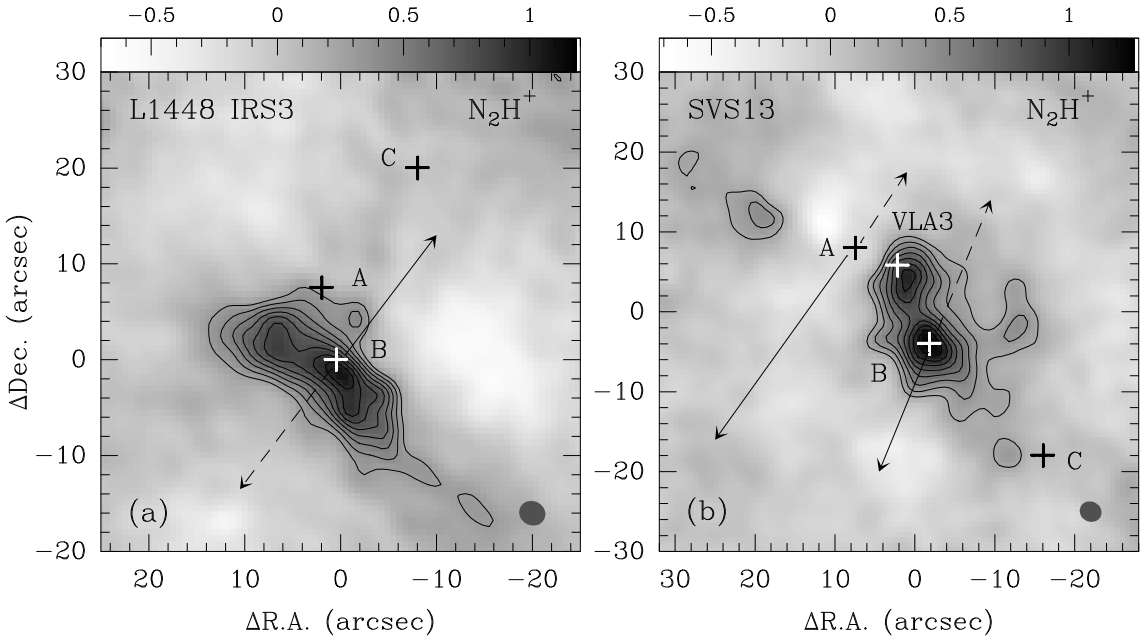

Figure 4.2: Images of the N_2H^+(1-0) intensity integrated over the seven hyperfine line components for L1448 IRS3 (left) and SVS 13 (right). The unit of the scale is [Jy beam^{-1} km s^{-1}]. Contours start at $\sim 3\,\sigma$ (see Table 4.1) with steps of $\sim 2\,\sigma$. Crosses represent the peaks of 3 mm dust continuum emission. Solid and dashed arrows show the direction of blue- and red-shifted outflows. Synthesized PdBI beams are shown as grey ovals.

between sources A and B, and $19\farcs8 \pm 0\farcs2$ between B and C. A weak emission peak, spatially coincident with the radio source VLA 3 (Rodríguez et al. 1997) and the 2.7 mm dust continuum source A2 in LMW2000, is detected in the 3 mm dust continuum image but not seen in the higher-resolution 1.4 mm image (see Fig. 4.1). Hereafter, we refer this weak 3 mm continuum source as VLA 3.

Assuming that the mm dust continuum emission is optically thin, the total gas mass in the circumstellar envelope was calculated with the same method as described in Launhardt & Henning (1997). In the calculations, we adopt an interstellar hydrogen-to-dust mass ratio of 110, and dust opacities of $\kappa_{1.4\mathrm{mm}} = 0.8\,\mathrm{cm^2\,g^{-1}}$ (a typical value for dense protostellar cores; see Ossenkopf & Henning 1994) and of $\kappa_{3\mathrm{mm}} \approx 0.2\,\mathrm{cm^2\,g^{-1}}$ (using $\kappa \propto \nu^{1.8}$). Dust temperature of the objects in L1448 IRS3 is adopted as 22 K (see Barsony et al. 1998); the dust temperatures of the objects in SVS 13 are derived from SED fitting (§ 4.4.1) and listed in Table 4.8. The derived masses, ranging from 0.3 to 4.1 $M_\odot$ at 3 mm and from 0.4 to 2.2 $M_\odot$ at 1.4 mm, are listed in Table 4.3.

N_2H^+ emission is detected from both sources. Figure 4.2 shows the velocity-integrated intensity images of both sources. The emission was integrated over all seven components, using frequency masks that completely cover velocity gradients within the objects. In L1448 IRS3 (Fig. 4.2a), a core, spatially coincident with the mm continuum source B, is seen. This core is elongated in the northeast-southwest direction, i.e., roughly perpendicular to the axis of the CO outflow driven by source B. In SVS 13 (Fig. 4.2b), a core, spatially associated with the mm continuum sources B and VLA 3,

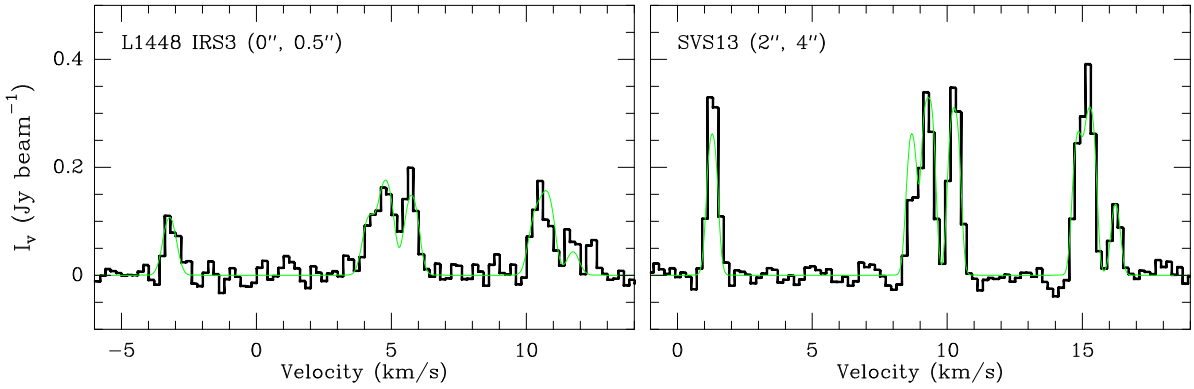

Figure 4.3: N_2H^+ spectra at the peak positions of L1448 IRS3 (left) and SVS 13 (right). Green solid curves show the results of hyperfine structure line fitting. Fit parameters are given in Table 4.4.

Table 4.4: Observing parameters from N_2H^+ (1-0) spectra fitting

	$V_{\rm LSR}{}^a$ [km s^{-1}]	$\triangle v^a$ [km s^{-1}]	$\tau_{\rm tot}{}^a$	$T_{\rm ex}{}^a$ [K]	$\triangle v_{\rm mean}{}^b$ [km s^{-1}]	$\triangle v_{\rm NT}{}^c$ [km s^{-1}]
L1448 IRS3	4.43±0.03	0.89±0.03	1.6±0.1	7.6±0.1	0.81±0.01	0.79
SVS 13	8.39±0.01	0.46±0.02	2.2±0.1	10.1±0.5	0.48±0.01	0.44

[a]Value at the intensity peak. The error represents 1 σ error in the hyperfine fitting.
[b]Mean line width obtained through gaussian fitting.
[c]Non-thermal line width at the given dust temperature (see Table 4.8).

is also seen and elongated in the northeast-southwest direction but double-peaked: one peak is coinciding with source B and the other is located $\sim 2''$ southwest to VLA 3. The FWHM radius of the core is measured to be $\sim$1520 AU. An emission jet is seen at the western edge of the core, which is $\sim 10''$ in size and extends to northwest. Two smaller clumps, one located close to source C and the other located $\sim 10''$ northeast of source A, are also seen in the image (see Fig. 4.2b).

Figure 4.3 shows the N_2H^+ (1–0) spectra at the peak positions of L1448 IRS3 and SVS 13. Seven hyperfine complex of the N_2H^+ (1–0) line have been detected in both sources. Using the hyperfine fitting program in CLASS, we derive LSR velocity ($V_{\rm LSR}$), intrinsic line width ($\triangle v$; corrected for instrumental effects), total optical depth ($\tau_{\rm tot}$), and excitation temperature ($T_{\rm ex}$) (see Table 4.4).

By simultaneously fitting the seven hyperfine components with the routine described in Chapter 2, we derive the mean velocity field of L1448 IRS3 and SVS 13 (see Fig. 4.4). The outflow information is also shown in the two images. Both L1448 IRS3 and SVS 13 show well-ordered velocity fields, with velocity gradients increasing from southwest to northeast. In L1448 IRS3, the gradient is roughly perpendicular to the axis of the outflow, while in SVS 13, the gradient is $> 50°$ across the axis of outflow driven by source B. A least-squares fitting of velocity gradients has been performed with

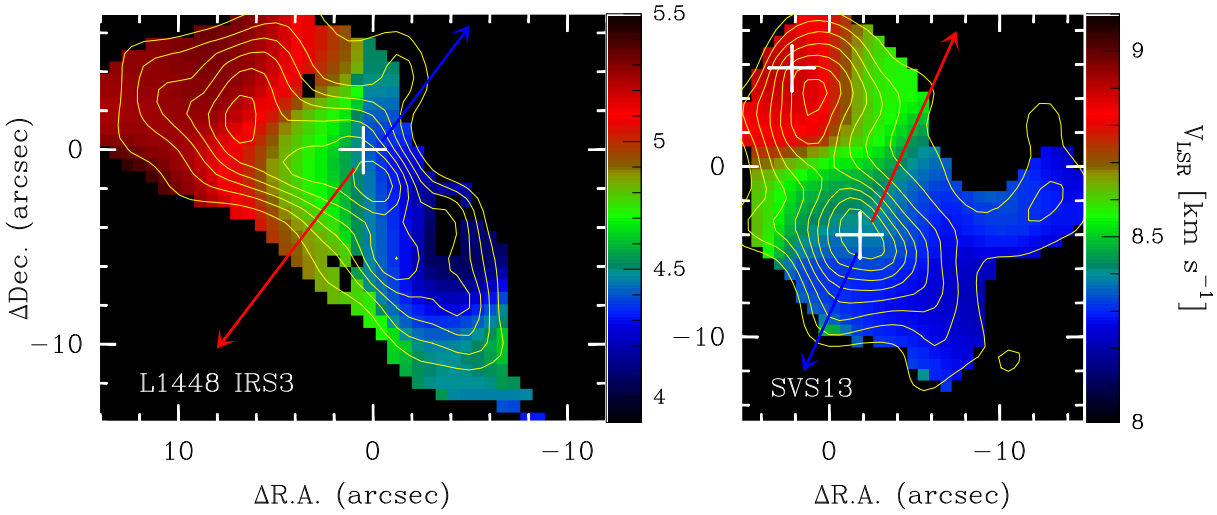

Figure 4.4: N_2H^+ velocity field maps of L1448 IRS3 (left) and SVS 13 (right). Contours and crosses are same as in Fig. 4.2. The red and blue arrows show the directions of red- and blueshifted CO outflows.

Table 4.5: Volume size, density, and mass of N_2H^+

Source	R [AU]	$M_{\rm vir}$ [$M_\odot$]	$n_{\rm vir}$ [$\times 10^6$ cm^{-3}]	$N(N_2H^+)$ [$\times 10^{12}$ cm^{-2}]	$M_{N_2H^+}$ [$\times 10^{-10}$ $M_\odot$]	$X(N_2H^+)$ [$\times 10^{-10}$]
L1448 IRS3	1500	1.67	18.0	8.36	4.1	3.3
SVS 13	1520	0.91	9.4	6.37	4.3	6.4

the routine described in Goodman et al. (1993). The fitting results are summarized in Table 4.6. The details of the velocity fields are discussed in § 4.4.2.

Figure 4.5 (top) shows the spatial distribution of N_2H^+ line widths for L1448 IRS3 and SVS 13. In the two sources, the line widths are roughly constant within the interiors of the cores, which is consistent with the observational results found in Chapter 2 and Chapter 3. The mean line width of two objects are derived from gaussian fitting to the distribution of line widths versus solid angle area (see Fig. 4.5 bottom and Table 4.4). The virial masses of the N_2H^+ cores (see Table 4.5) are then calculated using the same method described in Chapter 2.

Table 4.6: Velocity gradients and specific angular momenta

Source	mean velocity [km s^{-1}]	g [km s^{-1} pc^{-1}]	Θ_g^a [degree]	g_r [km s^{-1}]	J/M [$\times 10^{-3}$ km s^{-1} pc]
L1448 IRS3	4.77	61.3±0.2	88±1	0.92	~ 0.86
SVS 13	8.59	28.0±0.1	51±1	0.43	~ 0.40

[a]East of north in the direction of increasing velocity

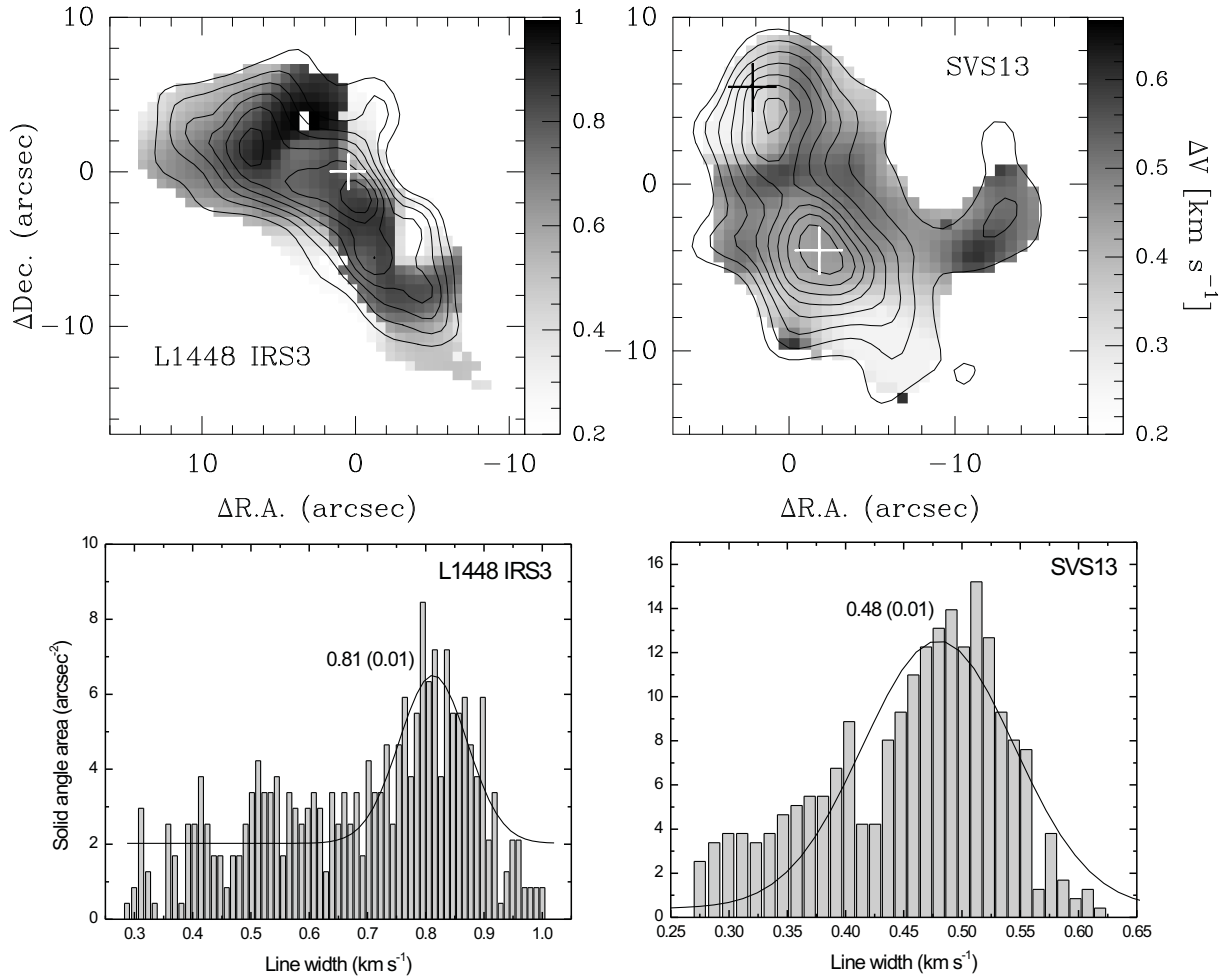

Figure 4.5: *Top*: Spatial distribution of N_2H^+ line widths in L1448 IRS3 (left) and SVS 13 (right), as derived from the HFS line fitting. Contours and symbols are the same as them in Fig. 4.2. *Bottom*: Distribution of N_2H^+ line widths versus solid angle areas for L1448 IRS3 (left) and SVS 13 (right). Black solid curves and numbers show the results of Gaussian fitting to the distributions.

4.3.2 *Spitzer* and VLT results

Figure 4.6 shows the *Spitzer* images of L1448 IRS3. Fig. 4.6a shows a wide-field IRAC 2 (4.5 μm) image of L1448 complex, in which three Class 0 sources L1448 IRS2, L1448 IRS3, and L1448C (also known as L1448-mm) are labeled. Centered at L1448C is a well-studied collimated bipolar jet, which is associated with high-velocity outflow seen at SiO (Guilloteau et al. 1992) and CO (Bachiller et al. 1995). Its northern lobe shows multiple bow-shocked structures and rushes directly into L1448 IRS3, in which two infrared sources are found (see Fig. 4.6a).

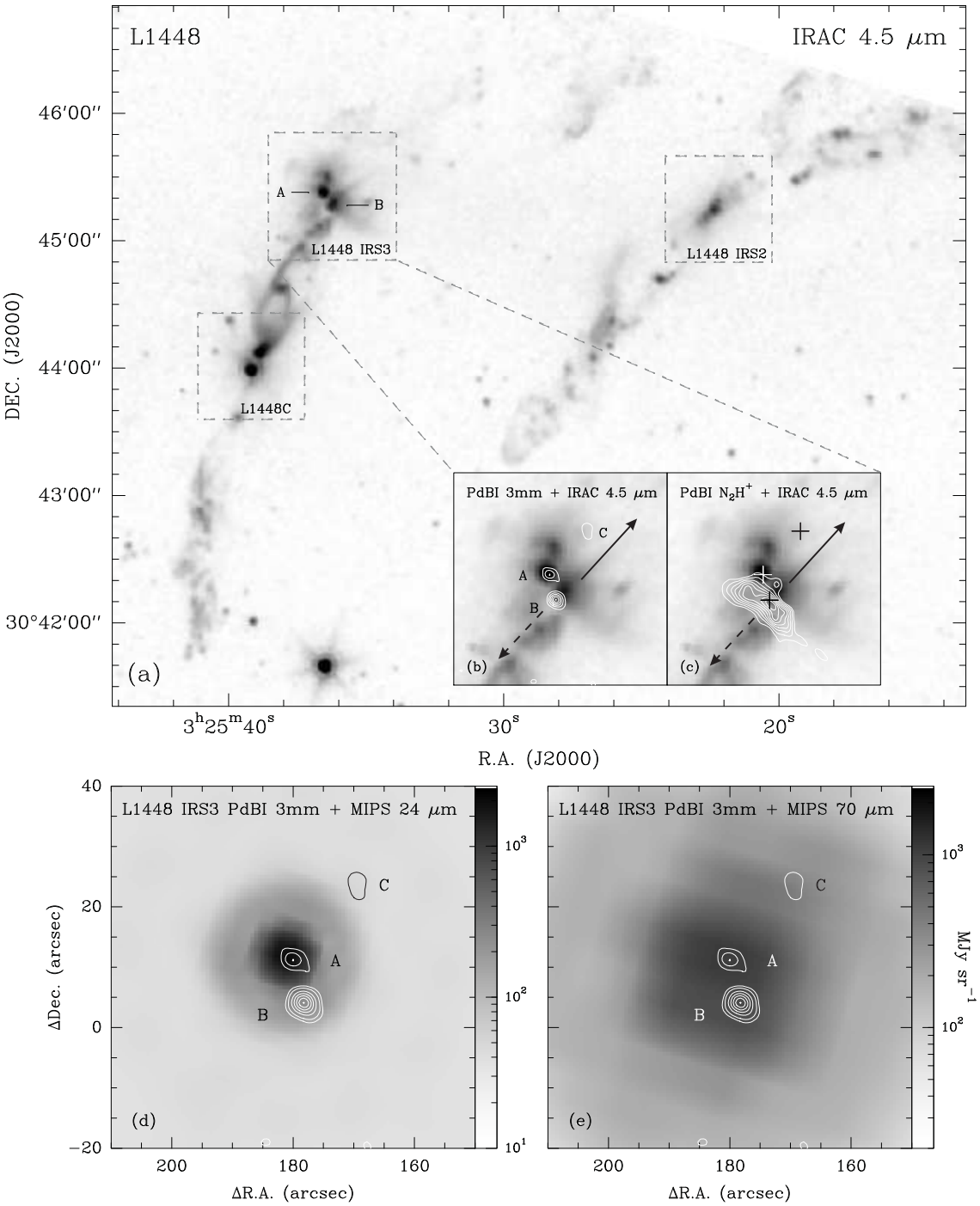

Figure 4.6: *Spitzer* images of L1448 IRS3. (a) *Spitzer* IRAC band 2 (4.5 μm) image of L1448 complex. (b) IRAC band 2 image of L1448 IRS3 overlaid with the PdBI 3 mm dust continuum contours. (c) Same, but overlaid with the PdBI N_2H^+ intensity contours; (d) *Spitzer* MIPS 1 (24 μm) image of L1448 IRS3, overlaid with the PdBI 3 mm dust continuum contours (reference center at R.A.=03:25:22.51, DEC=30:45:10.85, J2000); (e) *Spitzer* MIPS 2 (70 μm) image of L1448 IRS3, overlaid with the PdBI 3 mm dust continuum contours.

Figs. 4.6b and 4.6c show enlarged views of L1448 IRS3, overlaid with the contours from the PdBI 3 mm dust continuum and N_2H^+ images. The two infrared sources are spatially coincident with their dust continuum sources. The emission around source B shows an elongated structure, with source B being at the apex, implying that the infrared emission is due to the scattered light in a cavity evacuated by the outflow (see Chpater 3 for similar cases). Located to the north of source A is an infrared knot (see Fig. 4.6b), which was previously found in the H_2 (1–0) S(1) image by Curiel et al. (1999) and could be ejected by source A. In the MIPS 1 (24 μm) image shown in Fig. 4.6d, the emission is peaked at source A and few emission is found at source B. At MIPS 2 band (70 μm; see Fig. 4.6e), the emission is extended at the AB pair and sources A and B are not resolved. No infrared emission is detected from source C at all IRAC bands and MIPS bands, suggesting that source C is either a deeply embedded protostar or a very low luminosity object under the detecting sensitivities of the *Spitzer*.

Figure 4.7 shows the *Spitzer* images of SVS 13, with the same sequence as in Fig. 4.6. In the wide-field IRAC 2 image shown in Fig. 4.7a, a number of HH objects are seen, implying active star formation in the NGC 1333 region. The HH objects that can be clearly distinguished are labeled by the same numbers as in Bally et al. (1996; for a comparison see their optical image in Figure 2). In the IRAC maps, a strong infrared source is spatially coinciding with the dust continuum source A. Located to the southeast of source A is the well-known HH chain $7-11$ (see Fig. 4.7b), which is associated with high-velocity blue-shifted CO outflow (B2000). Another collimated jet is found in the south of SVS 13 with the continuum source C being located at the apex (see Fig. 4.7b), but no infrared source is found at this position. Fig. 4.7c shows that the N_2H^+ emission is not spatially associated with the infrared emission, but roughly perpendicular to the directions of the jets/outflows.

In the MIPS 1 image, a strong infrared source is again found at source A, and another weak one is found at source C. In the MIPS 2 image, extended emission are seen at sources A and C. It should be noted that no infrared emission is detected from source B at all IRAC and MIPS bands, which could be explained in the same way as source C in L1448 IRS3. Flux densities of sources A and C are measured with aperture photometry in the IRAF APPHOT package, with the radii, sky annuls, and aperture corrections recommended by the *Spitzer* Science Center (see Table 4.7).

Figure 4.8 shows the H_2 narrow band images of SVS 13 A, taken by NACO/VLT at four different epochs. In the images, a single (unresolved) star is found at the position of SVS 13 A. Another young stellar object ASR 2 (Aspin et al. 1994), located $\sim 11\farcs5$ southwest of SVS 13A, appears to be a close binary[3] with an angular separation of $0\farcs12 \pm 0\farcs01$ (42 AU at a distance of 350 pc).

4.4 Discussion

Our discussion is focused on SVS 13. The results of L1448 IRS3 will be discussed together with other objects in Chapter 6. More details of L1448 IRS3, as well as the

[3]This object is only resolved in the image taken on January 11 2005, i.e., in the best observational conditions (see Table 4.2).

Table 4.7: *Spitzer* flux densities of L1448 IRS3 and SVS 13

Source	R.A.[a] (J2000)	Dec.[a] (J2000)	$S(3.6\,\mu m)$ [mJy]	$S(4.5\,\mu m)$ [mJy]	$S(5.8\,\mu m)$ [mJy]	$S(8.0\,\mu m)$ [mJy]	$S(24\,\mu m)$ [Jy]	$S(70\,\mu m)$ [Jy]
L1448 IRS3 A	03:25:36.52	30:45:23.23	1.2±0.2	10.5±0.3	45.3±1.3	149.5±2.3	4.4±0.1	28.5±0.2
B	03:25:36.21	30:45:17.15	1.6±0.3	4.7±0.5	5.7±0.5	55±1	−−	−−
SVS 13 A	03:29:03.73	31:16:03.80	312.5±3.4	543.1±4.4	2607±10	2433±10	20.76±0.06	111.7±0.3
C	03:29:01.98	31:15:38.17	$< 0.36^b$	$< 0.43^b$	$< 1.3^b$	$< 0.54^b$	0.22±0.01	12.2±0.1

[a]Peak position of infrared sources measured at the IRAC band 3 (5.8 μm).
[b]IRAC sensitivities of the *Spitzer*.

Table 4.8: Fitting results of the spectral energy distribution for SVS 13.

Source	$T_{\rm dust}$ [K]	$T_{\rm bol}$ [K]	$L_{\rm bol}$ [$L_\odot$]	$L_{\rm submm}$ [$L_\odot$]	$L_{\rm submm}/L_{\rm bol}$ [%]	Classification
SVS 13 A	33	114	46.6	0.37	0.8	0/I(?)
B	22	28	5.6	0.28	5.0	0
C	32	38	4.3	0.09	2.1	0

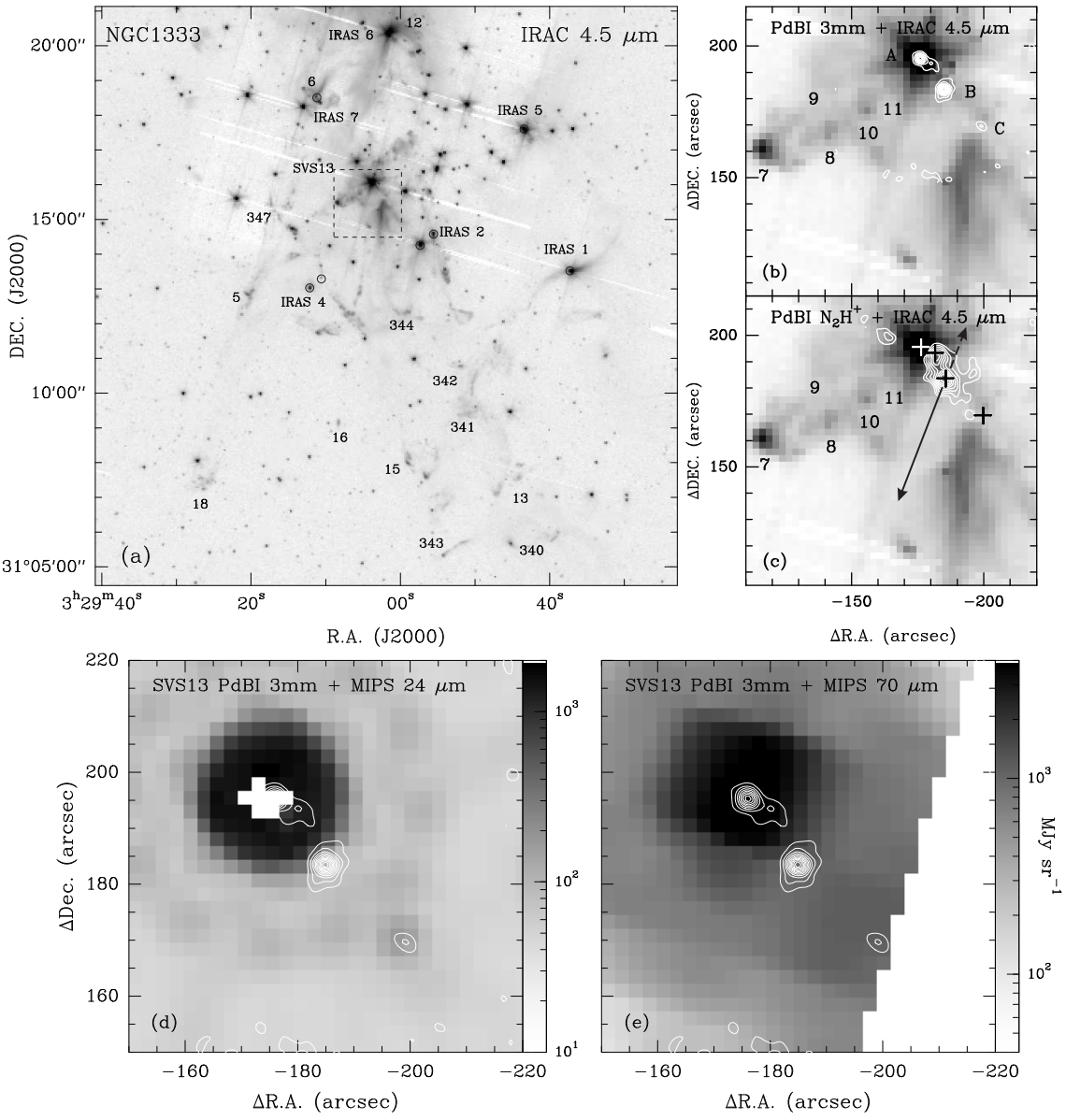

Figure 4.7: The same as Fig. 4.6, but for SVS 13 (reference center at R.A.=03:29:17.49, DEC=31:12:48.54, J2000).

forthcoming IRAM-PdBI data of L1448C and L1448 IRS2, will be presented in a separate paper prepared by Chen, Launhardt, Henning, & Goodman, et al.

4.4.1 Spectral energy distributions and evolutionary stages

Figure 4.9 shows the spectral energy distributions (SEDs) of SVS 13, based on the infrared (*Spitzer* and IRAS), sub-mm (SCUBA), and mm (IRAM-30 m, BIMA, and PdBI) observations. IRAS far-infrared (only 100 μm data used here) data are adopted from Jennings et al. (1987); SCUBA submm data from Chandler & Richer (2000);

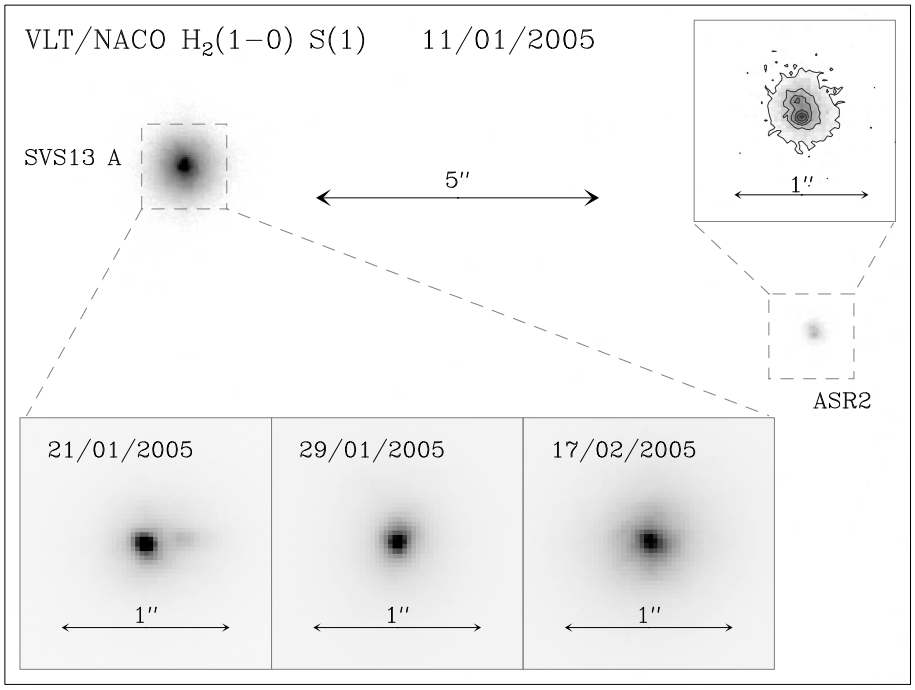

Figure 4.8: VLT/NACO S27 image of SVS 13 A in the H_2 (1-0) S(1) narrow band. North is up and east is to the left. The scale is marked in each map.

IRAM-30 m 1.3 mm data from Chini et al. (1997)[4]; BIMA 2.7 mm data from LMW2000; IRAM PdBI 3.1 mm data from this work and 3.5 mm data from B98. Since IRAS could not resolve SVS 13, the ratio of 8:1:1 (A : B : C) was inferred for the flux density at 100 μm, according to the ratios estimated from other observations. For source B, the *Spitzer* sensitivities at IRAC bands (also for source C) and MIPS bands are adopted[5].

In order to derive luminosity and temperature, we first interpolated and then integrated the SEDs, always assuming spherical symmetry. Interpolation between the flux densities was done by a χ^2 grey-body fit to all points at $\lambda \geq 100\,\mu$m, using the same method described in Chapter 3. A simple logarithmic interpolation was performed between all points at $\lambda \leq 100\,\mu$m. The fitting results are summarized in Table 4.8.

The fitting results of sources B and C confirm the early suggestions (see e.g., Chandler & Richer 2000) that both sources are Class 0 protostars. For source A, the high bolometric temperature (~ 114 K) and direct detection in the NIR wavelengths suggest it is a Class I young stellar object. However, we want to note that source A resembles a Class 0 protostar in at least two ways: (1) it is associated with a cm radio source (VLA 4; Rodríguez et al. 1999) and embedded in a large-scale (not remnant) dusty envelope, and (2) it is driving an extremely high velocity CO outflow (B2000), which is believed to be one of the characteristics of Class 0 protostars (see a review by Bachiller 1996). As already mentioned by B2000, we speculate that source A could be a Class 0/I

[4] Although IRAM PdBI 1.3 mm and 1.4 mm data are available in B98 and this work, here we prefer using the single-dish data.

[5] see http://ssc.spitzer.caltech.edu/irac/sens.html and http://ssc.spitzer.caltech.edu/mips/sens.html

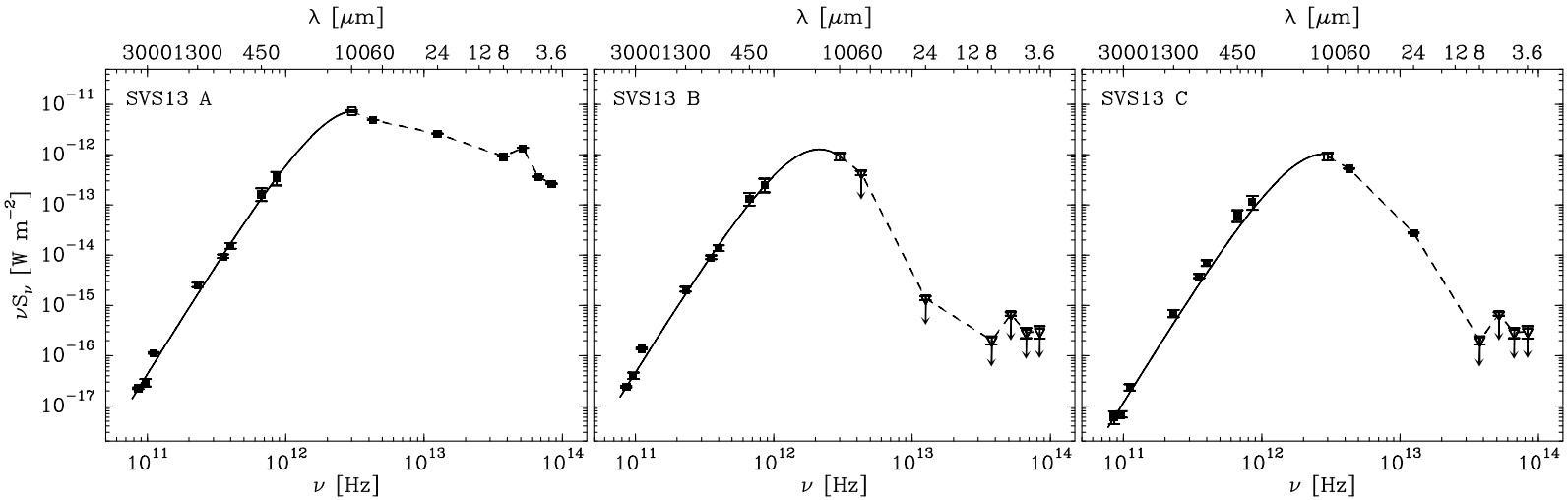

Figure 4.9: Spectral energy distributions of SVS 13A (left), B (middle), and C (right). Error bars ($1\,\sigma$) are indicated for all data points. Solid squares represent real observational data points. Open squares represent IRAS 100 μm data points, where flux densities are estimated for the three sources with ratios assumed in § 4.4.1. Open triangles represent the sensitivities of the IRAC and MIPS. Solid lines show the best-fit for all points at $\lambda \geq 100\,\mu$m using a grey-body model. Dashed lines at $\lambda \leq 100\,\mu$m show the simple logarithmic interpolation used to derive the luminosity. The fitting results are summarized in Table 4.8.

(or even Class 0) protostar, which is visible in the infrared wavelengths due to high inclination angle. Indeed, the bipolar CO outflow driven by source A is far from being symmetrical (see B2000), suggesting a high inclination angle.

4.4.2 Gas kinematics of SVS 13

4.4.2.1 Subsonic turbulent motion

Assuming that the kinetic gas temperature is equal to the dust temperature ($\sim 20\,\mathrm{K}$; see Table 4.8 for source B), the thermal line widths of N_2H^+ and an "average" particle of mass $2.33\,m_H$ (assuming gas with 90% H_2 and 10% He) are calculated to be ~ 0.18 and $\sim 0.62\,\mathrm{km\,s^{-1}}$, respectively. The latter line width represents the local sound speed. The non-thermal contribution to the N_2H^+ line width ($\triangle v_{\mathrm{NT}} = \sqrt{\triangle v^2_{\mathrm{mean}} - \triangle v^2_{\mathrm{th}}}$) is then estimated to be $\sim 0.44\,\mathrm{km\,s^{-1}}$, which is about two times larger than the thermal line width but smaller than the local sound speed (i.e., subsonic).

It is widely accepted that turbulence is the main contribution to the non-thermal line width (Barranco & Goodman 1998; Goodman et al. 1998), while infall, outflow, and rotation could also broaden the line width. The spatial distribution of the line widths in SVS 13 (see Fig. 4.5) shows that large line widths ($\geq 0.45\,\mathrm{km\,s^{-1}}$) occur mainly in the gap between sources B and VLA 3 and the emission jet at the edge of the core. At or around the two sources, line widths are relatively small ($0.3 - 0.4\,\mathrm{km\,s^{-1}}$). We suggest that the large line widths in the gap are caused by core rotation (see below; see also CB 230 in Chapter 2 for a similar case). Taken out this rotating effect, the corrected non-thermal line width would be $0.35 - 0.4\,\mathrm{km\,s^{-1}}$. Although this corrected result is still larger than the thermal line, it is fair to say that the turbulence in SVS 13 is at a low level.

4.4.2.2 Fast rotation

The radial velocity field derived from N_2H^+ line observations shows a clear velocity gradient across the core of $\sim 28\,\mathrm{km\,s^{-1}\,pc^{-1}}$ increasing from southwest to northeast, i.e., roughly along the connection line between sources B and VLA 3. As discussed in Chapter 2, systematic velocity gradients are usually dominated by either rotation or outflow. As shown in Fig. 4.4, the large cross angle ($> 50°$) between the gradient and the outflow axis strongly supports that this systematic velocity gradient is due to core rotation rather than outflow.

The velocity gradient derived in SVS 13 is much larger than the results found in Chapters 2 & 3 ($\sim 7 - 10\,\mathrm{km\,s^{-1}\,pc^{-1}}$) and other Class 0 objects, like, e.g., IRAM 04191 ($\sim 7\,\mathrm{km\,s^{-1}\,pc^{-1}}$; Belloche et al. 2002) and NGC1333 IRAS4 ($\sim 10\,\mathrm{km\,s^{-1}\,pc^{-1}}$; Belloche et al. 2006), suggesting a fast rotation. With this gradient and the FWHM core size ($\sim 1520\,\mathrm{AU}$), the specific angular momentum J/M is calculated to be $\sim 0.4 \times 10^{-3}\,\mathrm{km\,s^{-1}\,pc}$ ($\sim 1.25 \times 10^{16}\,\mathrm{m^2\,s^{-1}}$), using the same method described in Chapter 2.

4.4.2.3 Energy balance

Assuming that the non-thermal line width and the velocity gradient are due to turbulence and core rotation, respectively, we could estimate the contribution of different terms to the total energy balance and derive the ratios of rotational, thermal, and turbulent energy to gravitational potential energy (for equations see Chapter 2).

The estimated $\beta_{\rm rot}$, $\beta_{\rm therm}$, and $\beta_{\rm turb}$ values of SVS 13 are $\sim 0.023/sin^2i$, 0.27, and 0.13, respectively. As previously found in Chapter 2, both thermal and turbulent contributions dominate the support of the core, while the thermal contribution about two times outweighs turbulence. The rotational support is relatively small and could be negligible. When we apply the equilibrium virial theorem $2[E_{\rm therm} + E_{\rm turb} + E_{\rm rot}] + E_{\rm grav} = 0$ (in the absence of magnetic field) and assume $sin^2i = 1$, $\beta_{\rm vir} = 2(\beta_{\rm rot} + \beta_{\rm therm} + \beta_{\rm turb}) - 1$ is about -0.15, suggesting the core is slightly supercritical.

4.4.3 SVS 13 A: single or binary?

High-resolution VLA observations have resolved SVS 13 A into a binary system (VLA 4A and VLA 4B) with an angular separation of $0\farcs3$ (Anglada et al. 2000). In this system, only one component (VLA 4B) is associated with a substantial amounts of circumstellar dust, while the other (VLA 4A) is characterized by free-free emission at cm wavelengths (Anglada et al. 2004).

In our VLT/NACO images, however, SVS 13 A remains as a single (unresolved) star. The coordinate of the star is measured to be 03:29:03.76.0 $\pm$0.1, +31:16:03.94 $\pm$ 1.0 (J2000)[6], coinciding with the dust continuum source detected by IRAM-PdBI and the radio source VLA 4B. It suggests this star is the infrared counterpart of the dust continuum source A (at $1-3$ mm) and radio source VLA 4B (at $0.7-3.6$ cm), which is in contrast to the suggestion by Anglada et al., who considered that VLA 4A is the counterpart of the optical/infrared star SVS 13.

Only one star being detected in the VLA/NACO images makes us doubt the binary qualification of SVS 13 A. There is a possibility that VLA 4A is a deeply embedded source, from which no infrared emission emerges yet. Indeed, the water masers associated with SVS 13 A appear segregated in position and velocity, supporting the binary hypothesis (see Rodríguez et al. 2002). More high-resolution observations are needed in future to determine the natures of these two components. In the discussion below, we still assume SVS 13 A as a close protobinary system.

4.4.4 SVS 13 B and VLA 3: a bound protobinary system

Our 3 mm dust continuum observations find a weak source at the position of the radio source VLA 3. Angular separation and flux density ratio between sources B and VLA 3 are measured to be $10\farcs7 \pm 0\farcs2$ and $\sim$13 from the 3 mm dust continuum image. The velocity field map shows that sources VLA 3 and B are located in the red- and blue-shifted regions, respectively. As discussed above, this velocity gradient is due to the

[6]The coordinate is derived from the nearby object ASR 2, of which the coordinate is referred as 03:29:03.76.0, +31:16:03.94 (J2000). The error bar is dominated by the positional uncertainties of ASR 2.

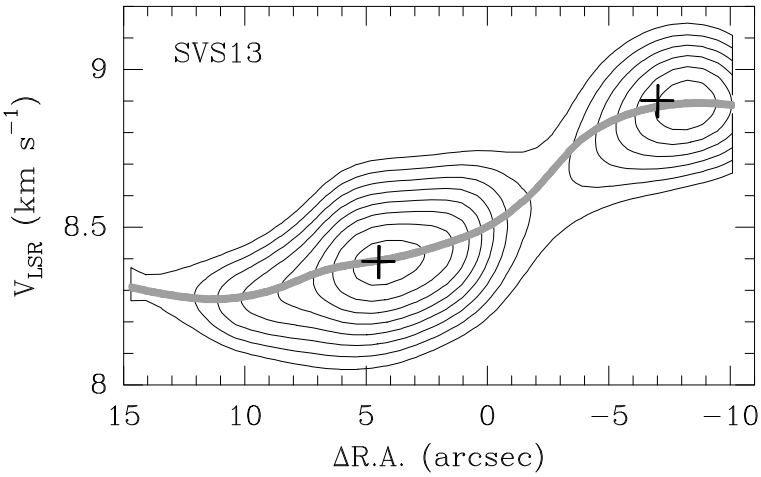

Figure 4.10: Position-velocity diagram of SVS 13 (along the connection line between sources B and VLA 3). Crosses show the locations of sources B and VLA 3. Grey line marks the mean radial velocity.

core rotation, which strongly supports the view that the two dust continuum sources are forming a protobinary system embedded in the N_2H^+ core.

Fig. 4.10 shows the position-velocity diagram along the connection-line between the two sources. The radial velocity difference between the two sources is $\sim 0.5\,\mathrm{km\,s^{-1}}$. Assuming that the two sources are in Keplerian rotation, the velocity difference yields a combined binary mass of $\sim 1.07\,M_\odot$. Assuming a mass ratio of ~ 13 ($M_\mathrm{B}/M_\mathrm{VLA3}$), the derived masses of sources B and VLA 3 are 0.99 and $0.08\,M_\odot$, respectively.

The estimated dynamical mass of source B is well comparable to the total gas mass derived from 1.4 mm dust continuum ($0.97\,M_\odot$) and viral mass derived from N_2H^+ line ($0.91\,M_\odot$). Taking into account the uncertainties in our calculations, we could consider at the first order that the dynamic mass, virial mass, and gas mass derived for source B are equal to each other. This strongly supports our assumption above that both sources B and VLA 3 are forming a physical-bound binary system. Hereafter, we refer this binary protostar as SVS 13 B.

4.4.5 Hierarchical fragmentation in SVS 13

The 3 mm dust continuum image of SVS 13 shows three distinct sources (A, B, and C), which are roughly aligned along a line in the northeast-southwest direction (see Fig. 4.1). Previous single-dish submm and mm maps have shown an elongated (also in northeast-southwest direction) large-scale envelope, with a radius of $\sim$ 20000 AU (0.1 pc), around these three sources (Chini et al. 1997; Chandler & Richer 2000). The separations between sources A-B and B-C are ~ 5000 AU and ~ 7000 AU, respectively. Both separations are larger than the typical Jeans length in prestellar cores (~ 4000 AU; see Chapter 3). Based on these associated morphologies, we suggest that these dust continuum sources (A, B, and C) were formed by initial fragmentation of a large-scale filamentary molecular cloud core.

On the other hand, in the SVS 13 B (sub-)core, a binary protostar, with a separation of 3800 AU (less than the Jeans length), was formed. The velocity field associated with this binary protostar is dominated by rotation and the rotational energy is quantified to be $\beta_{\rm rot} \sim 0.023/sin^2 i$. Although this energy is relatively small in the support of the core, it is believed to play an important role in the fragmentation process (see reviews by Bodenheimer et al. 2000 and Tholine 2002). The simulations in Boss (1999) have shown that rotating cloud cores fragment when $\beta_{\rm rot} > 0.01$ initially (considering magnetic fields support fragmentation)[7]. Based on the morphology and velocity structure, we suggest that the protobinary system in SVS 13 B was formed through rotational fragmentation of a single collapsing protostellar core.

Altogether we suggest a hierarchical fragmentation picture for SVS 13. (1) A large-scale filamentary prestellar core was initially fragmented into three sub-cores (sources A, B, and C) due to slow rotation or turbulence (see a review by Bonnell et al. 2007). (2) These sub-cores are continually contracting toward higher degrees and start separately collapsing; during this phase, the rotation of the sub-cores is getting faster and dominates gas motion. (3) During or immediately after collapse, the single sub-core fragments into a binary protostar (e.g., SVS 13 B) if rotational energy is larger than a certain level (e.g., $\beta_{\rm rot} > 0.01$) or forms a single protostar (e.g., SVS 13 C?) if rotational energy is not enough to trigger the fragmentation.

[7]Machida et al. (2005) suggest that the rotational fragmentation occurs only when $\beta_{\rm rot} \geq 0.04$, considering magnetic fields suppress fragmentation. The derived $\beta_{\rm rot}$ value $0.023/sin^2 i$ matches the Machida et al's criteria when $i < 50°$.

Chapter 5

VLT/NACO deep imaging of young stellar objects

This chapter is based on two papers published by Astronomy & Astrophysics by Chen, Henning, van Boekel, & Grady (2006) and Chen, Launhardt, & Henning (2007), and one paper prepared for Astrophysics & Astronomy by Chen, Launhardt, & Henning (2008).

Abstract

We present high-resolution near-infrared observations of young stellar objects in nearby clouds, using the adaptive optics system NACO at the ESO *Very Large Telescope* (VLT). The main goal of this study is to search for binary systems in the young stellar objects and sample their multiplicity properties. The preliminary results suggest a raw multiplicity rate of $35 \pm 5\%$ with binary separation ranging from 30 AU to 2000 AU. We describe in detail two examples. One is the Class I object GSS 30 IRS1, the other is relatively evolved Class III object HD 100453. In GSS 30 IRS1, VLT/NACO images reveal two separate components with an angular separation of $\sim 0\farcs15$ (~ 24 AU at a distance of 160 pc). The brightness contrasts between the two components are ~ 1.4 mag at H band, 1.5 mag at K_s band, and 2.1 mag at L' band. From two-epoch images, we find a possible orbital motion in GSS 30 IRS1 and estimate a combined dynamical mass of $2.0 \pm 0.5\,M_\odot$ for this system. In HD 100453, we detect a new companion with an angular separation of $\sim 1\farcs06$ (~ 120 AU at a distance of 114 pc) to the primary HD 100453. The brightness contrasts between the two components are ~ 5.1 mag at K_s band and ~ 4.2 mag at Brγ band. Two-epoch images also show a small possible orbital motion in this binary system, through which we estimate a combined dynamical mass of $1.0 \pm 0.2\,M_\odot$. Based on our results, as well as the data in the literature, we derive the distribution of specific orbital angular momentum in the pre-main sequence binary systems. We find that the specific angular momenta of wide pre-main sequence binaries are close to those of the protostellar cores we studied before, suggesting that these wide binary systems could be formed directly through fragmentation of protostellar cores and inherit most angular momentum contained in the collapse region.

5.1 Introduction and sample

In this chapter I present our preliminary results from a systematic search for binary systems among the young stellar objects (YSOs) in nearby clouds, using the adaptive optics system NACO at the ESO *Very Large Telescope* (VLT). For this study I retrieved near-infrared (NIR) imaging data of a number of low-mass sources from the the ESO/ST-ECF Science Archive Facility[1]. Most sources were selected such that they have either Class I or "flat-spectrum" (slightly more evolved than Class I) spectral energy distributions (SEDs), except IRAS 120 in L1641 (Class II) and HD 100453 (Class III). These YSOs represent the direct evolutionary outcomes of the Class 0 protostars that we studied in the former chapters. Therefore, studying these objects at high spatial resolution offers an opportunity to sample an important intermediate stage between protostellar cores and main sequence (MS) stars.

The target list and basic properties of the sources are summarized in Table 5.1. In defining Class I and flat-spectrum (FS) YSOs, the classification scheme of Greene et al. (1994) has been adopted here, i.e., Class I sources have a spectral index $\alpha = d\log(\lambda F_\lambda)/d\log(\lambda) > 0.3$, and flat-spectrum sources have $0.3 > \alpha_{\rm IR} \geq -0.3$ in the wavelength range $2\,\mu{\rm m} \leq \lambda \leq 12\,\mu{\rm m}$. It must be noted that the use of only an IR spectral index to classify YSOs is not the most physical criterion. In particular, Class I YSOs are primarily defined by the fact that they are surrounded by a remnant envelope (Lada 1987). It is likely that some of the targets in this sample do not match this criteria.

5.2 VLT/NACO observations

The sources were observed with NACO (Lenzen et al. 2003; Rousset et al. 2003) at the ESO VLT on Cerro Paranal in Chile between 2003 and 2005. The detector of NACO is an Aladdin InSb 1024 × 1024 pixel array. The cameras used were S13, S27, and L27, which provide pixel scales of 13.25, 27.03, and 27.12 mas pixel^{-1}, respectively. The fields of view of the S13, S27, and L27 cameras are $\sim 14'' \times 14''$, $28'' \times 28''$, and $28'' \times 28''$, respectively.

The observations were mainly carried out in H-band ($1.66\,\mu$m), $K_{\rm s}$-band ($2.18\,\mu$m), and L'-band ($3.80\,\mu$m), respectively (see Table 5.1). The data reduction was carried out using self-developed IDL scripts. After bad-pixel filtering, flat-field correction, and sky removal, the individual dithering positions were combined into a resulting mosaic image.

5.3 A case of Class I object: GSS 30 IRS1

Figure 5.1 shows the VLT/NACO images of the binary/multiple systems resolved in this study. Within 2000 AU of the 34 Class I and FS targets, we have detected a total of 12 binary/multiple systems, of which 8 are new discoveries. A raw multiplicity rate

[1] http://archive.eso.org

Table 5.1: Sample and observation log[a]

Object	Other name	$\alpha_{\rm IR}$	Class	$L_{\rm bol}(L_\odot)$	Ref.[b]	Filters	Obs. Date (UT)
			Taurus (IRAS source)				
04113+2758		-0.01	FS	>1.6	1,2	$HK_{\rm s}L'$	03/12/03
04239+2436		1.27	I	1.3	1,2	$HK_{\rm s}L'$	04/12/03
04263+2426	Haro 6-10	1.02	I	0.74	1,2	$HK_{\rm s}L'$	03/12/03
04287+1801	L1551 IRS5	1.57	I	28	1,2	$HK_{\rm s}L'$	04/12/03
04295+2251	L1536 IRS	0.11	FS	0.6	1,2	$K_{\rm s}L'$	04/12/03
04361+2547	TMR 1	1.27	I	3.7	1,2	$K_{\rm s}L'$	04/12/03
04365+2535	TMC 1A	1.08	I	2.4	1,2	$K_{\rm s}L'$	04/12/03
04385+2550	Haro 6-33	0.14	FS	>0.4	1,2	$HK_{\rm s}L'$	03/12/03
04489+3042		0.18	FS	0.3	1,2	$K_{\rm s}L'$	04/12/03
			Ophiuchus				
Oph 29	GSS 30	1.20	I	21	3,4	$HK_{\rm s}L'$	03/03, 01/06/03, 17/06/04
Oph 51		-0.09	FS	0.71	4,5	$K_{\rm s}L'$	02/06/03
Oph 108	EL 29	0.98	I	26	3,4	$HK_{\rm s}L'$	01/06/03
Oph 132	IRS 4	0.08	FS	5.6	3,4	$K_{\rm s}L'$	02/06/03
Oph 134	WL 6	0.59	I	1.7	3,4	$K_{\rm s}L'$	01/06/03
Oph 141	IRS 43	0.98	I	6.7	3,4	$K_{\rm s}L'$	01/06/03
Oph 147	IRS 47	0.17	FS	3.7	3,4	$HK_{\rm s}L'$	02/06/03
Oph 159	IRS 48	0.18	FS	7.4	3,4	$HK_{\rm s}L'$	01/06/03
Oph 167	IRS 51	-0.04	FS	1.1	3,4	$HK_{\rm s}L'$	01/06/03
Oph 182	IRS 54	1.76	I	6.6	3,4	$K_{\rm s}L'$	02/06/03
Oph 204	L1689 IRS5	-0.25	FS	2.4	4,6	$HK_{\rm s}L'$	02/06/03
			Serpens				
Ser 159		0.11	FS	...	5,7	$HK_{\rm s}L'$	01/06/03
Ser 307	SVS 2	0.06	FS	...	5,7	$HK_{\rm s}L'$	01/06/03
Ser 314	SVS 20	-0.03	FS	...	5,7	$HK_{\rm s}L'$	01/06/03
Ser 347	EC 129	0.06	FS	...	5,7	$HK_{\rm s}L'$	01/06/03
			Orion A (L1641)				
IRAS 29		1.3	I	32	8	$HK_{\rm s}L'$	03/12/03
IRAS 72		0.15	FS	3.2	8,9	$HK_{\rm s}L'$	04/12/03
IRAS 87		0.56	I	10.2	8	$HK_{\rm s}L'$	04/12/03
IRAS 120		-0.43	II	1.5	8,9	$HK_{\rm s}L'$	04/12/03
IRAS 171		-0.05	FS	2.4	8,9	$HK_{\rm s}L'$	03/12/03
IRAS 187	V1791 Ori	0.01	FS	7.5	8,9	$HK_{\rm s}L'$	03/12/03
IRAS 191	DL Ori	0.64	I	8.1	8,9	$HK_{\rm s}L'$	03/12/03
IRAS 224		0.12	FS	1.5	8,9	$HK_{\rm s}L'$	04/12/03
IRAS 237		-0.21	FS	7.3	8	$HK_{\rm s}L'$	04/12/03
IRAS 270		0.47	I	5.4	8	$HK_{\rm s}L'$	03/12/03
HD 100453	SAO 239162	...	III	9.0	10,11	$K_{\rm s}Br\gamma$	02/06/03, 23/05/06

[a]Basic information was adopted from Table 1 in Duchêne et al. (2007)

[b]References: 1) Kenyon & Hartmann (1995); 2) Motte & André (2001); 3) Barsony et al. (1997); 4) Bontemps et al. (2001); 5) 2MASS Point source Catalog; 6) Greene et al. (1994); 7) Kaas et al. (2004); 8) Chen & Tokunaga (1994); 9) Strom et al. (1989); 10) Dominik et al. (2003); 11) Meeus et al. (2002)

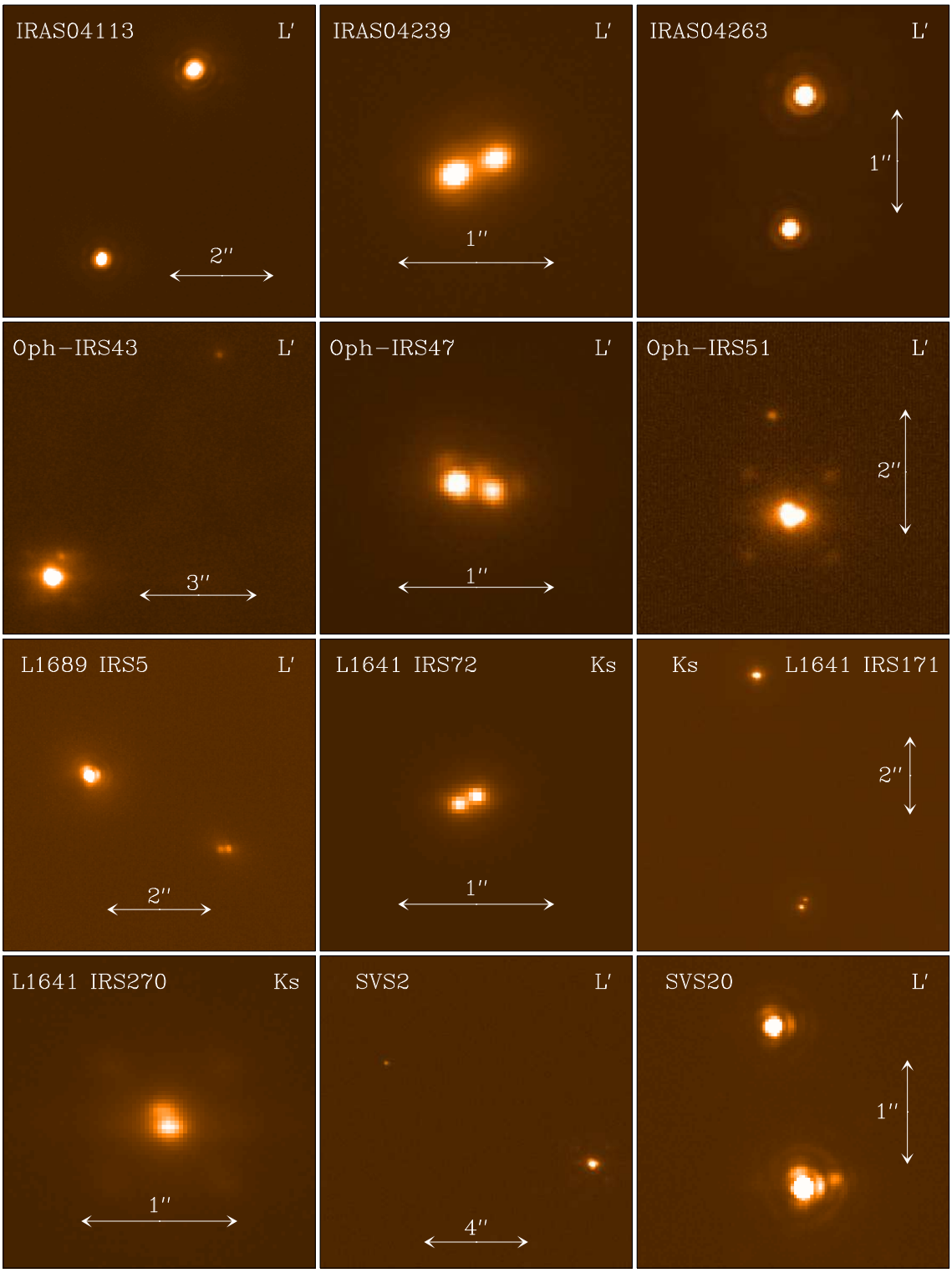

Figure 5.1: VLT/NACO images of binaries at the K_s band (2.166 μm) and the L' band (3.80 μm). North is up, and east is to the left. Scales are marked in each panel.

Table 5.2: NACO observation logs of GSS 30 IRS1 and photometric calibration stars SAO 245532, HD 161743.

Source	Obs. date (UT Date)	NACO Camera	Obs. Band	DIT×N[a] [s]	Seeing [″]	Airmass
IRS1	2003 March 03	S13	K_s	60.0×4	0.81	1.01
IRS1	2003 June 01	S27	H	80.0×4	0.67	1.08
IRS1	2003 June 01	S27	K_s	10.0×4	0.75	1.12
IRS1	2003 June 01	L27	L'	0.175×18	1.00	1.03
SAO 245532	2003 June 01	S27	K_s	0.5×5	1.06	1.34
SAO 245532	2003 June 01	S27	H	0.5×5	0.92	1.33
HD 161743	2003 June 01	L27	L'	0.18×5	1.18	1.04
IRS1	2004 June 17	S13	K_s	20.0×4	0.59	1.35

[a]DIT and N correspond to the exposure integration time and the number of exposures, respectively.

of $35 \pm 5\%$ is estimated from this study. The combined results will be analyzed in a separate paper prepared by Chen, Launhardt, & Henning. In this chapter I focus on two individual examples: one is the Class I object GSS 30 IRS1 (this section), the other is more evolved Class III object HD 100453 (next section).

5.3.1 Introduction of GSS 30 IRS1

GSS 30 IRS1 (hereafter also IRS1) is one of the best-studied YSOs in the ρ Ophiuchus molecular cloud core at a distance of ~ 160 pc. It has been classified as a low-mass Class I object based on its spectral energy distribution (Grasdalen et al. 1973; Elias 1978; Wilking et al. 1989) and bolometric luminosity ($L_{\rm bol} = 21\,L_\odot$; Bontemps et al. 2001). NIR polarimetric studies have shown that IRS1 is surrounded by a large (~ 2000 AU) disk-like envelope and a smaller (~ 150 AU) circumstellar disk, which is inclined $\sim 25°$ away from the plane of the sky (Castelaz et al. 1985; Tamura et al. 1991; Weintraub et al. 1993; Chrysostomou et al. 1996). Strong 1.3 mm dust continuum emission was detected from IRS1 with an integrated flux density of ~ 100 mJy, indicative of a circumstellar mass of $\sim 0.03\,M_\odot$ (André & Montmerle 1994). Zhang et al. (1997) detected a flattened molecular core in $C^{18}O$ and ^{13}CO ($J = 1-0$), in roughly the same orientation as the circumstellar disk. Recently, Pontoppidan et al. (2002) detected bright CO ro-vibrational emission from IRS1, suggesting a strong accretion shock in the inner $10 - 50$ AU of the circumstellar disk. Tamura et al. (1990) reported high velocity CO emission at 115 GHz around IRS1 in a region of roughly $5'$ in extent. However, since both the blue- and red-shifted molecular gas are located to the south of GSS 30, the origin of the molecular outflow could not be identified. In this section I present new NIR observations of GSS 30 IRS1, conducted with VLT/NACO. The observation parameters of GSS 30 IRS1 are summarized in Table 5.2.

5.3.2 Results on GSS 30 IRS1

Figure 5.2a shows the S27/H-band image of IRS1. A bipolar nebulosity is seen around IRS1, with a bright double-wing lobe extending to the northeast and a fainter lobe

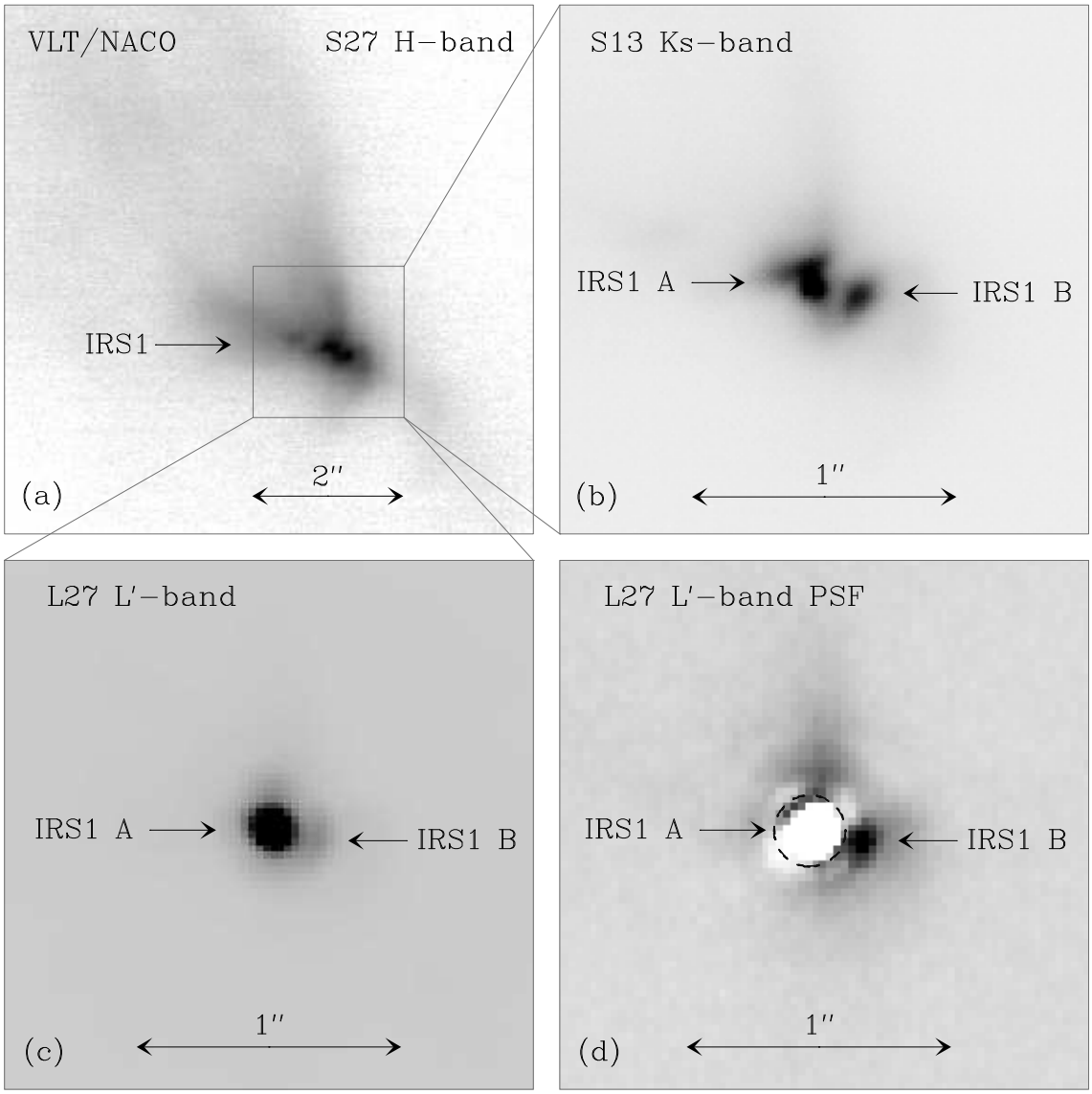

Figure 5.2: (a) VLT/NACO S27 image of GSS 30 IRS1 in the H-band (1.65 μm). (b) 2003 VLT/NACO S13 K_s-band (2.18 μm) image of the inner region around IRS1. The positions of IRS1 A and IRS1 B are indicated with letters A and B, respectively. (c) L27 L'-band (3.80 μm) image of IRS1. (d) L27 L'-band PSF-subtracted image of IRS1. For all the images, north is up and east is to the left. The scales are marked in each map.

Table 5.3: HK_sL' magnitudes and colors of GSS 30 IRS1 A and IRS1 B. Data are from the VLT/NACO S27 camera.

Source	H	K_s	L'	$H-K_s$	K_s-L'
IRS1	10.9 ± 0.1	8.4 ± 0.1	7.84 ± 0.02	2.5 ± 0.2	0.6 ± 0.1
IRS1 A	11.3 ± 0.2	8.7 ± 0.1	7.98 ± 0.02	2.6 ± 0.3	0.7 ± 0.1
IRS1 B	12.7 ± 0.3	10.2 ± 0.2	10.1 ± 0.03	2.5 ± 0.5	0.1 ± 0.2

extending to the southwest. Figure 5.2b shows a higher resolution 2003 S13/K_s-band image of the central part around IRS1. In this image IRS1 is resolved into two objects. In the following, we refer to the brighter eastern object as IRS1 A and to the western object as IRS1 B. Figure 5.2c shows the L27/L'-band image of IRS1. In this image a strong point-like object is seen at the position of IRS1 A, but fainter emission is also detected at the position of IRS1 B. To enhance the contrast on the faint source, we subtracted the PSF from IRS1 A. In this L'-band PSF-subtracted image, a point-like object becomes visible at the position of IRS1 B (see Fig. 5.2d).

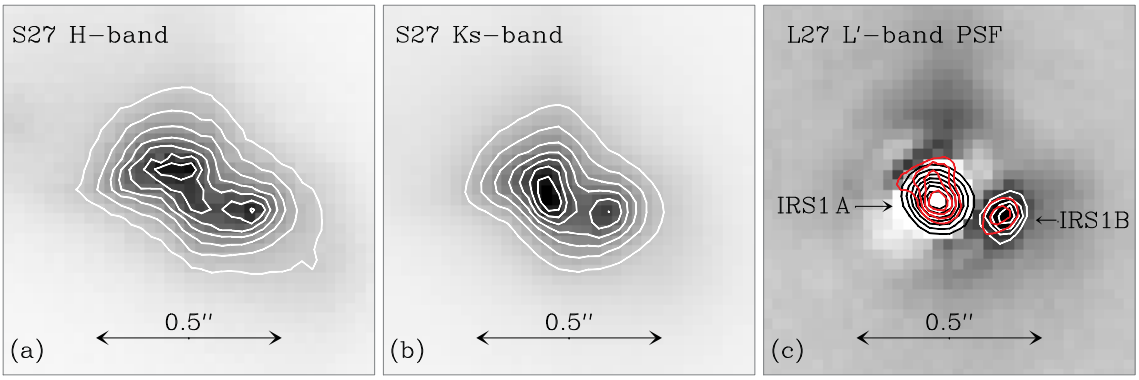

Figure 5.3: a) S27/H-band contour image. Contours start from 30% to 90%, in steps of 10% of the peak intensity. b) Same, but at S27/K_s-band. c) L'-band PSF-subtracted image. Contours (white) are at 60%, 70%, 80%, and 90% of the peak intensity of IRS1 B. The image is overlaid with L27/L'-band contours (black; from 30% to 90%, in steps of 10% of the peak intensity of IRS1 A) and S13/K_s-band contours (red; from 60% to 90%, in steps of 10% of the peak intensity of IRS1 A).

To view the structure in detail, in Fig. 5.3 we show the contour maps of the inner region around GSS 30 IRS1. At all HK_sL' bands, IRS1 is resolved into two objects. However, both IRS1 A and IRS1 B show extended structures at HK_s bands (see Figs. 5.3a and 5.3b). Figure 5.3c shows the contour of the L'-band PSF-subtracted image, overlaid with the contours from Figs. 5.2b and 5.2c. At L' band, both objects show point-like structures. Furthermore, we find that IRS1 A and IRS1 B detected at K_s band are spatially coincident with each L' band source. Nevertheless, there is a small offset ($\sim$ 10 mas) between the peaks of IRS1 B in the S13/K_s-band image and L27/L'-band image (see Fig. 5.3c), which could be due to the differences in resolution and wavelength between the cameras S13 and L27.

The photometry of IRS1 and calibration stars was performed with the GILDAS package. For comparison with earlier papers (e.g., Barsony et al. 1997), we first treat IRS1 as a single source and integrate the flux densities enclosed by the FWHM levels. The integrated flux densities are then converted into magnitudes by applying the same method to the standard stars (see Table 5.3). The derived magnitudes of "IRS1" compare well with the results in Weintraub et al. (1993) and Barsony et al. (1997). In order to obtain the magnitudes of IRS1 A and IRS1 B, a number of assumptions have to be made because of their extended structures and strong scattering in nearby nebulosity. At HK_s bands, we integrate the flux densities enclosed by the 80% level (H band) and 70% level (K_s band) of the peak intensities (where the two objects are separated; see Fig. 5.3) and then estimate flux ratios between the two objects. By combining "IRS1" magnitudes and the flux ratios, we derive individual magnitudes of IRS1 A and IRS B. At L' band, the magnitude of IRS1 B was calculated from the integrated flux density enclosed by the FWHM level in the PSF-subtracted image. The derived HK_sL' magnitudes, uncertainties, and colors of IRS1 A and IRS1 B, are listed in Table 5.3. The brightness contrasts between IRS1 A and IRS1 B are 1.4 mag at H band, 1.5 mag at K_s bands[2], and 2.1 mag at L' band, indicating that IRS1 A is "redder" than IRS1 B. However, it must be noted that large uncertainties exist in this photometry and the results can be referred only for qualitative analysis.

5.3.3 Discussion for GSS 30 IRS1

5.3.3.1 GSS 30 IRS1: a binary system?

In general, Class I YSOs are still embedded in their remnant envelope, which produces large scattered light nebulosity and makes the interpretation of the NIR maps very complicated. In the case of GSS 30 IRS1, the northeast double-wing lobe has long been suggested as scattered light from the wall of a cavity evacuated by the molecular outflow, while the fainter southwest lobe is proposed to be obscured by a tilted circumstellar disk (Castelaz et al. 1985; Tamura et al. 1991; Weintraub et al. 1993; Chrysostomou et al. 1996).

Taking into account this outflow-disk complex, the two objects detected in IRS1 may represent two scattered light peaks from two dust clumps located on the outer wall of the outflow cavity. These two dust clumps could be separated by an optically thick ridge of dense material in the disk. This is a well-known effect from optically thick circumstellar disks observed close to edge-on (see e.g., Wolf et al. 2003b). Although a simple disk structure seems unlikely to account for the observations of GSS 30 IRS1, a similar behavior related to a partially optically thick nebula could not be ruled out here.

Another possibility is that IRS1 A and IRS1 B represent two YSOs and compose a binary system embedded in a common disk. Indeed, the good agreement between the S13/K_s-band image and L27/L'-band image (see Fig. 5.3c) suggests that the two objects represent actual stars rather than scattered light structures. However, in contrast to the point-like structures seen at L' band, both objects show extended structures

[2]In the deeper image observed by S13 camera, the brightness contrast is ~ 1.0 mag at K_s band.

at HK_s bands (especially at H band), which makes us still doubt their stellar qualifications. Unfortunately, the three-band NIR observations acquired so far are not sufficient to determine the natures of the two objects. Since the 1.3 mm continuum observations suggest a great deal of circumstellar dust around IRS1 (André & Montmerle 1994), we speculate that this extended structure is due to the dust scattering in a small cocoon/halo (or even circumstellar disk) surrounding each component, the tidal truncation causing it to be non-spherical (see Lubow & Artymowicz 2000). At L' band, the dust opacity (scattering) is greatly reduced; here, the point-like structure of two objects is revealed.

Assuming that IRS1 is a binary system, the angular separation and position angle (with respect to IRS1 A) were measured to be 154.4 ± 5 mas and $256\overset{\circ}{.}5 \pm 0\overset{\circ}{.}5$ in the 2003 S13/K_s-band image, respectively. The angular separation corresponds to a linear projected separation of ~ 24 AU at a distance of 160 pc. Due to this small separation, IRS1 A and IRS1 B remained unresolved in previous binary surveys of the ρ Ophiuchi molecular cloud (see Haisch et al. 2002; Duchêne et al. 2004).

5.3.3.2 Orbital motion in GSS 30 IRS1?

Figure 5.4 shows the 2003 and 2004 two-epoch S13/K_s-band images of GSS 30 IRS1. The comparison shows a small shift of IRS1 B (see Fig. 5.4). The observed changes in separation (~ 10 mas) and position angle ($\sim 3^\circ$) suggest that IRS1 B is rotating clockwise around IRS1 A[3]. However, the uncertainties in the measurements are of the same order as the change of position, therefore the result does not provide strong evidence for the physical bound. Furthermore, two-epoch images are not sufficient to derive orbital parameters. Before we can state that the newly discovered two objects in IRS1 are really forming a binary system, at least one more epoch image is needed to confirm the detection of orbital motion and at least four more epochs images are needed to derive orbital parameters.

Nevertheless, assuming that the short shift is due to the orbital motion in the binary system, some tentative conclusions still could be derived. From this shift, we infer a relative proper motion of 8.6 ± 3.0 mas yr^{-1}, implying a relative velocity of 4.9 $\pm$ 1.8 km s^{-1} in the plane of the sky. According to the Keplerian motion and taking into account an inclination $\sim 25^\circ$ (assuming the orbit has the same inclination as the large circumbinary disk), we obtain a total mass of $M \sim 2.0 \pm 0.5\, M_\odot$ and a period of ~ 90 yr for this binary system.

On the other hand, stellar masses could also be estimated through a comparison between the photometry and theoretical evolutionary tracks (e.g., Gehz et al. 1997). The bolometric luminosity of IRS1 was estimated to be $21\, L_\odot$ (Bontemps et al. 2001). From the brightness contrasts between IRS1 A and IRS1 B, we infer a flux ratio of 10:1 for the two objects. Taking an age of $1 - 3 \times 10^5$ yr for IRS1 (a typical age of Class I YSOs; see Shu et al. 1987), the comparison to the evolution tracks of D'antona & Mazzitelli (1994) shows that the masses of IRS1 A and IRS1 B are $1.3 - 1.6\, M_\odot$ and

[3]The separation and position angle measured in 2004 S13/K_s-band image are 146 ± 6 mas and $254^\circ \pm 1^\circ$, respectively. For angular orientation we used the detector column as reference. The repeatability of the detector orientation on the sky between different observing epochs is better than $0\overset{\circ}{.}01$ (R. Lenzen, private communication).

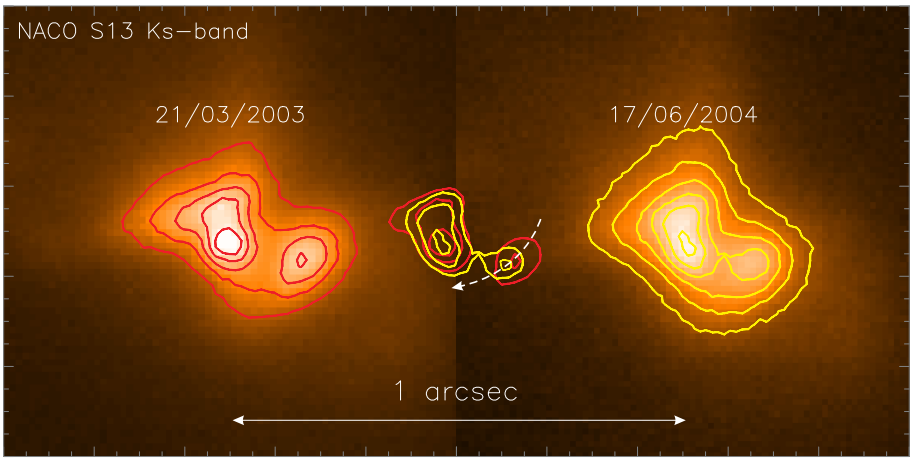

Figure 5.4: Comparison between the 2003 (left) and 2004 (right) NACO S13/K_s-band data. The contours in both map start from 30% of the peak intensity by the step of 10%. The contours in the middle are overlayed by two-epoch data and have been clipped to only show the positions of IRS1 A and IRS1 B. A small shift by IRS1 B is evident in the comparison. A possible inclined trajectroy for the shift of IRS1 B is also suggested.

$0.3 - 0.4\,M_\odot$, respectively. The estimated total binary mass is consistent with the mass derived from the "orbital" motion.

5.4 A case of Class III object: HD 100453

5.4.1 Introduction of HD 100453

HD 100453 (IRAS 11307−5402 or SAO 239162) is an isolated Herbig Ae star of spectral type A9Ve (Malfait et al. 1998). *Hipparcos* measurements give a parallax of 8.97 ± 0.76 mas for HD 100453, from which a distance of 114^{+11}_{-9} pc is derived. The luminosity and mass of HD 100453 were estimated to be $\sim 9\,L_\odot$ and $\sim 1.7\,M_\odot$, respectively (Dominik et al. 2003). The age of HD 100453 is estimated to be ≥ 10 Myr by Meeus et al. (2002). Assuming that HD 100453 is one of the members of the Lower Centaurus Crux association (Kouwenhoven et al. 2005), the upper limit for the age of HD 100453 could be ~ 20 Myr (Mamajek et al. 2002).

The strong infrared excess in the SED of HD 100453 implies the presence of circumstellar dust which is believed to be located in a circumstellar disk (Meeus et al. 2001, 2002; Dominik et al. 2003). According to the classification of Meeus et al. (2001), HD 100453 is the so-called group Ib source, i.e., it has an SED that can be fitted with a power-law plus a black-body continuum, but does not show silicate emission bands shortward of 30 μm. On the other hand, moderately strong PAH bands are present at 3.3, 6.2, 7.7 and 11.2 μm in the mid-IR spectrum of HD 100453 (Meeus et al. 2001). Both Meeus et al. (2002) and Dominik et al. (2003) suggested that the lack of the silicate feature is due to predominating large grains in the circumstellar disk of HD 100453. This viewpoint is supported by the ISO-SWS spectrum of HD 100453. As shown in

Table 5.4: NACO observation logs of HD 100453 and No.9144

Source	Obs. date [UT date]	Central wavelength [μm]	Bandwidth [μm]	DIT [s]	NDIT	Seeing [$''$]	airmass
HD 100453	2003 June 02	2.18	0.35	2.0	2	0.9	1.153
HD 100453	2003 June 02	2.166	0.023	0.35	10	0.9	1.153
No.9144	2003 June 01	2.18	0.35	0.5	5	0.9	1.064
HD 100453	2005 May 23	2.166	0.023	1.0	10	0.5	1.165

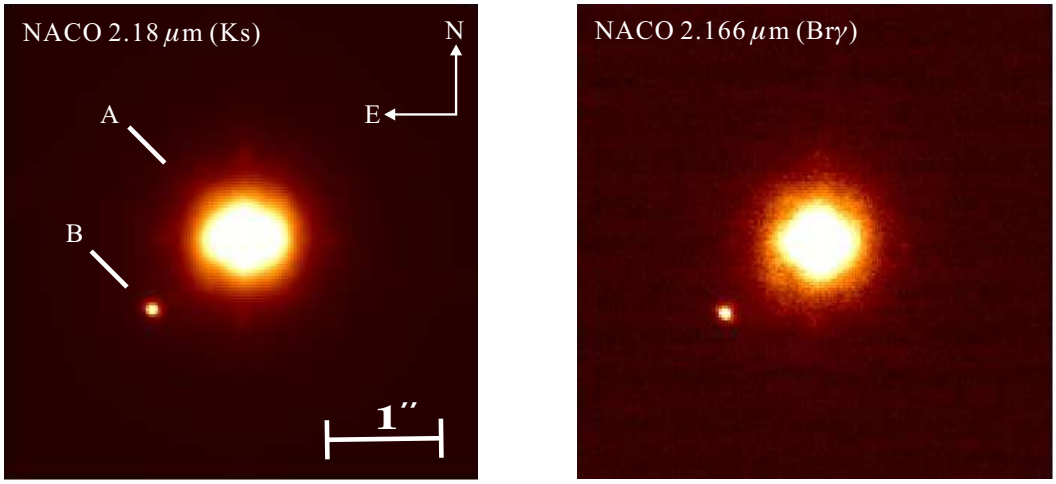

Figure 5.5: The 2003 VLT/NACO AO images of HD 100453 in the K_s band (2.18 μm) and the Brγ band (2.166 μm). North is up, and east is to the left. The positions of HD 100453A and HD 100453B are indicated with letters A and B. The scale is marked in the K_s band image.

Vandenbussche et al. (2004), there is a tentative detection of an emission in the 34 μm band, which can be attributed to crystalline forsterite grains with a size of $\sim 2\,\mu$m. In this section I present two-epoch high-resolution NIR observations of HD 100453. The observation parameters of HD 100453 are summarized in Table 5.4.

5.4.2 Results on HD 100453

Figure 5.5 shows the 2003 K_s-band and Brγ-band images of HD 100453. The main result of the observations is the detection of a previously unknown source to the south-east of HD 100453. Hereafter, we refer this unknown source as HD 100453B, and refer HD 100453 itself as HD 100453A. With respect to HD 100453A, we derive from 2003 K_s-band image a position angle of $127.^\circ3 \pm 1^\circ$ and a separation of $1''.06 \pm 0''.02$ (projected linear separation = 120 ± 2 AU at the distance of 114 pc) for HD 100453B. The positional error given here is dominated by the centering uncertainties of HD 100453B (around 0.5 pixels).

Aperture photometry of HD 100453B and the calibration star No.9144 ($K_s = 11.28$ mag; Persson et al. 1998) was performed with the IRAF/APPHOT package. The photometric apertures of HD 100453B and the calibrator were set to 10 pixels ($0\farcs27$, $\simeq 2.8$ FWHM), in which most of the flux of HD 100453B was recovered. Accurate photometry of HD 100453B suffers from the additional background flux caused by HD 100453A. In order to reduce this effect, we integrated the background flux in the annulus between 49 pixels and 29 pixels with HD 100453A at the center (excluding the flux from HD 100453B), and derived the flux scale in this annulus, assuming circularly symmetric emission from HD 100453A. Then we calculated the background flux in the photometric aperture of HD 100453B and subtracted this background flux from HD 100453B. On the basis of the aperture photometry and error estimates, we derived a magnitude of 10.7 ± 0.1 mag for HD 100453B in the K_s band. Therefore, the brightness contrast between HD 100453A and HD 100453B is 5.1 mag in the K_s band (the magnitude of HD 100453A is 5.60 ± 0.021 mag, which is taken from the 2MASS Point Source Catalog[4]). Due to the high brightness contrast between primary and secondary, HD 100453B was below the detection limit of the near-infrared survey of Kouwenhoven et al. (2005) by roughly one magnitude, and thus remained undetected by these authors. The brightness contrast at Brγ band is measured to be ~ 4.2 mag, which is about one magnitude smaller than that at K_s. The photometric apertures of HD 100453A and B at Brγ were also set to 10 pixels, close to the PSF FWHM of both sources. We also subtracted the background contribution from the flux of HD 100453B at Brγ.

5.4.3 Discussion for HD 100453

The proximity of HD 100453B to HD 100453A suggests that HD 100453B is a physical companion to HD 100453A. HD 100453 is an isolated Herbig Ae star. In a region within a radius of $5'$ centered at HD 100453A, there are only seven stars brighter than HD 100453B ($K_s = 10.66$ mag) in the K band (see Cutri et al. 2003). In analogy to earlier binary surveys, we would consider any bright star closer than $2\farcs0$ to the primary as a companion. Therefore, the probability for a bright field star to be considered as a companion by chance is less than $[7/(5 \times 60)^2\pi] \times 2.0^2\pi = 3.0 \times 10^{-4}$. On the other hand, it is already known that the binary frequency among HAEBE stars is very high, approximately 40% (see Bouvier & Corporon 2001). This supports the view that HD 100453B is a physical companion to HD 100453A.

The second epoch Brγ image taken in 2006 provides further evidence for the physical bound. From the *Hipparcos* catalog (Perryman et al. 1997), the average annual proper motion of HD 100453 is estimated to be $\sim 37.3\,\mathrm{mas\,yr^{-1}}$. Therefore, if HD 100453B is an unrelated field star, the relative separation between the two sources should be changed by an amount of $0\farcs1$ over 3 years, a clearly detectable shift in the VLT/NACO images. However, the comparison between the two-epoch images (see Fig. 5.6) does not find such a large shift but instead shows a small movement of HD 100453B. In Fig. 5.7 we show the scheme of this movement, compared with the proper motion of HD 100453A. The comparison suggests that HD 100453B is rotating anti-clockwise around HD 100453A. From this small movement, we derive a relative motion of $6.7 \pm 2.0\,\mathrm{mas\,yr^{-1}}$, implying a

[4]http://vizier.cfa.harvard.edu/viz-bin/VizieR?-source=II/246

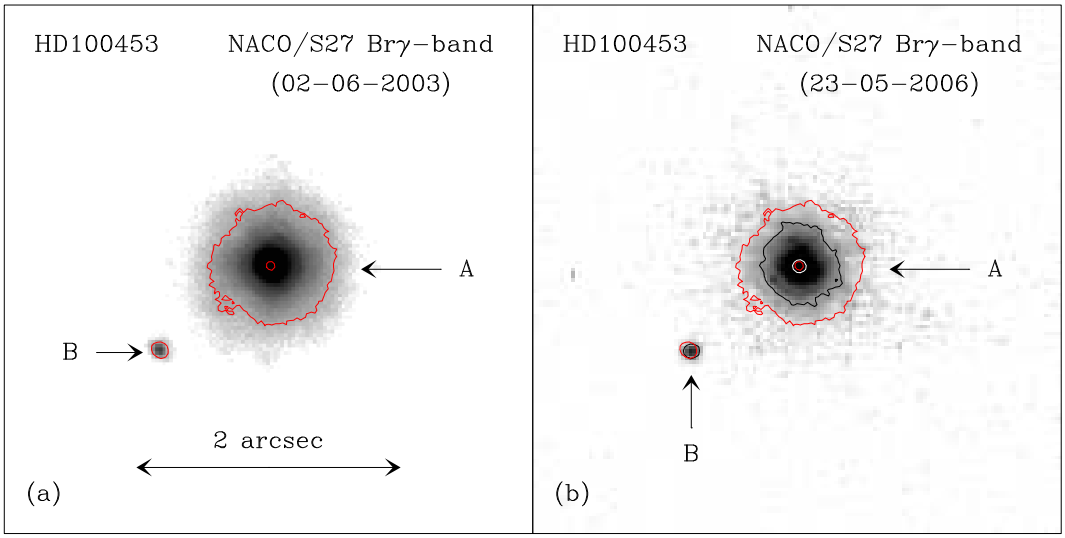

Figure 5.6: Comparison between the 2003 (left) and 2006 (right) NACO S27/Brγ images. The positions of HD 100453A and HD 100453B are indicated with letters A and B. The scale is marked in the 2003 image. The 2006 Brγ image was taken from Collins et al. (in prep.).

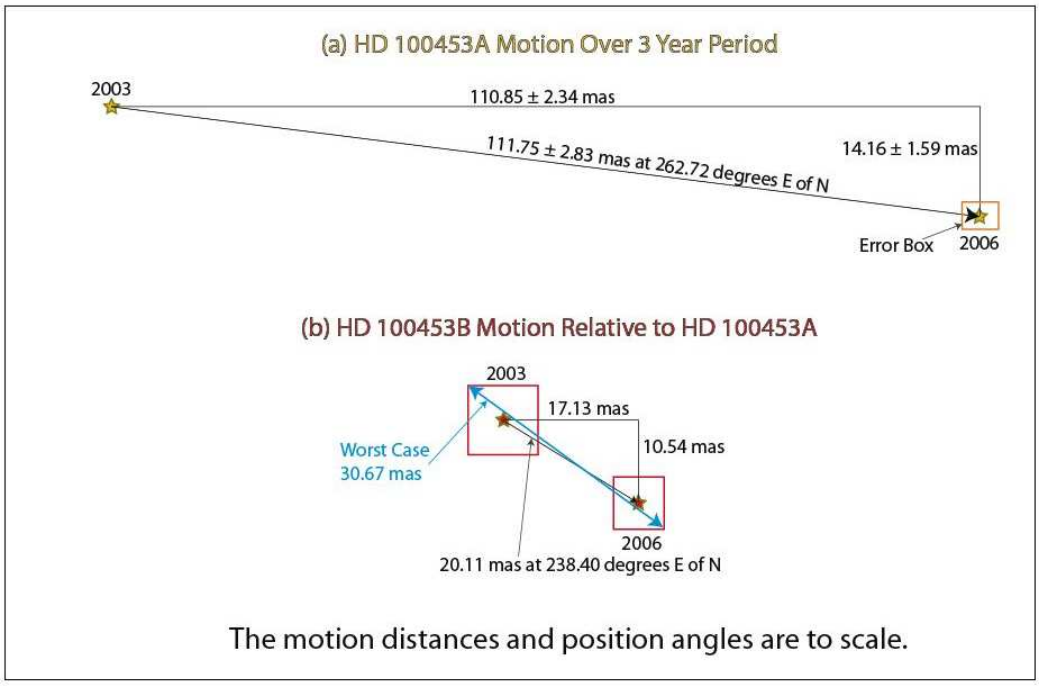

Figure 5.7: (a) The proper motion of HD 100453A over 3 year period. (b) The relative motion of HD 100453B, respecting to HD 100453A. The scheme was provided by K. Collins (private communication).

Table 5.5: Specific orbital angular momenta of PMS binary systems

Source	Class	Separation [AU]	$M_{\rm B}$ [$M_\odot$]	q [M_2/M_1]	J/M [$\times 10^{15}\,{\rm m^2\,s^{-1}}$]	Reference
GSS 30 IRS1*	I	24	2.0	0.3	5.48	This work
L 1527	I	25	0.52	0.7	3.89	Rodríguez (2004)
L 1551 IRS5	I	40	1.2	0.4	6.30	Rodríguez (2004)
YLW 15	I	72	1.7	0.5	10.96	Curiel et al. (2004)
GG Tau	II	11.6	3.34	0.22	4.08	Duchêne et al. (2006)
UZ Tau E	II	41	1.31	0.28	5.58	Prato et al. (2002)
UY Aur	II	165	1.6	0.6	16.97	Close et al. (1998)
HD 98800 B	III	1	1.28	0.82	1.25	Boden et al. (2005)
NTTS 045251	III	5	2.26	0.56	3.45	Zinnecker & Correia (2004)
HD 100453*	III	120	1.0	0.4	9.96	This work

*These values are very uncertain.

relative velocity of $\sim 3.6\,{\rm km\,s^{-1}}$ in the plane of the sky. Assuming to Keplerian rotation, we estimate a lower limit to the total mass of the system to be $1.0 \pm 0.2\,M_\odot$. However, large uncertainty exists in our estimation due to the limitation of the two-epoch observations. On the other hand, if we assume the age of HD 100453B as $10 - 20\,{\rm Myr}$, a simple comparison to the evolutionary tracks of Baraffe et al. (1998) shows that the $K_{\rm s}$ magnitude of HD 100453B is in agreement with the predicted magnitudes of a star of $0.25 - 0.35\ M_\odot$. The corresponding mass ratio between HD 100453B and HD 100453A is therefore $\sim 0.4 \pm 0.1$.

5.5 Distribution of specific angular momentum in PMS binary systems

The specific orbital angular momentum of a binary system is calculated by,

$$J_{\rm binary} = \sqrt{GM_{\rm B}D} \times \frac{q}{(1+q)^2} \tag{5.1}$$

where $M_{\rm B}$, D, and q are total binary mass, separation, and mass ratio (M_2/M_1), respectively. Clearly, in order to derive specific angular momentum of binary systems, we have to derive accurate binary mass, mass ratio and separation in advance. In general, there are two ways to derive masses of binary systems: (1) radial-velocity observation, and (2) multiple-epoch imaging. The former method is most favorable for close (spectroscopic) binary systems, which has been performed over decades for MS field stars (see e.g., Duquennoy & Mayor 1991) and for very low mass ($< 0.1\,M_\odot$) binary systems (see a review by Burgasser et al. 2007). For relatively wide PMS binary systems, multiple-epoch imaging to constrain orbital motion and hence dynamical mass is the usual method used. However, due to large efforts and observing times required by this method, the numbers observed are still very small. Table 5.5 lists a few PMS binary systems, of which the dynamical masses were already studied. We find that the specific angular momenta of these PMS binaries (especially wide systems) are close to those of the protostellar cores we studied before (see Fig. 2.13 or Fig. 6.4), suggesting that

these binary systems could be formed directly through fragmentation of protostellar cores and inherit most angular momentum contained in the collapse region.

Chapter 6

Discussion: new constrains on binary star formation models

This chapter is based on a summary paper prepared by Chen, Launhardt, & Henning et al.

Within this thesis, in total thirteen protostellar cores have been observed at three different millimeter (mm) interferometric arrays (9 at OVRO, 2 at ATCA, and 2 at IRAM-PdBI[1]). The observations were mainly conducted at mm dust continuum and in the N_2H^+ (1–0) molecular line. Figure 6.1 shows the mm dust continuum images of six binary protostars observed within this thesis, in which IRAS 02382 and L723 are two newly-discovered binary protostars. From the mm dust continuum images, we derive the circumstellar mass distribution, separations, and mass ratios. Figure 6.2 shows the radial velocity fields of two binary protostars and their envelopes, derived from N_2H^+ line observations. From the velocity fields, we derive the kinematic properties of the protostellar cores, such as the velocity gradients and the distribution of specific angular momentum.

Although the number observed is still small, we can already draw some important preliminary conclusions based on these results. In this chapter, I discuss new observational constraints, derived from this thesis work, on the binary star formation models.

6.1 How common is binarity in the protostellar phase?

Binarity/multiplicity is frequent in the protostellar phase. All separations accessible to current mm interferometers have been observed (see Table 6.1). Based on our OVRO survey (see Chapter 2), as well as our earlier single-dish (sub)mm dust continuum survey (Launhardt et al. in prep.), we estimate a binary fraction of $> 40\%$ with separation ranging from 500 AU to 10,000 AU. However, due to the small numbers and the limited angular resolution, it is still too early to derive a statistical binary fraction and separation distribution.

[1]Two more objects (L1448C and L1448 IRS2) are in observing at IRAM-PdBI.

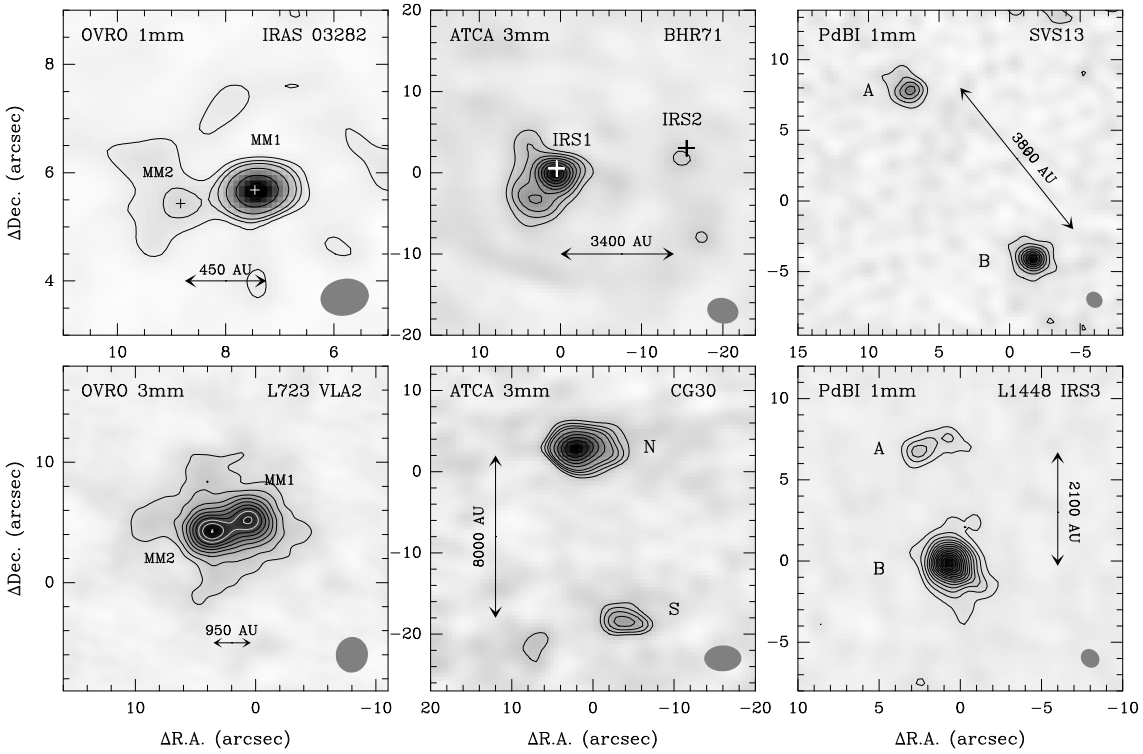

Figure 6.1: Interferometric mm continuum maps of six binary protostars taken at three different interferometers within the course of our program.

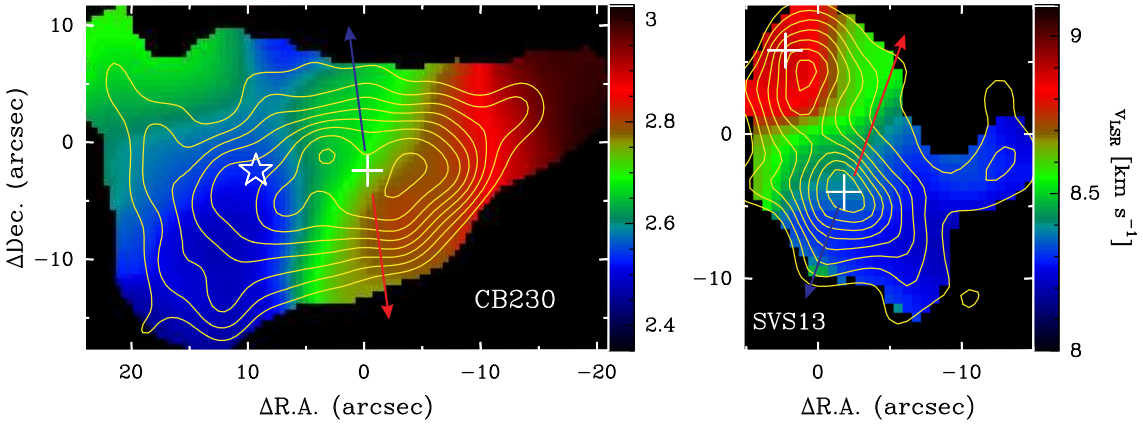

Figure 6.2: N_2H^+ velocity field maps of two binary protostars. Crosses represent the peaks of the mm dust continuum emission. The asterisk in CB 230 marks the position of the secondary protostar observed at 7 μm with ISOCAM (not detected at 3 mm). Red and blue arrows show the directions of of the molecular outflows.

6.2 How is mass distributed in binary star formation?

Table 6.1: Separation and circumstellar mass ratio of known protobinary systems

Source	Class	Sep. [AU]	M_2/M_1	Reference
L1551 IRS5	0/I	50	0.4	Looney et al. 1997
SVS 13A (VLA4A, 4B)	0/I	100	0.37	Anglada et al. 2004
VLA1623	0	180	1.0	Looney et al. 2000
L1551-NE	0	230	0.4	Moriarty-Schieven et al. 2000
IRAS03282+3035	0	450	0.2	This work
NGC1333 IRAS4 A	0	600	0.25	Looney et al. 2000
IRAS16293−2422	0	820	0.8	Mundy et al. 1992
L723 VLA2	0	920	0.8	This work
L1448 IRS3	0	2400	0.18	Looney et al. 2000; this work
BHR71 IRS	0/I	3400	0.1*	This work
NGC1333 IRAS4 B/C	0	3720	0.27	Looney et al. 2000
CB 230	0/I	3800	0.1	Launhardt 2001
SVS 13 B (B, VLA3)	0	3750	0.1*	This work
CG 30 (BHR 12)	0	8700	0.38	This work

* These values are very uncertain guesses.

Although we had derived the masses of circumstellar envelope and disk from the mm dust continuum images, these 'absolute' masses are very uncertain and often cannot be compared because different observing (e.g., sensitivity, angular resolution, and uv coverage) and analysis methods trace different amounts of material. Relative masses are more reliable although they are often just scaled with the flux density without detailed modeling of the temperature structure which might be different for different protostar masses, accretion rates, and disk sizes.

We list in Table 6.1 (updated from Table 1 in Launhardt 2004) most known binary protostars and their circumstellar mass ratios, under the assumption that the mass is proportional to the mm flux density. It must be noted that the circumstellar mass ratio does not necessarily reflect the mass ratio of the hydrostatic cores nor that of the final stars. Figure 6.3 shows the distribution of circumstellar mass ratios in these protobinary systems. The distribution appears to be flat like that of more evolved long-period MS binary stars. We find that more than 75% of protobinary systems have circumstellar mass ratios below 0.5, i.e., unequal masses are much more common than equal masses. Since equal-mass systems are relatively easier to detect in the observations, this distribution indicates a real trend that **unequal-mass systems are preferred in the process of binary star formation.**

6.3 How is angular momentum distributed?

Figure 6.4 shows the distribution of specific angular momentum versus size scale for all protostellar cores studied in this thesis (Chapters 2−4), together with the PMS binary systems (Chapter 5), using the same way as described in Fig. 2.13. The distribution

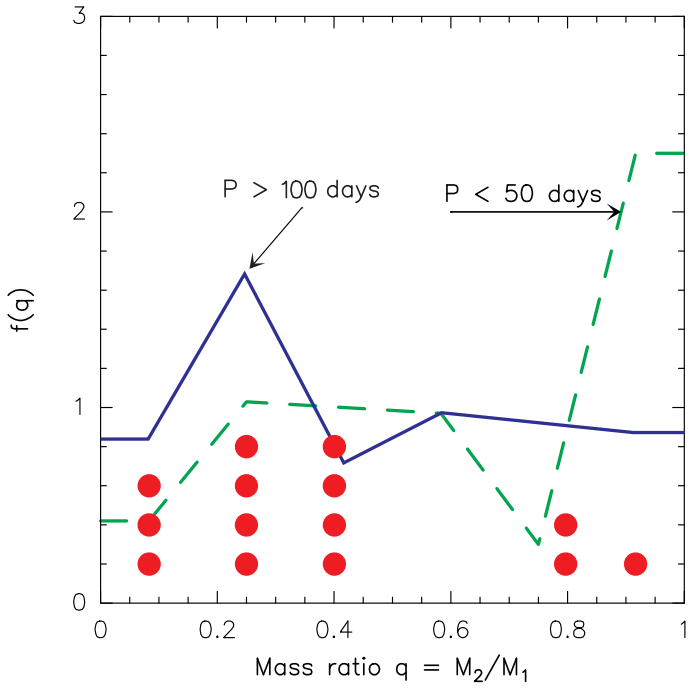

Figure 6.3: Distribution of circumstellar mass ratios in protobinary systems (red dots). Color lines show the distribution of mass ratios in MS binary systems (Halbwachs et al. 2003).

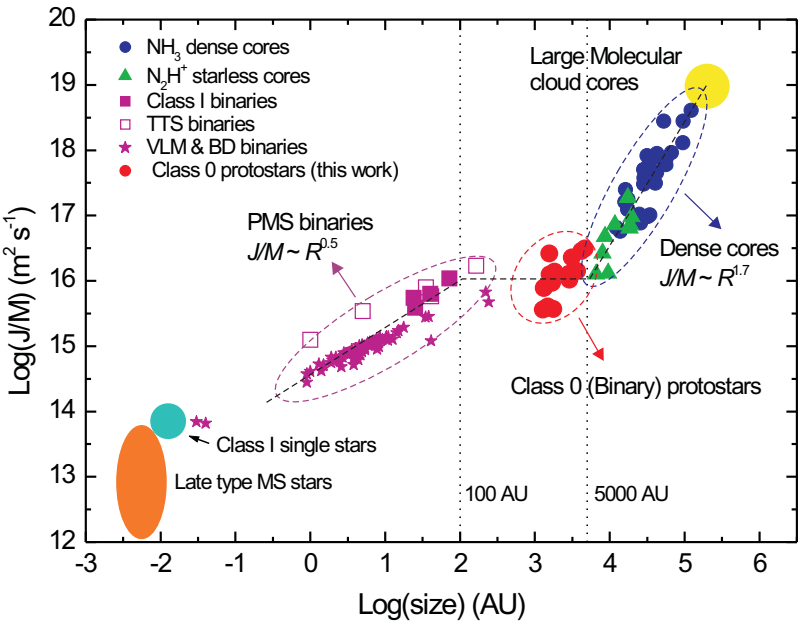

Figure 6.4: Distribution of specific angular momentum J/M versus size R of molecular cloud cores, protostars, and stars. For details see caption in Fig. 2.13.

confirms our result found in Chapter 2 that the specific angular momenta of Class 0 protostellar cores are intermediate between those of prestellar cores and the orbital angular momenta of wide PMS binary systems and there is no significant decrease of angular momentum between the onset of the protostellar collapse and the emergence of a binary star. This result indicates that **most of the angular momentum contained in the collapse region is transformed into orbital angular momentum of the resulting stellar binary system.**

If we assume that most binary protostars in our research are bound systems (e.g., SVS 13 B), the specific orbital angular momenta of primary (J_1) and secondary (J_2) can be calculated by following equations, respectively,

$$J_1 = \sqrt{GM_{\rm B}D} \times \frac{q^2}{(1+q)^2} \tag{6.1}$$

$$J_2 = \sqrt{GM_{\rm B}D} \times \frac{1}{(1+q)^2} \tag{6.2}$$

where $M_{\rm B}$, D, and q are total binary mass, separation, and mass ratio (M_2/M_1), respectively. As discussed above, most binary protostars actually consist of unequal masses components, which means that the amounts of their specific angular momentum are also unequal, i.e., most of specific angular momentum contained in the prestellar core is inherited by the secondary during the fragmentation (while most of mass is inherited by the primary). Furthermore, we find in many protobinary systems that the outflows and hence the angular momenta of the components are not aligned, like e.g., CB 230 and L723 (Chapter 2), CG 30 and BHR 71 (Chapter 3). These results indicate that **during core fragmentation the initial angular momentum is not evenly, in value and direction, transformed into the binary components.**

6.4 Which factor dominates the fragmentation?

In order to study which physical processes are most important for the fragmentation of a molecular cloud core, we have derived the energy balance for our sample based on the N_2H^+ observations. In general, rotation and turbulence are the two main mechanisms that have been considered to provide the angular momentum required for fragmentation. We therefore show in Fig. 6.5 the distributions of $\triangle v_{\rm NT}$ and $\beta_{\rm turb}$ versus core size R, and in Fig. 6.6 the distribution of $\beta_{\rm rot}$ versus core size.

As we already mentioned in former chapters, high-level (supersonic) turbulence normally occurs in large-scale cores only, while the inner parts of cores are "velocity coherent" and characterized by low-level (subsonic) turbulence (Fig. 6.5a). The distribution of $\beta_{\rm turb}$ v.s. R in Fig. 6.5b is somewhat scattered and shows no correlation between turbulence level and fragmentation. This means that turbulence works mainly before gravitationally bound prestellar cores form and no longer plays an important role on the small scales, i.e., in (pre-)protostellar cores.

On the other hand, we find that most cores with binary protostars have ratios of rotational to potential gravitational energy of $\beta_{\rm rot} > 1\%$ (see Figure 6.6b)[2]. This

[2]The derived $\beta_{\rm rot}$ values were originated from $\beta_{\rm rot}/sin^2 i$, where we assume $sin^2 i = 1$ for all objects.

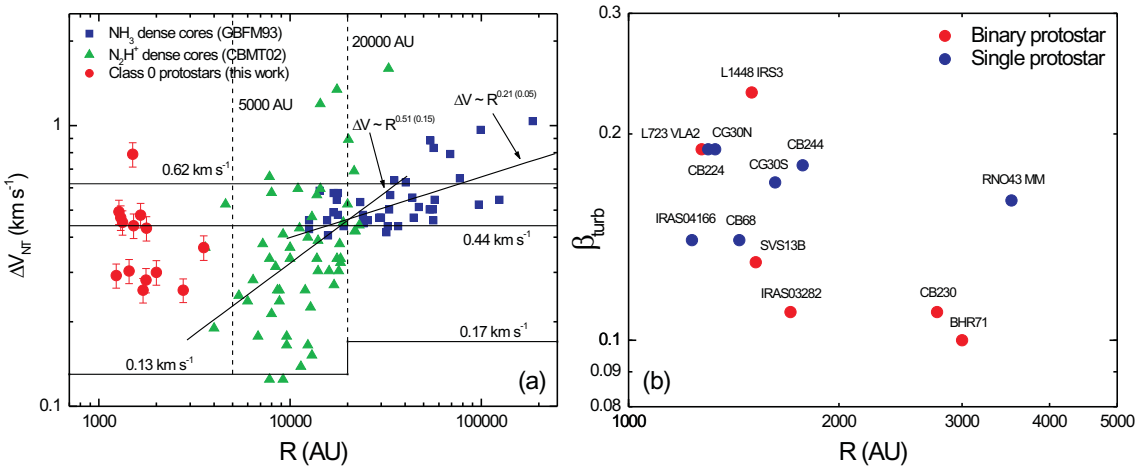

Figure 6.5: (a) Non-thermal line width $\triangle V_{NT}$ versus size R of dense molecular cloud cores. For details see Fig. 2.11 in Chapter 2. (b) Ratio of turbulent to gravitational energy β_{turb} versus size R for protostellar cores.

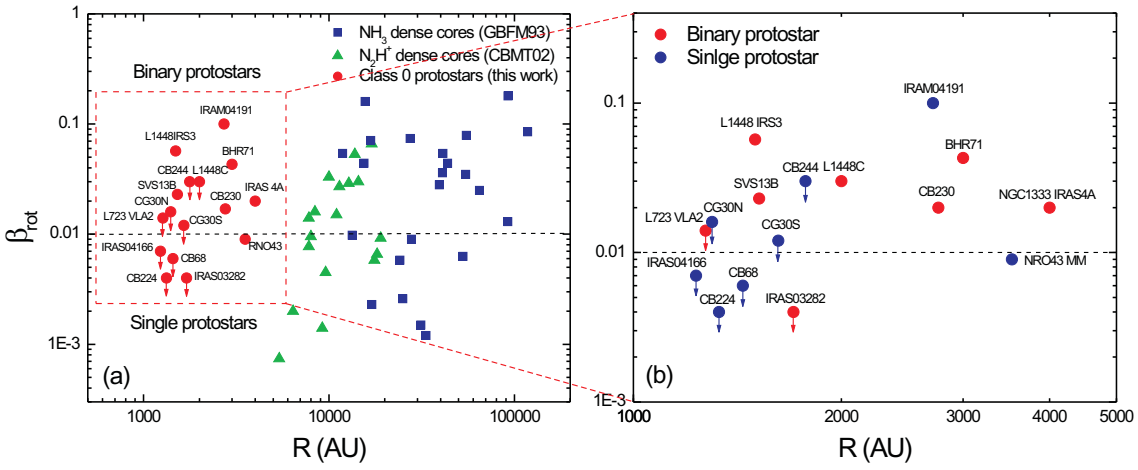

Figure 6.6: (a) Ratio of rotational to gravitational energy β_{rot} versus size R. For details see Fig. 2.14 in Chapter 2. (b) Same, but enlarged view for protostellar cores.

is consistent with theoretical simulations (see reviews by Bodenheimer et al. 2000) and suggests that the **initial amount of rotational energy in a molecular cloud core is playing an important role in the protostellar fragmentation process.** However, due to the small numbers, the conclusion is not statistically significant.

6.5 Why quadrupolar outflow is so rare?

Assuming that binarity among protostars occurs as frequent as among pre-main sequence stars, one would expect to find many multiple (quadrupolar) protostellar outflows. However, such kind of outflows have been observed only in a handful of sources. As our knowledge, so far there are only two low-mass protostars associated with quadrupolar outflows: one is L 723 (see Chapter 2), the other is IRAS 16293–2422 (Walker et al. 1988; Mizuno et al. 1990).

We speculate three reasons to explain this puzzle: (1) outflow-envelope interactions make the interpretation of outflow maps very complicated and no clear morphologies can been identified; (2) if the circumstellar disks of sub-cores are aligned, they may drive one common large-scale outflow; (3) the outflow momentum flux of protostars is proportional to the circumstellar envelope mass (Bontemps et al. 1996). Since binary protostars appear to have preferentially very unequal circumstellar masses (accretion rates), their relative outflow strengths are expected to be also quite unequal. Therefore, the weaker outflow may often be covered by large-scale stronger outflow and not detected. The discovery of an equal-mass protobinary system in L 723 (Chapter 2) and IRAS 16293 (Mundy et al. 1992) and of a weak secondary outflow from the lower-mass component in the unequal-mass protobinary systems CB 230 (see Chapter 2) and BHR 71 (see Chapter 3) strongly support this explanation. However, high-resolution outflow data so far exist only for very few systems and it is too early to derive correlations between alignment, relative outflow strengths, separation, and mass ratios.

6.6 How did protobinary systems accrete?

Accretion onto a protobinary is one of the most important contributions to the final parameters of the system. Numerical simulations of accretion onto a binary system have found that the main dependencies are on the binary mass ratio and the relative specific angular momentum, $j_{\rm inf}$, of the infalling material (see Bate & Bonnell 1997 and Bate 2000). For unequal masses components, low $j_{\rm inf}$ material is accreted by the primary or its disk; for higher $j_{\rm inf}$, the infall can also be accreted by the secondary or its disk; when $j_{\rm inf}$ approaches the specific angular momentum of binary system ($j_{\rm binary} = \sqrt{GM_{\rm B}D} \times \frac{q}{(1+q)^2}$), circumbinary disk formation begins; as $j_{\rm inf} \gg j_{\rm binary}$ the infall is then accreted by neither component but only forms a circumbinary disk (see Fig. 6.7).

In our observations, we find in several protobinary systems that only one component is associated with a great amounts of circumstellar dust while the other is somewhat naked, like e.g., in CB 230 (Chapter 2), BHR 71 (Chapter 3), and SVS 13B (Chapter 4). The large contrast between the two components implies that the accretion and hence development of a circumstellar disk occurs preferentially in only one component, with the disk absent or much less significant in the other one. To compare observations with theoretical simulations, we take SVS 13B as an example. In the SVS 13 B system, we had estimated dynamical mass of $\sim 1.0\,M_{\odot}$, mass ratio $q \sim 1/13$, and separation $D \sim 3800$ AU (see Chapter 4). If we consider specifical angular momentum derived from the N_2H^+ velocity field as $j_{\rm inf}$ ($\sim 1.25 \times 10^{16}\,{\rm m^2\,s^{-1}}$), we then derive $j_{\rm inf}/j_1 \sim 8$, $j_{\rm inf}/j_2$

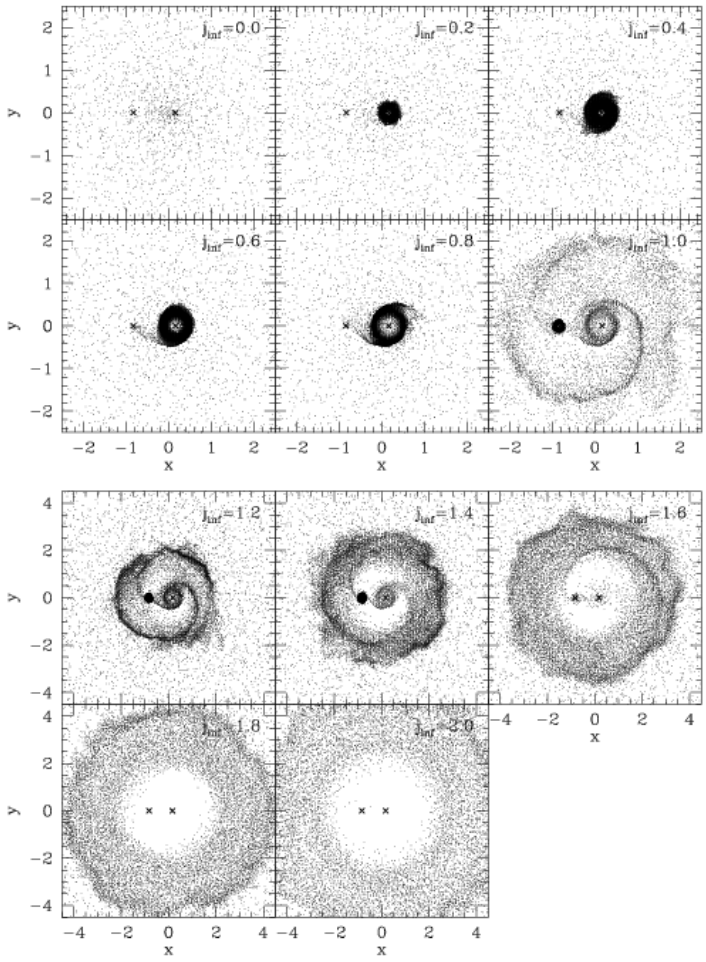

Figure 6.7: Steady-state accretion onto a $q = 0.2$ protobinary system from clouds with various specific angular momentum of the infalling gas $j_{\rm inf}$ in units of the binary specific angular momentum. The protostars are marked with crosses, with the primary on the right. Gas particle positions are projected on to the plane of the binary. Axes are given in units of binary separation D. The image is adopted from Bate & Bonnell (1997).

~ 0.1, and $j_{\rm inf}/j_{\rm B} \sim 0.7$. These ratios correspond to the simulation case that only circumprimary disk could be formed in an accreting protobinary system. Therefore, the observations and simulations are consistent with each other: **only one component associated with a great amounts of circumstellar dust (or disk) is due to the relatively low specific angular momentum in the infalling envelope.**

Chapter 7

Summary and outlook

7.1 Summary

This thesis presents a systematic effort to reveal the physical processes that lead to the formation of binary stars. In order to search for binary protostars and to derive their kinematic properties, we have observed, at high angular resolution, thirteen nearby, isolated, low-mass protostellar cores in the N_2H^+ line and at mm dust continuum, using the OVRO, ATCA, and IRAM-PdBI millimeter arrays. The results were complemented by infrared data from the *Spitzer* and VLT telescopes.

In Chapter 2 I present the results of an interferometric survey for nine nearby, isolated, low-mass protostellar cores, using the OVRO millimeter array. Three binary protostars (IRAS 03282, L723 VLA2, and CB 230) have been identified by OVRO observations, of which IRAS 03282 and L723 VLA2 are new discoveries. Chapter 3 presents interferometric observations of isolated, low-mass protostellar double cores CG 30 and BHR 71, using the ATCA. Chapter 4 presents the observational results from IRAM-PdBI towards two binary protostars L1448 IRS3 and SVS 13. In Chapter 5 I present our preliminary results from a systematic survey for binary systems among young stellar objects in nearby clouds.

From the mm dust continuum images we derive circumstellar mass distribution (ranging from 0.05 to 4.0 $M_\odot$), separations (from 450 to 8700 AU), and mass ratios (from 0.1 to 0.8) for the protostellar binary systems. N_2H^+ line emission is detected from all thirteen objects and is found to be spatially associated and quantitatively correlated with the thermal dust continuum emission. Twelve of the thirteen objects have compact N_2H^+ cores with FWHM radii of $730 - 3500$ AU. The only more evolved (Class I) object in the sample (CB 188) shows only faint and extended N_2H^+ emission, suggesting that the N_2H^+ cores are destroyed or dissipated at the end of the protostellar phase. The mean N_2H^+ line width was found to be 0.45 ± 0.05 km s^{-1}. Estimated virial masses range from 0.3 to 1.7 $M_\odot$. By simultaneously fitting the seven hyperfine line components of N_2H^+, we derive the velocity fields and hence velocity gradient and distribution of specific angular momenta. Most objects in our sample show systematic velocity gradients, which could be explained by either core ration or effect from outflows. The measured velocity gradients across the cores range from 6 to 60 km s^{-1} pc^{-1}, with a mean value of ~ 10 km s^{-1} pc^{-1}. The derived specific angular momenta range

from 0.12 to 0.86 $\times$ 10^{-3} km s^{-1} pc. Furthermore, we derive the energy balance based on N_2H^+ observations and find that thermal and turbulent energy support are about equally important in these cores, while rotational support is negligible. The estimated $\beta_{\rm rot}$ values range from 0.004 to 0.05, with a typical value of $\sim$0.01.

In the survey conducted at VLT/NACO, we find a raw multiplicity rate of $35 \pm 5\%$ with binary separation ranging from 30 AU to 2000 AU for young stellar objects. Based on our preliminary results, as well as the data in the literature, we derive the distribution of specific orbital angular momentum in the pre-main sequence binary systems and find that the specific angular momenta of wide pre-main sequence binaries are close to those derived from the N_2H^+ line observations toward the protostellar cores.

Based on these data, we could, for the first time, derive the distributions of mass ratios and specific angular momenta in protobinary systems, and kinematically study the fragmentation process. We find that binarity/mulitplicity is frequent in the protostellar phase, although it is too early to derive a separation distribution. The circumstellar mass ratio distribution of binary protostars appears to be flat like that of more evolved long-period MS binary stars, and more than 75% of protobinary systems have circumstellar mass ratios below 0.5, i.e., unequal masses are much more common than equal masses. We find that the specific angular momenta of protostellar cores are intermediate between those of prestellar cores and the orbital angular momenta of wide PMS binary systems. There appears to be no significant decrease of angular momentum between the onset of the protostellar collapse and the emergence of a binary star, which suggests that most of the angular momentum contained in the collapse region is transformed into orbital angular momentum of the resulting stellar binary system. Furthermore, we find that during core fragmentation the angular momentum is not evenly, in value and direction, divided between sub-cores. Most cores with binary protostars have ratios of rotational to potential gravitational energy of $\beta_{\rm rot} > 1\%$. This is consistent with theoretical simulations and suggests that the initial amount of rotational energy in a molecular cloud core is playing an important role in the protostellar fragmentation process.

7.2 Future work

Although a series of results have been achieved in this thesis work, we are aware of that kinematic data which would reveal the link between distribution of angular momentum and protostellar fragmentation are still very rare. Obviously, more objects are needed being observed at high angular resolution.

As part of our program, two additional objects (L1448 IRS2 and L1448C) are already in observing (in the N_2H^+ line and at 3 mm dust continuum) at IRAM-PdBI. To enlarge our sample, I plan to continue proposing more objects in the near future at both IRAM-PdBI and ATCA, and then to derive separations, mass ratios, and rotation curves for a larger number of protobinary systems.

Our observations have proved that N_2H^+ is good tracer of cold and quiescent gas and is suitable for studying kinematics of protostellar cores at high angular resolution. However, I want to note that N_2H^+ line emission mainly traces the outer envelope, kinematic and structure information from the inner envelope and disk still remains

untouched in our research. In addition, we find that the N_2H^+ emission is strongly affected by the outflows, both in terms of entrainment and molecule destruction. To probe gas kinematics in the inner protostellar cores where binary stars form, we have to think about new methods and tracers.

The Submillimeter Array (SMA) is an ideal instrument for studies of kinematics and structures in the inner collapsing region. Compared with 3 mm observations, submillimeter dust emission and high-excitation lines constrain the properties of the actual protostellar envelope and are less sensitive to the surrounding cloud material. For example, in the 345 GHz window opened by SMA, $H^{13}CO^+$ transitions are available for exploring the kinematics in the denser ($\sim 10^7 - 10^8\,\mathrm{cm}^{-3}$) and warmer ($\sim 50\,\mathrm{K}$) gas, while in the 230 GHz window, CO isotopic lines can be used to probe different aspects of the physical structure of the envelopes and the associated outflows. Based on these observations, we could disentangle the emission and hence the kinematics and structures from the envelope and circumstellar disk. With this in mind, we have partly extended our program at the SMA. Our earlier CO isotopic lines proposals for the southern binary protostar CG 30 and the binary protostars in the L1448 complex were accepted in the observing period 2007 Nov − 2008 Apr. I plan to continue proposing more objects in high-excitation lines in the forthcoming semesters.

Finally, the Atacama Large Millimeter Array (ALMA), with an angular resolution of down to 10 mas, is the instrument which we expect to bring the breakthrough in our knowledge on the details of the binary star formation process. It may solve many problems concerning the earliest phase of (binary) star formation, but will probably raise more new and unexpected questions.

Appendix A

List of publications

1. **X. P. Chen** & Y. Yao, 2004, *Near-Infrared Observations of the Massive Star Forming Region IRAS 23151+5912*, ChJAA , Vol. 4, No. 3, P 284

2. **X. P. Chen**, Y. Yao, J. Yang, Z. Jiang, and M. Ishii, 2004, *Near-infrared polarimetric and spectrometric study of massive star-forming region S87*, A&A, 428, 523

3. **X. P. Chen** & Y. Yao, 2005, *Near-infrared polarization study of L1641S*, Sciences in China, G. Vol. 48, No. 1, P 68

4. **X. P. Chen**, Th. Henning, R. van Boekel, and C. A. Grady, 2006, *VLT/NACO adaptive optics imaging of the Herbig Ae star HD 100453*, A&A, 445, 331

5. **X. P. Chen**, R. Launhardt, and Th. Henning, 2007, *OVRO N_2H^+ Observations of Class 0 Protostars: Constraints on the Formation of Binary Stars*, ApJ, 669, 1058

6. **X. P. Chen**, R. Launhardt, and Th. Henning, 2007, '*VLT/NACO adaptive optics imaging of GSS 30 IRS1: a protostellar binary system?*, A&A, 475, 277

7. **X. P. Chen**, R. Launhardt, T. Bourke, et al. 2007, *ATCA and Spitzer Observations of the Binary Protostellar Systems CG 30 and BHR 71*, ApJ, submitted

8. **X. P. Chen**, R. Launhardt, and Th. Henning, 2008, *IRAM-PdBI observations of binary protostars I: SVS 13*, ApJ, to be submitted

9. **X. P. Chen**, R. Launhardt, and Th. Henning, et al. 2008, *IRAM-PdBI observations of binary protostars II: L1448 protostellar cluster*, ApJ, in prep.

10. R. Launhardt, **X. P. Chen**, A. I. Sargent, and H. Zinnecker, 2008, *L 723: A binary protostar with a quadrupolar molecular outflow*, ApJL, to be submitted

11. R. Launhardt, **X. P. Chen**, and A. I. Sargent, et al., 2008, *Morphology and kinematics of the protostellar double core in the Bok globule CB 230*, ApJL, to be submitted

12. **X. P. Chen**, R. Launhardt, and Th. Henning, 2008, *VLT/NACO deep imaging of young stellar objects*, A&A, in prep.

13. R. Launhardt, A. I. Sargent, H. Zinnecker, and **X. P. Chen**, 2008, *The internal structure of isolated low-mass protostellar cores: high angular resolution observations of the thermal millimeter dust continuum emission*, ApJ, in prep.

Bibliography

[1] Aikawa, Y., Ohashi, N., Inutsuka, S. I., et al. 2001, ApJ, 552, 639

[2] André, P., Bouwman, J., Belloche, A., & Hennebelle, P. 2002, in Chemistry as a Diagnostic of Star Formaiton, ed. C. L. Curry & M. Fich (NRC Press, Ottawa), 127

[3] André, P., & Montmerle, T. 1994, ApJ, 420, 837

[4] André, P., Ward-Thompson, D., & Barsony, M. 2000, in Protostars and Planets IV, ed. V. Mannings, A. P. Boss, & S. S. Russell (Tucson: Univ. Arizona Press), 59

[5] Anglada, G., Estalella, R., Rodríguez, L. F., Torrelles, J. M., Lopez, R., & Canto, J. 1991, ApJ, 376, 615

[9] Anglada, G., Rodríguez, L. F., & Osorio, M. et al. 2004, ApJ, 605, L137

[7] Anglada, G., Rodríguez, L. F., & Torrelles, J. M. 1996, ApJ, 473, L123

[9] Anglada, G., Rodríguez, L. F., & Torrelles, J. M. 2000, ApJ, 542, L123

[9] Anglada, G., Rodríguez, L. F., & Torrelles, J. M., et al. 1989, ApJ, 341, 208

[10] Arce, H. G., & Sargent, A. I. 2004, ApJ, 624, 232

[11] Aspin, C., Sandell, G., & Russel, A. P. G. 1994, A&AS, 106, 165

[12] Bacciotti, F., Ray, T. P., Eislöffell, J., et al. 2003, Ap&SS, 287, 3

[13] Bachiller, R. 1996, ARA&A, 34, 111

[14] Bachiller, R., & Cernicharo, J. 1986, A&A, 168, 262

[17] Bachiller, R., Guilloteau, S., & Dutrey, A., et al. 1995, A&A, 299, 857

[16] Bachiller, R., Gueth, F., Guilloteau, S. et al. 2000, A&A, 362, L33 (B2000)

[17] Bachiller, R., Guilloteau, S., Dutrey, A. et al. 1995, A&A, 299, 857

[18] Bachiller, R., Guilloteau, S., Gueth, F. et al. 1998, A&A, 339, L49 (B98)

[19] Bachiller, R., Terebey, S., Jarrett, T. et al. 1994, ApJ, 437, 296

[20] Balbus, S. A., 2003, ARA&A, 41, 555

[21] Ballesteros-Paredes, J., Klessen, R. S., Mac Low, M.-M., & Vázquez-Semadeni, E. 2007, in Protostars and Planets V, ed. B. Reipurth, D., Jewitt, & K. Keil (Tucson: Univ. Arizona Press), 63

[22] Bally, J., Devine, D., & Reipurth, B. 1996, ApJ, 473, L49

[23] Baraffe, I., Chabrier, G., Allard, F., & Hauschildt, P. H. 1998, A&A, 337, 403

[24] Barranco, J. A, & Goodman, A. 1998, ApJ, 504, 207

[25] Barsony, M., Kenyon, S. J., Lada, E. A., & Teuben, P. J. 1997, ApJS, 112, 109

[26] Barsony, M., Ward-Thompson, D., André, P., & O'Linger, J. 1998, ApJ, 509, 733

[27] Basu, S., & Mouschovias, T. C. 1994, ApJ, 432, 720

[28] Bate, M. R. 1998, ApJ, 508, L95

[29] Bate, M. R. 2000, MNRAS, 314, 33

[32] Bate, M. R., & Bonnell, I. A. 1997, MNRAS, 285, 33

[31] Bate, M. R., Bonnell, I. A., & Bromm, V. 2003, MNRAS, 339, 577

[32] Bate, M. R., & Burkert, A. 1997, MNRAS, 288, 1060

[33] Belloche, A., & André, P. 2004, A&A, 419, L35

[34] Belloche, A., André, P., Despois, D., & Blinder, S. 2002, A&A, 393, 927

[35] Belloche, A., Hennebelle, P., & André, P. 2006, A&A, 453, 145

[36] Benson, P. J., Caselli, P., & Myers, P. C., 1998, ApJ, 506, 743

[37] Benson, P. J., & Myers, P. C. 1989, ApJS, 71, 89

[38] Bergin, E. A., Ciardi, D. R., Lada, C. J., Alves, J., & Lada, E. A. 2001, ApJ, 557, 209

[39] Bergin, E. A., & Langer, W. D. 1997, ApJ, 486, 316

[40] Boden, A. F., Sargent, A. I., & Akeson, R. L., et al. 2005, ApJ, 635, 442

[41] Bodenheimer, P. 1995, ARA&A, 33, 199

[42] Bodenheimer, P., Burkert, A., Klein, R. I., & Boss, A. P. 2000, in Protostars and Planets IV, ed. V. Mannings, A. P. Boss, & S. R. Russell (Tucson: Univ. Arizona Press), 675

[43] Bonnell, I., & Bate, M. R., 1994, MNRAS, 269, L45

[44] Bonnell, I., Larson, R. B., & Zinnecker, H. 2007, in Protostars and Planets V, ed. B. Reipurth, D. Jewitt, & K. Keil (Tucson: Univ. Arizona Press), 149

[45] Bonnell, I., Martel, H., & Bastien, P. 1991, ApJ, 377, 553

[46] Bontemps, S., André, P., Kaas, A. A., et al. 2001, A&A, 372, 173

[215] Boffin, H. M. J., Watkins, S. J., & Bhattal, A. S. et al. 1998, MNRAS, 300, 1189

[48] Boss, A. P. 1989, ApJ, 346, 336

[49] Boss, A. P. 1999, ApJ, 520, 744

[50] Boss, A. P., & Bodenheimer, P. 1979, ApJ, 234, 289

[51] Boss, A. P., Fisher, R. T., Klein, R. I., & McKee, C. 2000 ApJ, 528, 325

[52] Bourke, T. L. 2001, ApJ, 554, L91 (B01)

[53] Bourke, T. L., Garay, G., Lehtinen, K. K. et al. 1997, ApJ, 476, 781 (B97)

[54] Bouvier, J., & Corporon, P. 2001, in IAU Symp. 200, The Formation of Binary Stars, ed. H. Zinnecker & R. D. Mathieu (San Francisco: ASP), 155

[55] Brandt, J. C., 1971, in: Maran, S. P., Brandt, J. C., Stecher, T. P. (eds.), The Gum Nebula and Related Problemss, NASA SP-322, 4

[56] Briggs, D. S., Schwab, F. R., & Sramek, R. A. 1999, ASPC, 180, 127

[57] Burgasser, A. J., Reid, I. N., Siegler, N. et al. 2007, in Protostars and Planets V, ed. B. Reipurth, D. Jewitt, & K. Keil (Tucson: Univ. Arizona Press), 427

[58] Burkert, A., & Bodenheimer, P. 1993, MNRAS, 264, 798

[59] Cabrit, S., & André, P. 1991, ApJ, 379, 25

[60] Caselli, P., Benson, P. J., Myers, P., & Tafalla, M. 2002, ApJ, 572, 238 (CBMT02)

[61] Caselli, P., Walmsley, C. M., Tafalla, M., Dore, L., & Myers, P. C. 1999, ApJ, 523, L165

[62] Caselli, P., Myers, P. C., Thaddeus, P. 1995, ApJ, 455, L77

[63] Castelaz, M. W., Hackwell, J. A., Grasdalen, G. L. et al. 1985, ApJ, 290, 261

[64] Chandler, C. J., & Richer, J. S. 2000, ApJ, 530, 851

[65] Chen, H., & Tokunaga, A. T. 1994, ApJS, 90, 149

[66] Chini, R., Reipurth, B., & Sievers, A. et al. 1997, A&A, 325, 542

[67] Chrysostomou, A., Clark, S. G., Hough, J. H. et al. 1996, MNRAS, 278, 449

[68] Clemens, D. P., & Barvainis, R. 1988, ApJS, 68, 257

[69] Close, L. M., Dutrey, A., Roddier, F., et al. 1998, ApJ, 499, 883

[70] Coffey, D., Bacciotti, F., Woitas, J., et al. 2004, ApJ, 604, 758

[71] Corporon, P., & Reipurth, B. 1997, in IAU Symp. 182, Poster Proc., Low-Mass Star Formation−−From Infall to Outflow, ed. F. Malbert & A. Castets (Grenobel: Obs. Grenoble), 85

[72] Covey, K. R., Greene, T. P., Doppmann, G. W., & Lada, C. J. 2005, AJ, 129, 2765

[73] Curiel, S., Raymond, J. C., Moran, J. M., et al. 1990, ApJ, 365, 85

[74] Curiel, S., Torrelles, J. M., Rodríguez, L. F., et al. 1999, ApJ, 527, 310

[75] Curiel, S., Girart, J. M., Rodríguez, L. F., & Cantó, J. 2004, RMxAC, 21, 137

[76] Cutri, R. M. et al. 2003, The 2MASS All-Sky Catalog of Point Sources

[77] D'antona, F., & Mazzitelli, I. 1994, ApJS, 90, 467

[78] Davidson, J. A. 1987, ApJ, 315, 602

[79] De Vries, Ch. H., Narayanan, G., & Snell, R. L. 2002, ApJ, 577, 798

[80] Di Francesco, J., Evans II, N. J., Myers, P. C. et al. 2007, in Protostars and Planets V, ed. B. Reipurth, D. Jewitt, & K. Keil (Tucson: Univ. Arizona Press), 17

[81] Di Francesco, J., Myers, P. C., & Wilner, D. J. et al. 2001, ApJ, 562, 770

[82] Dominik, C., Dullemond, C. P., Waters, L. B. F. M., & Walch, S. 2003, A&A, 398, 607

[83] Duchêne, G., Beust, H., & Adjali, F., et al. 2006, A&A, 457, L9

[85] Duchêne, G., Bontemps, S., & Bouvier, J., et al. 2007, A&A, 476, 229

[85] Duchêne, G., Bouvier, J., Bontemps, S. et al. 2004, A&A, 427, 651

[86] Duchêne, G., Delgado-Donate, E., Haisch, K. E., Loinard, L., & Rodríguez, L. 2007, in Protostars and Planets V, ed. B. Reipurth, D. Jewitt, & K. Keil (Tucson: Univ. Arizona Press), 379

[87] Duquennoy, A., & Mayor, M. 1991, A&A, 248, 485 (DM91)

[88] Elias, J. H. 1978, ApJ, 224, 453

[90] Evans II, N. J., Allen, L. E., & Blake, G. A., et al. 2003, PASP, 115, 965

[90] Evans II, N. J., Rawlings, J. M. C., Shirley, Y. et al. 2001, ApJ, 557, 193

[91] Feigelson, E. D., & Nelson, P. I., 1985, ApJ, 293, 192

[92] Fischer, D. A., & Marcy, G. W. 1992, ApJ, 396, 178

[93] Forveille, T. Guilloteau, S., & Lucas, R. 1989, CLASS Manual (Grenoble: IRAM)

[94] Froebrich, D. 2005, ApJS, 156, 169

[95] Fuller, G. A., & Myers, P. C. 1992, ApJ, 384, 523

[96] Gehz, A. M., McCarthy, D. W., Patience, J. L., & Beck, T. L. 1997, ApJ, 481, 378

[97] Girart, J. M., Estalella, R., Anglada, G., et al. 1997, ApJ, 489, 734

[98] Goldsmith, P. F., Snell, R. L., Hemeon-Heyer, M., & Langer, W. D. 1984, ApJ, 286, 599

[99] Goodman, A. A., Barranco, J. A., Wilner, D. J., & Heyer, M. H. 1998, ApJ, 504, 223

[100] Goodman, A. A., Benson, P. J., Fuller, G. A., & Myers, P. C. 1993, ApJ, 406, 528 (GBFM93)

[101] Goodwin, S. P., Kroupa, P., Goodman, A., & Burkert, A. 2007, in Protostars and Planets V, ed. B. Reipurth, D. Jewitt, & K. Keil (Tucson: Univ. Arizona Press), 133

[102] Goodwin, S. P., Whitworth, A. P., & Ward-Thompson, D. 2004, A&A, 423, 169

[103] Grasdalen, G. L., Strom, K. M., & Strom, S. E. 1973, ApJ, 184, L53

[104] Greene, T. P., Wilking, B. A., André, P., et al. 1994, ApJ, 434, 614

[105] Gueth, F., Bachiller, R., & Tafalla, M. 2003, A&A, 401, L5

[106] Guilloteau, S., Bachiller, R., Fuente, A., & Lucas, R. 1992, A&A, 265, L49

[107] Haisch, K. E., Barsony, M., Greene, T. P. & Ressler, M. E. 2002, AJ, 124, 2841

[108] Halbwachs, J. L., Mayor, M., Udry, S., & Arenou, F. 2003, A&A, 397, 159

[109] Henning, Th., & Launhardt, R. 1998, A&A, 338, 223

[110] Henning, Th., Wolf, S., Launhardt, R., & Waters, R. 2001, ApJ, 561, 871

[111] Herbig, G. H. 1974, Lick Obs. Bull., 658

[112] Herbig, G. H. & Jones, B. F. 1983, AJ, 88, 1040

[113] Hirota, T., Bushimata, T., Choi, Y. K., et al., 2008, PASJ, 60, in press

[114] Hodapp, K.-W., & Ladd, E. F. 1995, ApJ, 453, 715

[115] Jappsen, A.-K., & Klessen, R. S. 2004, A&A, 423, 1

[116] Jennings, R. E., Cameron, D. H. M., Cudlip, W., & Hirst, C. J. 1987, MNRAS, 226, 461

[117] Johnstone, D., Wilson, C. D., & Moriarty-Schieven, G., et al. 2000, ApJ, 545, 327

[118] Jørgensen, J. K. 2004, A&A, 424, 589

[119] Kaas, A. A., Olofsson, G., Bontemps, S., et al. 2004, A&A, 421, 623

[120] Khanzadyan, T., Smith, M. D., Davis, C. J. 2003, MNRAS, 338, 57

[121] Kenyon, S. J., & Hartmann, L. 1995, ApJS, 101, 117

[122] Klessen, R. S., Ballesteros-Paredes, J., Vázquez-Semadeni, E., & Durán-Rojas, E. 2005, ApJ, 620, 786

[123] Klessen, R. S., Heitsch, F., & Mac Low M. M. 2000, ApJ, 535, 887

[124] Knude, J., Jønch-Sørensen, H., & Nielsen, A. S. 1999, A&A, 350, 985

[125] Köhler, R., & Leinert, C. 1998, A&A, 331, 977

[126] Kouwenhoven, M. B. N., Brown, A. G. A., & Zinnecker, H. 2005, A&A, 430, 137

[127] Lada, C. J. 1987, in Star forming regions, IAU Symp. 115, 1

[128] Larson, R. B. 1995, MNRAS, 272, 213

[129] Larson, R. B. 2002, MNRAS, 332, 155

[130] Larson, R. B. 2003, Reports on Progress in Physics, 66, 1651

[131] Lamm, M. H. 2003, PhD thesis, Heidelberg University

[137] Launhardt R. 2001, in The Formation of Binary Stars, IAU Symp. 200, ed. H. Zinnecker, & R. D. Mathieu (San Francisco: ASP), 117

[133] Launhardt, R. 2004, in IAU Symp. 221, Star Formation at High Angular Resolution, ed. M. G. Burton, R. Jayawardhana, & T. L. Bourke (San Francisco: ASP), 213

[134] Launhardt, R., Evans, N. J., Wang, Y., Clemens, D. P., Henning, T., & Yun, J. L. 1998, ApJS, 119, 59

[135] Launhardt, R., & Henning, Th. 1997, A&A, 326, 329

[137] Launhardt, R., & Sargent, A. I. 2001, ApJL, 562, 173

[137] Launhardt, R., Sargent, A. I., Henning, Th. et al. 2001, Poster Proc. of IAU Symp. 200, 103

[138] LaValley, M., Isobe, T., & Feigelson, E. D., 1992, "ASURV", Bull. Am. Astron. Soc.

[140] Lee, C.-F., Mundy, L. G., Stone, J. M., Ostriker, E. C. 2002, ApJ, 576, 294

[140] Lee, C. W., Myers, P. C., & Tafalla, M. 2001, ApJS, 136, 703

[141] Leinert, C., Zinnecker, H., & Weitzel, N. et al. 1993, A&A, 278, 129

[142] Lenzen, R., Hartung, M., Brandner, W., et al. 2003, SPIE, 4841, 944

[143] Looney, L. W., Mundy, L. G., & Welch, W. J. 2000, ApJ, 529, 477 (LMW2000)

[144] Lopez, R., Estalella, R., Gomez, G., & Riera, A. 2006, A&A, 454, 233

[145] Lubow, S. H., & Artymowicz, P. 2000, in Protostars and Planets IV, ed., V. Mannings, A. P. Boss, & S. R. Russell (Tuscon: Univ. Arizona press), 731

[146] Machida, M. N., Matsumoto, T., Hanawa, T., & Tomisaka, K. 2005, MNRAS, 362, 382

[147] Mac Low, M.-M., & Klessen, R. S., 2004, Reviews of Modern Physcis, 76, 125

[148] Malfait, K., Bogaert, E., & Waelkens, C. 1998, A&A, 331, 211

[149] Mamajek, E. E., Meyer, M. R., & Liebert, J. 2002, AJ, 124, 1670

[150] Mardones, D., Myers, P. C., Tafalla, M., Wilner, D. J., Bachiller, R., & Garay, G. 1997, ApJ, 489, 719

[151] Mathieu, R.D. 1994, ARA&A, 32, 465

[152] Mathieu, R. D., Ghez, A. M., Jensen, E. L. N., & Simon, M. 2000, in Protostars and Planets IV, ed. V. Mannings, A. P. Boss, & S. R. Russell (Tucson: Univ. Arizona Press), 703

[153] Mayor, M., Duquennoy, A., Halbwachs, J.-L., & Mermilliod J.-C. 1992, In Complementary Approaches to Double and Multiple Star Research (H. A. McAlister & W. I. Hartkopf, eds.), pp. 73-81. ASP Conf. Series, San Francisco

[154] Mazeh, T., Goldberg, D., Duquennoy, A., & Mayor, M. 1992, ApJ, 401, 265

[155] McKee, C. F., & Ostriker, E. C. 2007, ARA&A, 45, 565

[156] Meeus, G., Waters, L. B. F. M., Bouwman, J., et al. 2001, A&A, 365, 476

[157] Meeus, G., Bouwman, J., Dominik, C., Waters, L. B. F. M., & de Koter, A. 2002, A&A, 392, 1039

[158] Mizuno, A., Fukui, Y., Iwata, T., Nozawa, S., & Takano, T. 1990, ApJ, 356, 184

[159] Motte, F., & André, P. 2001, A&A, 365, 440

[160] Mouschovias, T. Ch. 1991, The Physics of Star Formation and Early Stellar Evolution, ed. C. J. Lada & N. D. Kylafis (Dordrecht: Kluwer), 61

[161] Mouschovias, T. Ch., & Ciolek, G. E. 1999, The Origin of Stars and Planetary Systems, ed. C. J. Lada and N. D. Kylafis (Dordrecht: Kluwer), 305

[162] Mundy, L. E., Looney, L. W., Welch, W. J. 2001, in The Formation of Binary Stars, IAU Symp. 200, ed. H. Zinnecker, & R. D. Mathieu (San Francisco: ASP), 136

[163] Mundy, L. G., Wootten, A., Wilking, B. A., Blake, G. A., & Sargent, A. I. 1992, ApJ, 385, 306

[164] Ossenkopf, V., & Henning, Th. 1994, A&A, 291, 943

[165] Padin, S., Scott, S. L., Woody, D. P., et al. 1991, PASP, 103, 461

[166] Palacios, J. & Eiroa, C. 1999, A&A, 346, 233

[167] Park, Y., Lee, C. W., & Myers, P. 2004, ApJS, 152, 81

[168] Praise, B., Belloche, A., & Leurini, S. et al. 2006, A&A, 454, L79

[169] Patience, J., Ghez, A. M., Reid, I. N., & Matthews, K. 2002, AJ, 123, 1570

[170] Perryman, M. A. C., Lindegren, L., & Kovalevsky, J. et al. 1997, A&A, 323, 49

[171] Persi, P., Ferrari-Toniolo, M., & Busso, M. et al. 1990, AJ, 99, 303

[172] Persi, P., Palagi, F., & Felli, M. 1994, A&A, 291, 577

[173] Persson, S. E., Murphy, D. C., Krzeminski, W., Roth, M., & Rieke, M. J. 1998, AJ, 116, 2475

[174] Pontoppidan, K. M., Schöier, F. L., van Dishoeck, E. F., & Dartois, E. 2002, A&A, 393, 585

[175] Prato, L., Simon, M., Mazeh, T., et al. 2002, ApJ, 579, 99

[176] Ray, T., Dougados, C., & Bacciotti, F., et al. 2007, in Protostars and Planets V, ed. B. Reipurth, D. Jewitt, & K. Keil (Tucson: Univ. Arizona Press), 231

[177] Reipurth, B. 1983, A&A, 117, 183

[178] Reipurth, B., & Bally, J. 2001, ARA&A, 39, 403

[179] Reipurth, B., Bally, J., & Devine, D. 1997, AJ, 114, 2708

[180] Reipurth, B., Chini, R., Krugel, E., Kreysa, E., & Sievers, A. 1993, A&A, 273, 221

[181] Reipurth, B., Jewitt, D., & Keil, K. (ed.) 2007, Protostars and Planets V (Tucson: Univ. Arizona Press)

[182] Rodríguez, L. F. 2004, RMxAC, 21, 93

[183] Rodríguez, L. F., Anglada, G., & Curiel, S. 1997, ApJ, 480, L125

[184] Rodríguez, L. F., Anglada, G., & Curiel, S. 1999, ApJS, 125, 427

[185] Rodríguez, L. F., Anglada, G., Torrelles, J. M., et al. 2002, A&A, 389, 572

[186] Rousset, G., Lacombe, F., Puget, P. et al. 2003, SPIE, 4839, 140

[187] Saigo, K., & Tomisaka, K. 2006, ApJ, 645, 381

[188] Sault, R. J., Teuben, P. J., & Wright, M. C. H. 1995, in ASP Conf. Ser. 77, Astronomical Data Analysis Software and Systems IV, ed. R. A. Shaw, H. E. Payne, & J. J. E. Hayes (San Francisco: ASP), 443

[189] Scoville, N. Z., Carlstrom, J. E., Chandler, C. J. et al. 1993, PASP, 105, 1482

[190] Shang, H., Li, Z.-Y., & Hirano, N. 2007, in Protostars and Planets V, ed. B. Reipurth, D. Jewitt, & K. Keil (Tucson: Univ. Arizona Press), 261

[191] Shirley, Y. L., Evans II, N. J., & Rawlings, J. M. C. 2002, ApJ, 575, 337

[192] Shirley, Y. L., Evans II, N. J., Rawlings, J. M. C., & Gregersen, E. M. 2000, ApJS, 131, 249

[193] Shu, F. H. 1977, ApJ, 214, 488

[194] Shu, F. H., Adams, F. C., & Lizano, S. 1987, ARA&A, 25, 23

[195] Spitzer, L. Jr. 1978, Physical Process in the Interstellar Medium, New York, Wiley

[196] Stahler, S. W., & Palla, F. 2004, The formation of stars (Wiley press)

[197] Strom, S. E., Grasdalen, G. L., & Strom, K. M. 1974, ApJ, 191, 111

[199] Strom, S. E., Vrba, F. J., & Strom, K. M. 1976, AJ, 81, 314

[199] Strom, K. M., Newton, G., Strom, S. E., et al. 1989, ApJS, 71, 183

[201] Tafalla, M., Mardones, D., Myers, P. C., et al. 1998, ApJ, 504, 900

[201] Tafalla, M., Santiago, J., Johnstone, D., & Bachiller, R. 2004, A&A, 423, L21

[202] Tamura, M., Sato, S., Suzuki, H. et al. 1990, ApJ, 350, 728

[203] Tamura, M. et al. 1991, ApJ, 378, 611

[204] Terebey, S., & Padgett, D. L. 1997, in IAU Symp. 182, Herbig-Haro Flows and the Birth of Low Mass Stars, ed., B. Reipurth & C. Bertout (Dordrecht: Kluwer), 507

[205] Thies, I., Kroupa, P., Thies, C. 2005, MNRAS, 364, 961

[206] Tohline, J. E. 2002, ARA&A, 40, 349

[207] Turner, B. E., & Thaddeus, P. 1977, ApJ, 211, 755

[208] Vallée, J. P., Bastien, P., & Greaves, J. S. 2000, ApJ, 542, 352

[209] Vandenbussche, B., Dominik, C., Min, M. et al. 2004, A&A, 427, 519

[210] Volgenau, N. H., Mundy, L. G., Looney, L. W., & Welch, W. J. 2006, ApJ, 651, 301

[211] Walker, C. K., Lada, C. J., Young, E. T., & Margulis, M. 1988, ApJ, 332, 335.

[212] Wang, Y., Evans II, N. J., Zhou, S., & Clemens, D. P. 1995, ApJ, 454, 217

[213] Ward-Thompson, D., André, P., Crutcher, R. et al. 2007, in Protostars and Planets V, ed. B. Reipurth, D. Jewitt, & K. Keil (Tucson: Univ. Arizona Press), 33

[214] Ward-Thompson, D., Motte, F., & André, P. 1999, MNRAS, 268, 276

[215] Watkins, S. J., Bhattal, A. S, & Boffin, H. M. J., et al. 1998, MNRAS, 300, 1205

[216] Weintraub, D. A., Kastner, J. H., Griffith, L. L., & Campins, H. 1993, AJ, 105, 271

[217] Wilking, B. A., Lada, C. J., & Young, E. T. 1989, ApJ, 340, 823

[218] Williams, J. P., de Geus, E. J., & Blitz, L. 1994, ApJ, 428, 693

[219] White, R. J., & Ghez, A. M. 2001, ApJ, 556, 265

[220] hitworth, A. P., Bhattal, A. S., Francis, N., & Watkins, S J. 1996, MNRAS, 283, 1061

[222] Wolf, S., Launhardt, R., & Henning, Th. 2003a, ApJ, 592, 233

[222] Wolf, S., Padgett, D. L., & Stapelfeldt, K. R., 2003b, ApJ, 588, 373

[223] Wolf-Chase, G. A., Barsony, M., & O'Linger, J. 2000, AJ, 120, 1467

[224] Womack, M., Ziurys, L. M., & Wyckoff, S. 1992, ApJ, 387, 417

[225] Wu, Y., Huang, M., & He, J. 1996, A&AS, 115, 283

[226] Yun, J. L. & Clemens, D. P. 1994, ApJS, 92, 145

[227] Zhang, Q., Wootten, A., & Ho, P. T. P. 1997, ApJ, 475, 713

[228] Zinnecker, H., & Correia, S. 2004, ASPC, 318, 34

[229] Zinnecker, H., Bastien, P., Arcoragi, J. P., & Yorke, H. W. 1992, A&A, 265, 726

[230] Zinnecker, H., & Mathieu, R. D. (ed.) 2001, IAU Symposium. 200, The Formation of Binary stars (San Francisco: ASP)

Acknowledgements

This thesis was written at the Max Planck Institute for Astronomy between January 2005 and December 2007. I would like to thank all the people who helped me to successfully complete this thesis. Their time, effort, and support are greatly appreciated.

In particular, I want to thank Dr. Ralf Launhardt for the great support, many discussions about science and life, and lots of comments and corrections throughout the whole thesis work. I could not finish this thesis without his help. Thank you, Ralf! I am indebted you forever.

I want to thank Prof. Dr. Thomas Henning for giving me the opportunity to conducting PhD research at MPIA and supporting me in many ways during the past three years.

Thank Prof. Dr. Ralf Klessen for being my co-referee.

I like to thank the Star Formation group and System Administrators at MPIA for the nice working atmosphere.

The MPIA graduate students have provided me with friendship, support and scientific discussion. Thanks!

It is also my pleasure to thank my roommates, Anke, Paola, Boris, and David, for providing me with the perfect environment to balance work and fun.

I am grateful for the hospitality of Prof. Dr. Alyssa Goodman, Dr. Qizhou Zhang, and Dr. Tyler Bourke during my visiting at the Harvard-Smithsonian Center for Astrophysics.

I acknowledge financial support from the Max-Planck-Gesellschaft.

I would like to thank my parents and brother for their support and love I got over the years.

Finally, I want to thank my wife, Yingna Su, for the wonderful life that we share. I would not complete my PhD study without her unending love and encouragement. This thesis is for her.

Erklärung

Ich versichere, daß ich diese Arbeit selbständig verfaßt und keine anderen als die angegebenen Quellen und Hilfsmittel benutzt habe.

Declaration

I confirm, that I produced this work by my own hand and that I did not use any other resources and help except for those mentioned.

Heidelberg, January 2008 .....

Unterschrift / Signature